UNIVERSITY OF CALIFORNIA

SANTA CRUZ

Inclusive Photoproduction of π^0 and η Mesons in the 50 to 130 GeV Energy Range

A Thesis submitted in partial satisfaction
of the requirements for the degree of

DOCTOR OF PHILOSOPHY

in

PHYSICS

by

Alan Martin Breakstone

June 1980

The Thesis of Alan Martin Breakstone
is approved:

Dean of the Graduate Division

Reproduced with permission of the copyright owner. Further reproduction prohibited without permission.

Abstract

Inclusive Photoproduction of π^0 and η Mesons in the 50 to 130 GeV Energy Range

We conducted an experiment at the Tagged Photon Laboratory at the Fermi National Accelerator Laboratory to measure elastic photon-proton scattering, quasi-elastic vector and pseudoscalar meson photoproduction, and inclusive single photon and pseudoscalar meson photoproduction. This thesis describes the detection system of the experiment and data-taking and analysis procedures used for the extraction of Feynman x (x_F) and transverse momentum (p_t) distributions for inclusive photoproduction of π^0 and η mesons.

Using tagged photons ranging from 50 to 130 GeV incident on a 75 cm long liquid hydrogen target, we measure inclusive π^0 production for $.35 < x_F < 1.0$ with $.3 < p_t < 1.4$ GeV/c and inclusive η production for $.35 < x_F < 1.0$ with $0 < p_t < 1.4$ GeV/c. Clear π^0 and η signals are observed. The distributions in both x_F and p_t are consistent with scaling. The average transverse momentum of π^0's is $.57 \pm .07$ GeV/c, while for η's it is $.52 \pm .04$ GeV/c. The average η/π^0 ratio is $.52 \pm .10$ over the range $.3 < p_t < 1.4$ GeV/c and $.35 < x_F < 1.0$.

Reproduced with permission of the copyright owner. Further reproduction prohibited without permission.

Acknowledgments

As is usually the case for an experiment of this magnitude, there are a large number of people to thank for the time and effort they devoted to the project. Let me begin by acknowledging the support of Fermilab personnel, in particular Ed Mottys, who provided excellent technical help in assembling the detectors, and our liason physicist, Peter Garbincius, particulary for his expertise on the beam line and tagging system.

For the construction of the detection apparatus I wish to thank our engineer, Walter Nilsson, and technicians Leonard Bazzani and Bill Rowe, as well as many others, including some very fine undergraduates such as Bill Carlson, Cathy Chewey, and Chris Tacklind. We also exploited the programming skills of the undergraduate students Mike Recce and Dan Nguyen, whose efforts have greatly aided the analysis of the data.

During the most crucial stages of the experiment, mainly just prior to and during the data taking, we required much hard work from a number of people, including several of those listed above. In particular I want to thank two other graduate students, Franco Grancagnolo and Mike Badzik, who spent summers at Fermilab helping us set up and run the experiment. Also in this category are some senior-level

Reproduced with permission of the copyright owner. Further reproduction prohibited without permission.

people including Professor David Dorfan and Terry Schalk, who wrote much of the on-line software. Special thanks go to David Cheng, who helped design the detection apparatus, to Hartmut Sadrozinski, for his work on the final stages of the analysis of the data, and to Dennis Smith for his continued presence at Fermilab and at Santa Cruz during all phases of the experiment.

But my highest accolades are reserved for those of whom it can truly be said that the experiment would have failed without them. My fellow graduate students Alex Grillo and Vittorio Palladino worked so very hard and for so very long, displaying both superlative abilities and great dedication, often with great personal sacrifice, that it is impossible to thank them enough for their efforts. I learned a great deal from each of them; however, the true guiding light of the experiment and the person from whom I learned the most and who helped me the most is Abe Seiden. His creative brilliance and ceaseless efforts clearly made the difference between success and failure of the experiment. His own selflessness and modesty coupled with his deep compassion for others and the sacrifices they made should serve as a model to us all. Abe is one of the finest physicists and nicest human beings I have ever met, a truly remarkable person.

Finally, I also wish to thank my thesis advisor, Clemens Heusch, for steady financial support, and his aid in

Reproduced with permission of the copyright owner. Further reproduction prohibited without permission.

preparation of this thesis.

June 13, 1980

Reproduced with permission of the copyright owner. Further reproduction prohibited without permission.

Table of Contents

Chapter 1: Introductory Remarks
- 1.1. General Features of the Data
- 1.2. Hard Scattering Models
- 1.3. Soft Scattering Models

Chapter 2: Description of Experimental Apparatus
- 2.1. Beam Line
- 2.2. Tagging System
- 2.3. Hydrogen Target
- 2.4. Detection Apparatus

Chapter 3: Data Collection Procedure
- 3.1. Trigger Logic
- 3.2. CAMAC and Computer
  - 3.2.1. CAMAC System
  - 3.2.2. Computer Configuration and Data Flow
- 3.3. Setup of the Experiment
- 3.4. Calibration Runs
- 3.5. Data Runs
- 3.6. Summary of the Data Collected

Chapter 4: Analysis Procedure
- 4.1. Tape Copying
- 4.2. Monitor Programs
  - 4.2.1. ADC Pedestals
  - 4.2.2. Lead Glass Gains
  - 4.2.3. Gains of the Hodoscope and Total Absorption Counters
  - 4.2.4. The Grand Monitor Program
- 4.3. Forward Detector Analysis Routines
- 4.4. Corrections to Shower Energy, Position, and Width
- 4.5. Inclusive Filters
- 4.6. Mass Fits, Efficiency, and Normalization

Chapter 5: Results
- 5.1. Results
- 5.2. Discussion
- 5.3. Conclusions

Reproduced with permission of the copyright owner. Further reproduction prohibited without permission.

Appendix A: Design and Description of Forward Detector Components
A.1. General Design Considerations
A.2. Design, Testing, and Assembly of the Total Absorption Counters
A.3. Design, Testing, and Assembly of the Hodoscope
A.4. Overall Assembly

Appendix B: Forward Detector Calibration Procedures and Results
B.1. General Remarks
B.2. Calibration Procedures
B.3. Analysis and Results
B.3.1. Attenuation Functions and Gains
B.3.2. Lateral Shower Spread
B.3.3. Longitudinal Shower Development
B.3.4. Energy Dependence and Resolution
B.3.5. Shower Width and Position Resolution

Appendix C: On-line Monitoring Systems
C.1. General Requirements
C.2. LED System for the Total Absorption Counters
C.3. Americium Sources for the Total Absorption Counters
C.4. Muon Monitor
C.5. LED and Americium Source System for the Hodoscope
C.6. Time-of-Flight LED System

Appendix D: Derivation of Formulas
D.1. Overlapping Hodoscope Clusters
D.2. Di-photon Mass

References

Reproduced with permission of the copyright owner. Further reproduction prohibited without permission.

Tables

3-1 Summary of run conditions

4-1 U and V gain correction factors

5-1 Summary of cuts on π^0 and η data samples

5-2 p_t distributions for inclusive η production

5-3 x_F distributions for inclusive η production

5-4 p_t distributions for inclusive π^0 production

5-5 x_F distributions for inclusive π^0 production

5-6 η/π^0 ratio
a) vs. transverse momentum
b) vs. Feynman x

5-7 Average p_t for π^0 and η mesons as a function of x_F

5-8 Comparison of average transverse momenta from different experiments

A-1 Expected energy deposition in the total absorption counters

B-1 Lateral spread of showers in the total absorption counters
a) Pulse heights
b) Percentage of shower seen by U + V

B-2 Fraction of shower in the U and V counters as a function of energy
a) Electron-initiated showers
b) Photon-initiated showers

B-3 Shower width and position resolution in the hodoscope

Reproduced with permission of the copyright owner. Further reproduction prohibited without permission.

Figures

1-1 Lowest order Feynman graphs for inelastic electron-proton and photon-proton scattering

1-2 Quark cascade model

2-1 Electron yields for 400 GeV/c incident protons

2-2 E152 beamline (schematic)

2-3 Tagging system

2-4 Hydrogen target

2-5 Experimental layout

2-6 Recoil detector
a) Front view
b) Side view

2-7 Drift chamber drift cell

2-8 Time-of-flight counter

2-9 Recoil detector assembly

2-10 Forward detector assembly, side view

2-11 Forward detector assembly, front view

2-12 Forward charged particle counters

3-1 Simplified experimental trigger logic

3-2 Nova configuration

4-1 Average value of the monitors for a typical total absorption counter versus tape number
a) Americium
b) LED
c) Muon
d) Americium/muon ratio
e) Americium/LED ratio

Reproduced with permission of the copyright owner. Further reproduction prohibited without permission.

4-2 Average value of the monitors for a typical hodoscope counter versus tape number
a) Americium
b) LED
c) Americium/LED ratio

4-3 Gain for a typical total absorption counter versus tape number

4-4 Mass squared for individual showers

4-5 Reconstructed vs. calculated energy of showers from omega decays

4-6 Typical mass histogram with fit for eta inclusive measurement

5-1 Inclusive η transverse momentum distribution as a function of E_γ

5-2 Inclusive η transverse momentum distribution as a function of x_F
a) $.35 < x_F < .45$
b) $.45 < x_F < .6$
c) $.6 < x_F < .9$

5-3 Inclusive η Feynman x distribution as a function of E_γ

5-4 Inclusive π^0 transverse momentum distribution as a function of E_γ

5-5 Inclusive π^0 transverse momentum distribution as a function of x_F
a) $.35 < x_F < .45$
b) $.45 < x_F < .6$
c) $.6 < x_F < .9$

5-6 Inclusive π^0 Feynman x distribution as a function of E_γ

5-7 η/π^0 ratio as a function of transverse momentum

5-8 η/π^0 ratio as a function of Feynman x

5-9 Comparison of Feynman x distributions from different experiments

Reproduced with permission of the copyright owner. Further reproduction prohibited without permission.

A-1 Cross sectional view of the total absorption and hodoscope counters showing the configuration of lead and other materials

A-2 Shower distribution function

A-3 Scale drawings of the total absorption counters

A-4 RCA 4525 base circuit diagram

A-5 RCA 4517 base circuit diagram

B-1 Total absorption counter attenuation function

B-2 Hodoscope attenuation function

B-3 Percentage of shower seen in a U/V module as a function of distance from the counter edge

B-4 U/V ratio versus energy for electron and photon initiated showers

B-5 U/V pulse height distributions for 135 GeV electrons
- a) U
- b) V
- c) (U + V)/2

B-6 Pulse height and energy resolution versus energy for the total absorption counters

B-7 Pulse height and energy resolution versus energy for the hodoscope

B-8 Hodoscope distributions for 30 and 135 GeV electron showers
- a) Pulse height versus counter number for one event
- b) Pulse height sum over nine strips
- c) Average position
- d) Shower width

C-1 Total absorption counter LED hardware

C-2 Block diagram of LED electrical system
- a) Switching system
- b) Trigger logic

C-3 Trigger logic for the total absorption counter americium monitor

Reproduced with permission of the copyright owner. Further reproduction prohibited without permission.

C-4 Location of muon counters in the hodoscope

C-5 Muon monitor trigger logic

C-6 Total absorption counter monitors and gain versus time

C-7 Americium and LED system for hodoscope
  a) One hodoscope section (24 counters) showing fiber optics
  b) End view of a typical counter

C-8 Trigger logic for the hodoscope americium monitor

C-9 Hodoscope monitors versus time

C-10 Time-of-flight LED hardware

Reproduced with permission of the copyright owner. Further reproduction prohibited without permission.

Chapter 1

Introductory Remarks

For many years scientists have used photon scattering to probe the structure of matter. In essence our eyes are a sophisticated detector of the scattering of light off of ordinary objects. The scale with which photons probe matter is proportional to their wavelength; thus, it is inversely proportional to their energy. We have conducted an experiment with the highest energy photon beam in the world to probe the structure of the proton at the smallest possible distances. We built a single detection apparatus to measure a number of different reactions: elastic scattering ($\gamma p \rightarrow \gamma p$), quasi-elastic pseudoscalar and vector meson production ($\gamma p \rightarrow \pi^0 p$, $\gamma p \rightarrow \eta p$, and $\gamma p \rightarrow \omega p$), and inclusive production of pseudoscalar mesons and single photons ($\gamma p \rightarrow \pi^0 X$, $\gamma p \rightarrow \eta X$, and $\gamma p \rightarrow \gamma X$, where X means any other particle or set of particles). This experiment provides a first look at these reactions at energies more than an order of magnitude higher than they have been previously studied. It provides valuable new information on both the hadronic nature of the photon and the internal structure of the proton. In this thesis I will describe the entire detection apparatus and data taking procedures, concentrating on those aspects which are particularly important for inclusive pseudoscalar meson production. I will go on to

Reproduced with permission of the copyright owner. Further reproduction prohibited without permission.

describe in some detail the analysis of the inclusive channels $\gamma p \rightarrow \pi^0 X$ and $\gamma p \rightarrow \eta X$, giving the results and comparing them to those of other similar experiments.

1.1. General Features of the Data

Multiparticle production is characterized by four major properties:

1) the leading particle effect
2) limited transverse momentum
3) logarithmic rise in multiplicities
4) scaling in inclusive distributions

The leading particle effect (often referred to as peripheralism) implies that the quantum numbers of the beam and target particles tend to be preserved in an interaction. For example, in photon-proton scattering, the particles produced in the forward direction (the direction of the photon) are typically vector mesons which have the same quantum numbers as the photon. Because of this effect, we use the terms beam and target fragmentation regions to refer to the kinematical regions in the forward and backward directions in the center-of-mass system.

Reactions are also characterized by the production of relatively few particles with small transverse momentum. Most of the energy of a reaction goes into kinetic energy of the products rather than particle production per se. The number of particles produced rises approximately

Reproduced with permission of the copyright owner. Further reproduction prohibited without permission.

logarithmically with increasing center-of-mass energy. For transverse momenta less than about 1 GeV/c, the transverse momentum dependence of the inclusive cross sections is roughly exponential, yielding an average value of about 350 MeV/c, whereas for higher transverse momenta it assumes a power law behavior with an exponent ranging from about 8 to 12, depending on the beam and target particles and the inclusive particle species. This suggests different mechanisms for the production of high- versus low-transverse-momentum particles. Physicists make a distinction between "soft" scattering models, such as the Vector Dominance Model (VDM), which are responsible for the production of low-transverse-momentum particles, and "hard" scattering models, such as the Constituent Interchange Model (CIM) and parton models, which describe the production of particles with high transverse momenta.

For high-multiplicity reactions, one finds a large number of fairly low energy particles in the center-of-mass system. This is referred to as the central region. The types of particles produced in this region are not strongly correlated with the beam and target particles as is the case in their respective fragmentation regions. This suggests a production mechanism which is similar for all hadrons.

Finally, one finds a sort of beam energy independence of the inclusive cross sections called scaling. One might expect that an inclusive cross section depends on the total

Reproduced with permission of the copyright owner. Further reproduction prohibited without permission.

available center-of-mass energy, longitudinal momentum, and transverse momentum independently, but instead it is seen that if one uses the ratio of the longitudinal momentum to the energy in the center of mass frame as a variable, the inclusive distributions can be fitted well with only two quantities, namely, the transverse momentum (p_t) and this "scaling" variable, called Feynman x (x_F); i.e.

$$\frac{d\sigma}{dx_F dp_t^2}(x_F, E, p_t) = \frac{d\sigma}{dx_F dp_t^2}(x_F, p_t)$$

1.2. Hard Scattering Models

While the data presented in this thesis are at low transverse momenta (below about 1 GeV/c), our experiment does have the capability of studying inclusive reactions up to about 4 or 5 GeV/c, where the predictions of hard scattering models are relevant. Since these models are currently of great interest, I will briefly mention some of them, indicating their major predictions.

In hard scattering models, high-transverse-momentum particle production is due to the collisions of constituents of hadrons. If the constituents are point-like, structureless particles (like the electron), dimensional counting rules predict that the transverse momentum dependence of the inclusive cross section should be p_t^{-4}. This does not agree with inclusive distributions such as pp --> π^0 X, where a

Reproduced with permission of the copyright owner. Further reproduction prohibited without permission.

p_t^{-8} behavior is observed in the p_t range from 2 to 5 GeV/c [Angelis 78 and Clark 78].

To remedy this situation, Blankenbecler and others proposed the Constituent Interchange Model (CIM), whereby the constituents that are responsible for high-transverse-momentum particle production are not necessarily point-like [Gunion 72, Blankenbecler 74 and 78, and Jones 79]. A number of processes are possible, each with a different p dependence, allowing a complicated overall behavior. The data generally agree with this model, in particular, inclusive photoproduction results below 20 GeV with transverse momenta in the 1 to 2 GeV/c range have been compared to CIM predictions [Eisner 74 and Boyarski 76].

For the particular case of large-transverse-momentum photoproduction of single photons ("deeply inelastic Compton" scattering), Bjorken and Paschos derived a relation between electroproduction and photoproduction in the deeply inelastic region [Bjorken 69]. They assumed that the photon scatters off partons inside the proton as is illustrated in Figure 1-1. Since the photon couples to the partons via their electric charge, they obtained the following relation:

$$\frac{d\sigma^{\gamma p}}{d\Omega dE'} = \frac{\nu^2}{EE'} \frac{d\sigma^{ep}}{d\Omega dE'} \frac{<\Sigma Q_i^4>}{<\Sigma Q_i^2>}$$

where E and E' are the energies of the initial and final photon (measured in the laboratory frame), $\nu = E-E'$, and Q_i is the charge of the ith parton. This formula can be used

Reproduced with permission of the copyright owner. Further reproduction prohibited without permission.

Figure 1-1

Feynman Graphs for Inelastic Scattering

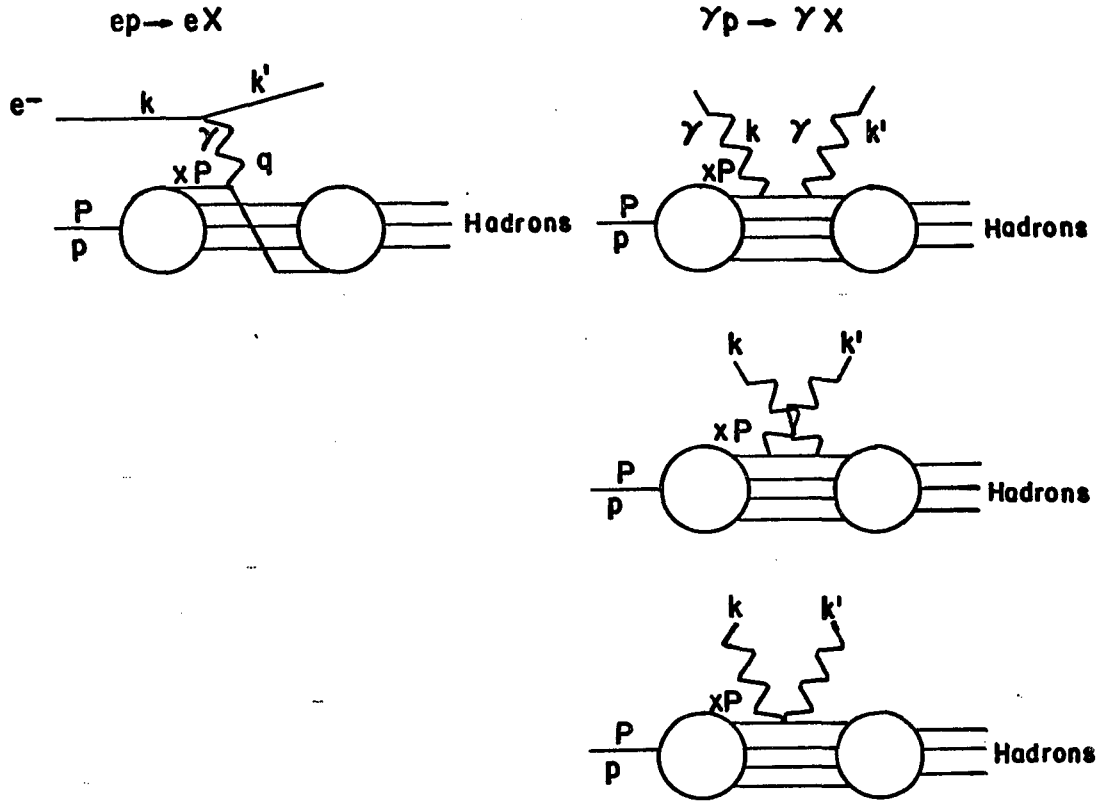

Reproduced with permission of the copyright owner. Further reproduction prohibited without permission.

to determine whether the partons are integrally or fractionally charged.

Experimentally it is difficult to separate single photons due to this process from those due to decays of other particles, predominantly π^0's and η's. One of the major goals of this experiment is to measure this process. The understanding of inclusive photoproduction of π^0 and η mesons is essential to this measurement.

1.3. Soft Scattering Models

To model the complex behavior of low-transverse-momentum particle production, it is necessary to take a phenomenological approach. The Vector Dominance Model (VDM) assumes that the photon couples to hadrons via vector mesons, notably the ρ^0, ω, and ϕ. The model makes a number of detailed predictions for the photon-proton total cross section and several exclusive processes, including elastic scattering. A further discussion of this model, including comparisons of its predictions with a large variety of data can be found in an excellent review article [Bauer 78].

For inclusive scattering a different approach has been taken. Seiden, Field, and others [Seiden 76, 77, and 78 and Field 78a, 78b, and 79] have developed a simple Monte Carlo model which describes many features of inclusive scattering quite well with an amazingly small amount of phenomenological input. These models envision multiparticle production

Reproduced with permission of the copyright owner. Further reproduction prohibited without permission.

Figure 1-2

Quark Cascade Model

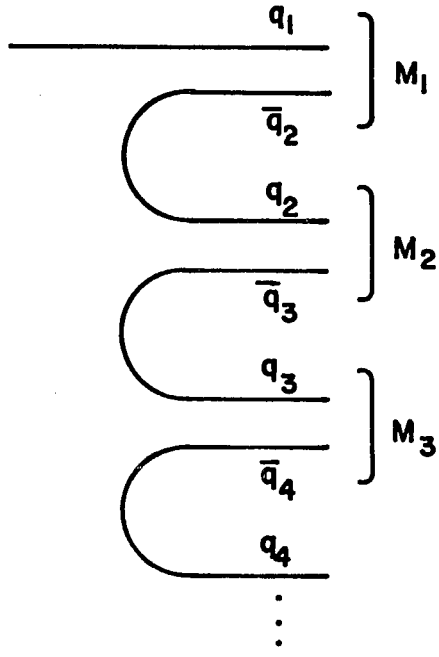

Reproduced with permission of the copyright owner. Further reproduction prohibited without permission.

as a cascade process, depicted in Figure 1-2, in which an isolated quark combines with an antiquark from a quark-antiquark pair in the sea to form a meson which can then decay to produce other mesons. The quark that is left combines with another antiquark to form another meson and the process continues. The key function involved is the energy-sharing function, f(z), which gives the probability that the meson produced has a fraction z of the parent quark's energy. This is generally parametrized to fit inclusive charged pion data. Also the transverse momentum of quarks must be parametrized and put into the model. Other assumptions which vary from model to model are the probabilities for producing each type of quark and the vector meson to pseudoscalar meson production ratio. Typically such models ignore high mass quarks (charmed and bottom quarks) and the production of baryons or mesons not in the pseudoscalar or vector nonets. In fact the whole basis of the model is contradictory to the theoretical notion that the beam and target fragmentation products are made at a later time than the particles in the central region. This point as well as other critiques of the model are discussed in [Field 78a].

Because of their general nature, quark cascade models can be used to simulate the data from a number of different reactions. We use a quark cascade model in our Monte Carlo program that simulates inclusive particle production.

Reproduced with permission of the copyright owner. Further reproduction prohibited without permission.

We also compare our data to those of other similar reactions. In particular we compare our data to those from low energy photoproduction [Berger 73], low energy electroproduction [Berger 77], and high energy electroproduction [Loomis 79] experiments. The comparison to electroproduction experiments is particularly interesting since it involves the comparison of the hadronic nature of real and virtual photons.

Reproduced with permission of the copyright owner. Further reproduction prohibited without permission.

Chapter 2

Description of Experimental Apparatus

The experiment is designed to simultaneously collect data for several processes with quite different kinematical parameters. Elastic photon-proton scattering and quasi-elastic neutral meson production require identification of the recoil proton while rejecting events in which nucleon resonances are formed. They also produce low-transverse-momentum photons which deposit nearly the entire beam energy into the forward detector. On the other hand inclusive photon, neutral pion, and eta production can produce lower energy photons at larger angles. The small opening angle of photon pairs from high energy neutral pion decays requires good position and energy resolution in the forward detector to separate single showers from pairs of showers. This is essential to the measurement of deep inelastic single photon production. Typical resolution parameters required of the forward detector are an energy resolution of a few per cent at 100 GeV energies with a position resolution of 1 cm, corresponding to an angular resolution of .3 mr, for forward going photons. For the recoil proton a drift chamber position resolution of 1 mm and a time-of-flight counter time resolution of 1 ns are sufficient over most of the momentum transfer range accessible to the experiment.

Reproduced with permission of the copyright owner. Further reproduction prohibited without permission.

The rest of this chapter consists of a description of the major elements of the experiment: the beam line, tagging system, hydrogen target, and detection apparatus. I will be quite brief in my discussion of the first two items since they are more fully described elsewhere [Halliwell 72, Garbincius 76 and 78, Cumalat 77, and Egloff 79].

2.1. Beam Line

Protons from the accelerator are directed onto a beryllium target where they produce, among other things, neutral pions which decay primarily to pairs of photons. These photons, along with other neutral particles, are allowed to propagate several meters through a magnetic field which bends the charged particles into a beam dump. A lead foil is inserted into the beam to convert photons to electron-positron pairs. The electrons are bent away to form a secondary beam, while most of the positively charged particles and neutrals are deposited into a beam dump. The major contamination of the electron beam is from negative pions produced by neutrons interacting in the lead foil.

Beryllium is chosen as the primary target material to minimize the ratio of collision length to radiation length since one wants to maximize neutral pion production while minimizing the conversion of photons before the converter. The beryllium target thickness of 36 cm (1.2 collision lengths, 1.0 radiation lengths) and the lead converter

Reproduced with permission of the copyright owner. Further reproduction prohibited without permission.

thickness of .125 inches (.57 radiation lengths) are chosen to maximize the electron yield while minimizing the negative pion contamination. (See [Halliwell 72] for more details.) The π^-/e^- ratio was measured to be .003 to .004 at 115 GeV by a previous experiment [Davis 74]. The yield of electrons produced by 400 GeV protons is shown in Figure 2-1.

The electrons produced in the lead converter then go through a series of magnets and collimators which define the size and momentum of the beam. The beamline is shown schematically in Figure 2-2. This electron beam is used for the calibration of the shower counters in the forward detector and to check out the entire apparatus and analysis programs with electron-proton elastic scattering. For the latter measurements, the lead converter is replaced by a .008 inch thick copper foil (.014 radiation length) to reduce the electron flux while leaving the collimator settings the same.

2.2. Tagging System

The tagging system (Figure 2-3), which converts the electron beam into a photon beam of known energy, consists of a thin copper radiator, a series of bending magnets, a scintillation counter hodoscope to measure the position of the deflected electrons and a set of lead glass blocks which measure the electron's energy as a cross check on the momentum measurement provided by the tagging hodoscope. With

Reproduced with permission of the copyright owner. Further reproduction prohibited without permission.

Figure 2-1

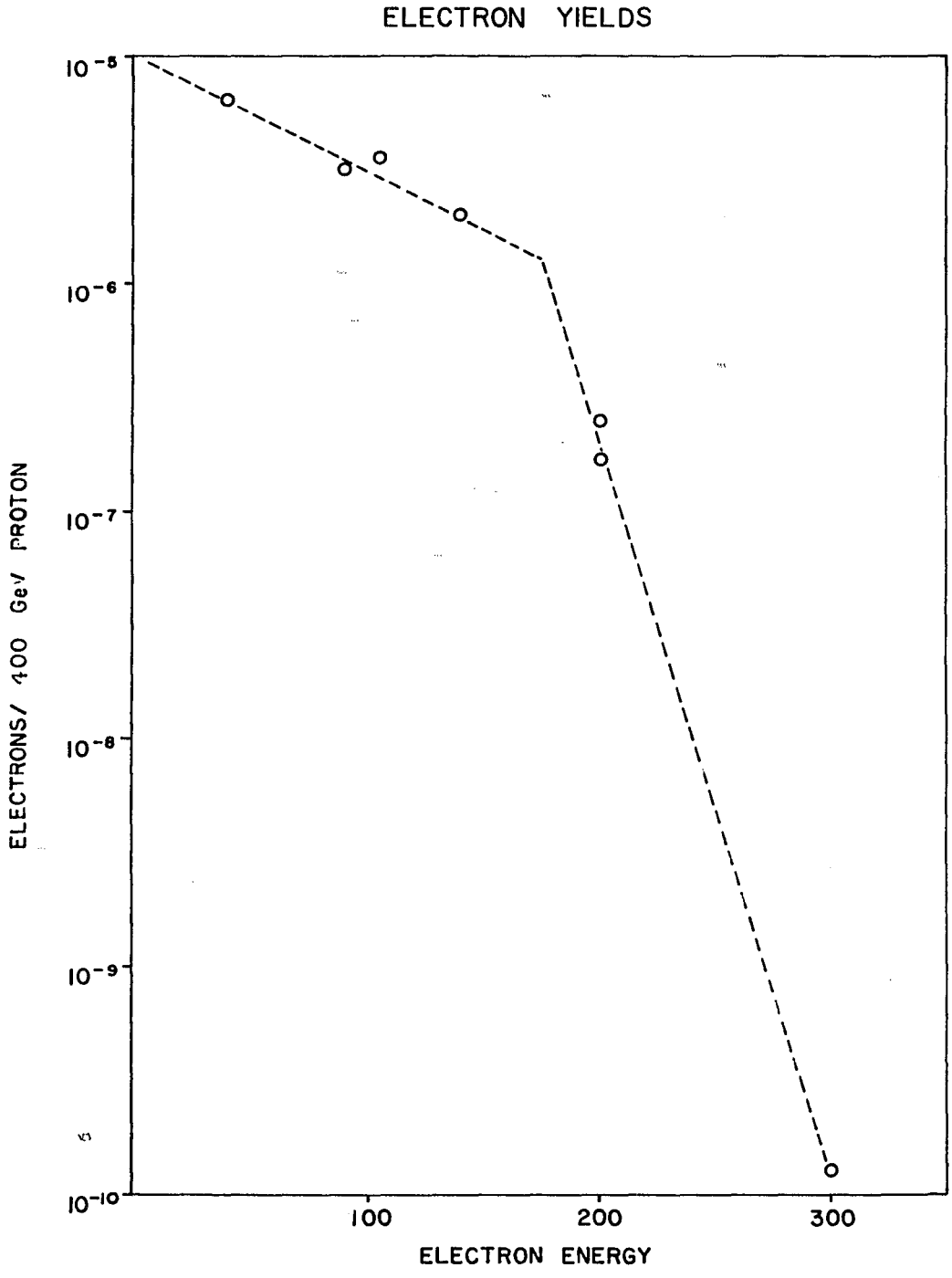

Reproduced with permission of the copyright owner. Further reproduction prohibited without permission.

Figure 2-2

Electron Beam Line Schematic

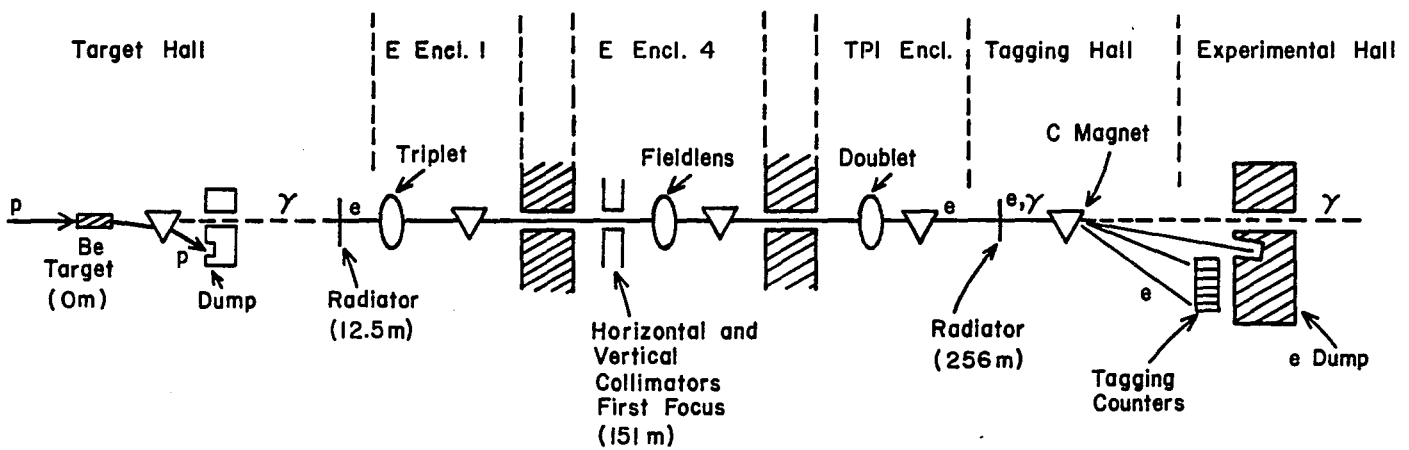

Reproduced with permission of the copyright owner. Further reproduction prohibited without permission.

Figure 2-3

TAGGING SYSTEM SCHEMATIC

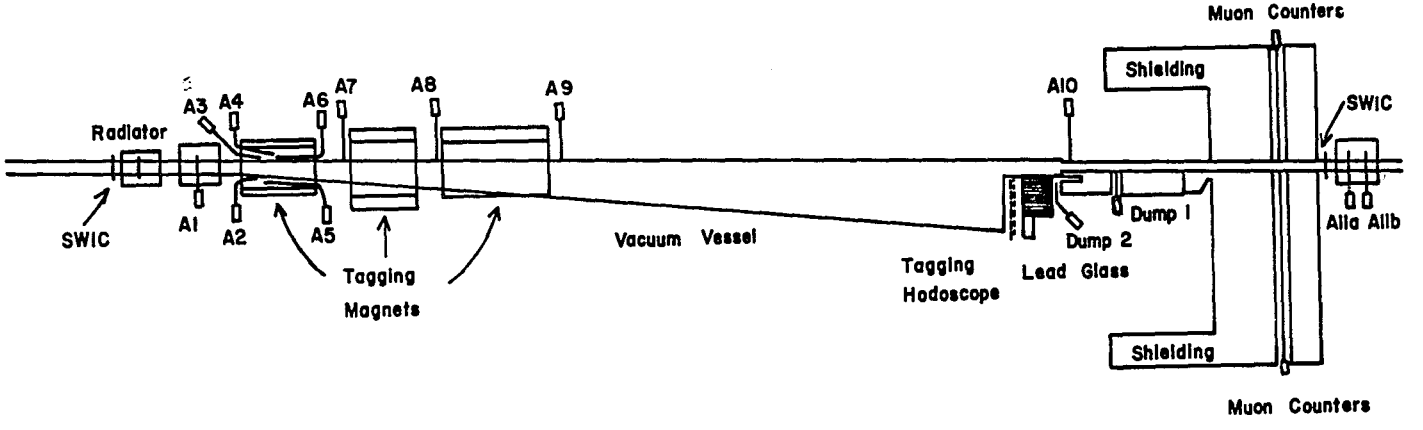

Reproduced with permission of the copyright owner. Further reproduction prohibited without permission.

this arrangement photons containing approximately 45% to 90% of the incoming beam energy are tagged. A typical flux is 2 x 10^5 tags per pulse of 3 x 10^{12} 400 GeV/c protons for a 135 GeV electron beam and a 5.5% r.l. copper radiator. Further details may be found in [Breakstone 80 and Grillo 80] as well as the previously-given references.

2.3. Hydrogen Target

This target consists of a 3 cm diameter, 75 cm long mylar flask containing liquid hydrogen (Figure 2-4). The diameter is just large enough to contain the beam. The thickness of the walls, insulation, and supporting structures around the target are kept as small as possible to minimize the amount of material traversed by recoil protons produced in elastic scattering and quasi-elastic vector meson production. On the average protons with a kinetic energy greater than 25 MeV (corresponding to $|t| > .05$ $(GeV/c)^2$ in elastic scattering) will be able to leave the target. The length of the target represents approximately .1 radiation length. This is chosen as a compromise between a large event rate and a low electromagnetic background. More details on the design of the hydrogen target are in [Grillo 80].

2.4. Detection Apparatus

The two major elements of the detection apparatus are a

Reproduced with permission of the copyright owner. Further reproduction prohibited without permission.

Figure 2-4

Liquid Hydrogen Target Assembly

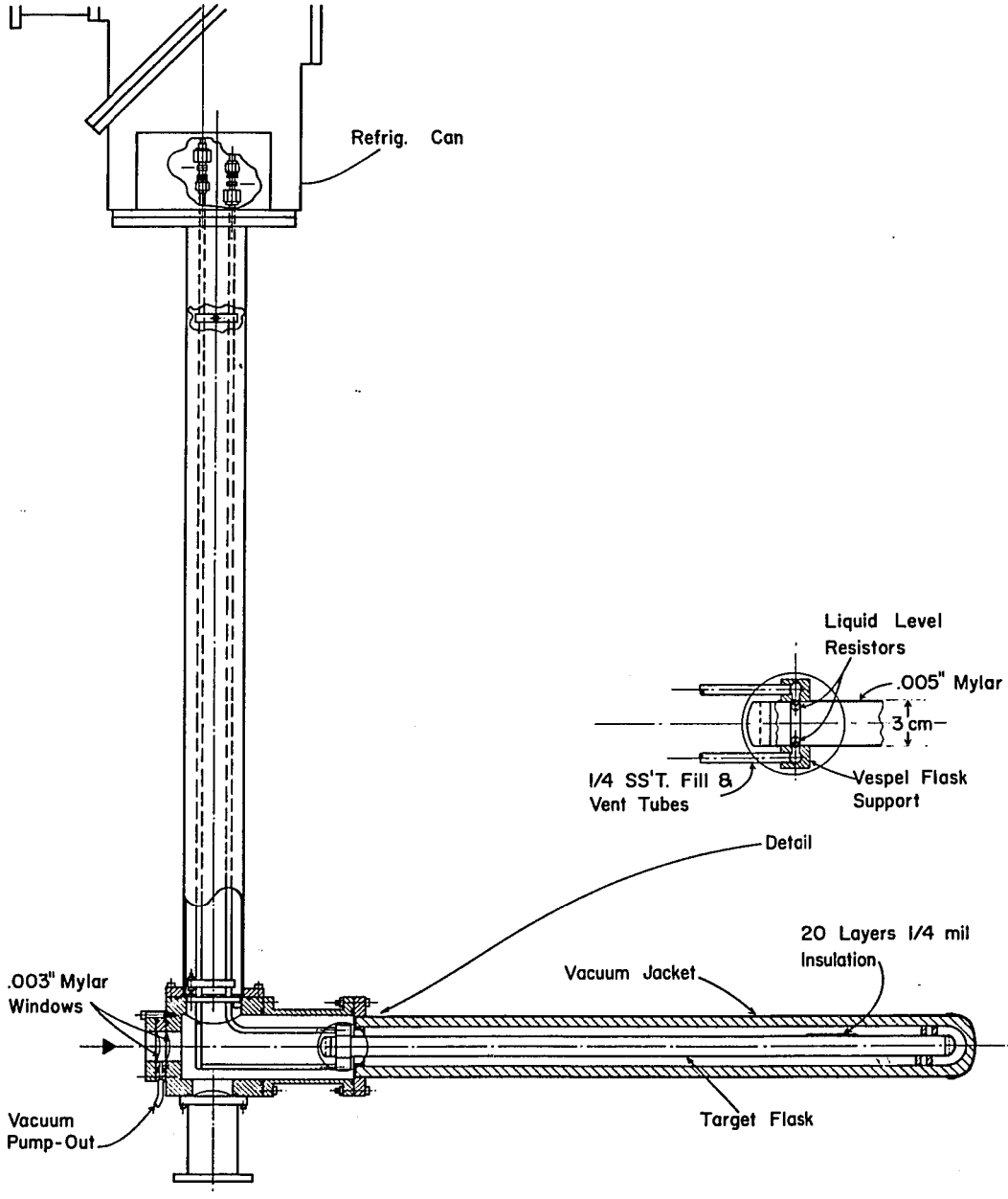

Reproduced with permission of the copyright owner. Further reproduction prohibited without permission.

set of drift chambers and time-of-flight (TOF) counters surrounding the target and an electromagnetic shower spectrometer in the forward direction. The experimental layout is shown in Figure 2-5.

Surrounding the target are two layers of drift chambers, each with four sense wire planes, and a layer of scintillation counters. They combine to measure the trajectory and time-of-flight of recoil particles (Figure 2-6). The detector spans the full azimuthal angle with a total of 80° ($4 \times 20^{\circ}$) dead angle due to the frames of the drift chambers. It subtends a polar angle from 45° to 90° in the lab. Each module of drift chambers has four planes of sense wires at 90°, 0°, 72°, and 108° with respect to the beam direction, thus giving four measurements of the particle's trajectory. A typical drift cell (shown in Figure 2-7) consists of a sense wire at a potential of +2.4 kV and a field wire at -4.9 kV. The drift cell size is 4 cm from sense wire to field wire. Above and below are a set of field wires with 2 mm spacing. We use pure ethylene gas in the chambers to avoid the complexities of a mixed gas system. [Palladino 80] contains many more details on the design and performance of these chambers.

The 16 time-of-flight counters form a barrel around the target with the center of each counter 1 m from the axis of the hydrogen target. The scintillator is half-inch thick NE-110 with an area of 150 cm by 40 cm. The light pipe is

Reproduced with permission of the copyright owner. Further reproduction prohibited without permission.

Figure 2-5

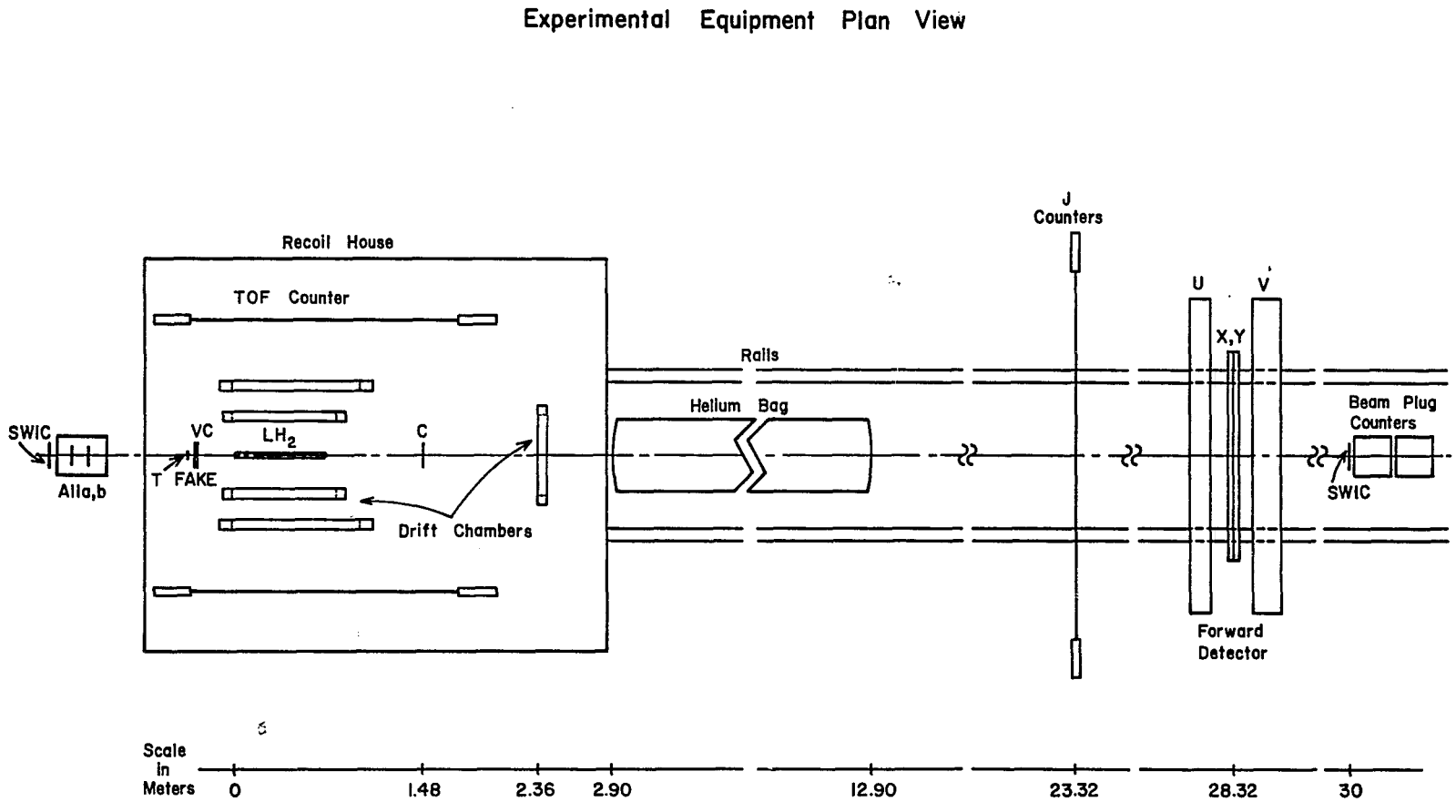

Reproduced with permission of the copyright owner. Further reproduction prohibited without permission.

Figure 2-6

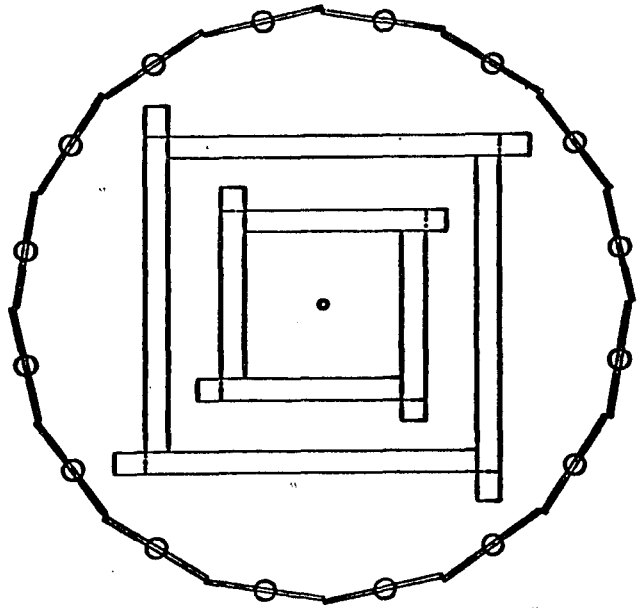

a) Recoil detector: front view

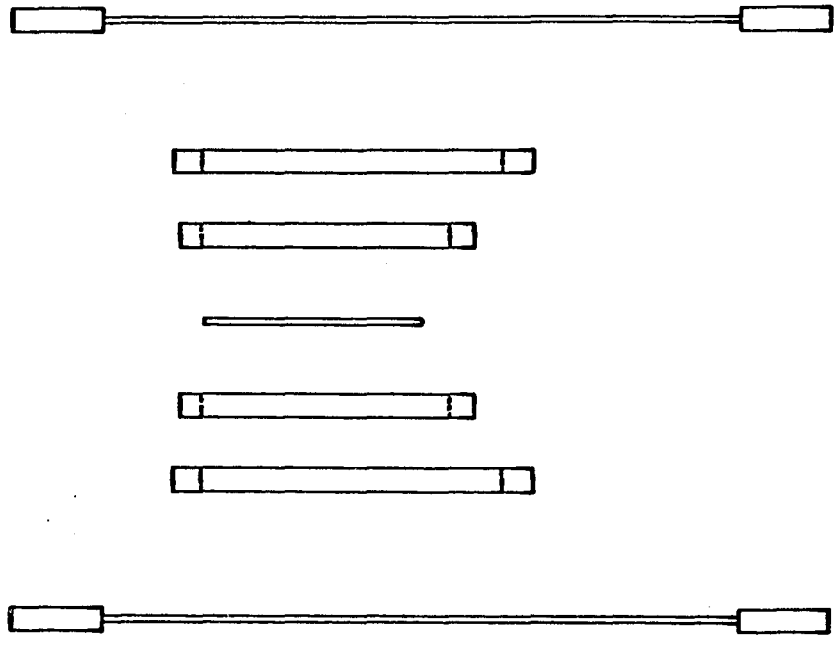

b) Recoil detector: side view

Reproduced with permission of the copyright owner. Further reproduction prohibited without permission.

Figure 2-7

Typical Drift Cell

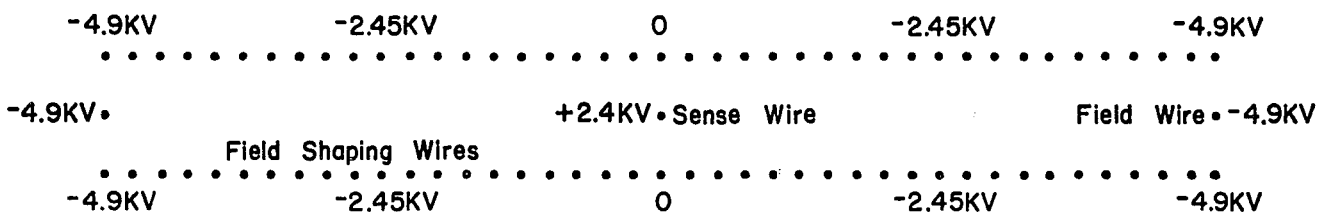

Reproduced with permission of the copyright owner. Further reproduction prohibited without permission.

simply a half-inch thick plexiglass sheet of a trapezoidal shape tapering down from 40 cm to 5 cm over a distance of 30 cm (Figure 2-8). Details of the design of these counters may be found in [Grillo 80].

The entire recoil detector is mounted on a cart (Figure 2-9) in an environmentally isolated house which provides a dehumidified atmosphere as well as electrostatic shielding which is necessary for proper functioning of the drift chambers. The cart rides on a set of rails which allows the detector to be moved outside the house so it can be accessed for repairs, additions, etc.

The forward electromagnetic shower spectrometer (Figures 2-10 and 2-11) consists of two banks of lead-acrylic plastic sandwich Cherenkov counters separated by a scintillator hodoscope. The front bank of shower counters, called the U counters, contains eight quarter-inch thick sheets of lead for a total thickness of 9.0 radiation lengths. The back bank of shower counters, called the V counters, contains nine quarter-inch thick sheets of lead with a total thickness of 10.2 radiation lengths. Each shower counter has an active area of 18 cm x 72 cm. The scintillator hodoscope consists of two identical sets of scintillation counters at right angles to each other. Each counter is 158 cm long x 3 cm wide x 2.5 cm thick with the exception of the counters around the beam hole which are 92 cm x 2 cm x 2.5 cm. There are a total of 112 of these hodoscope counters.

Reproduced with permission of the copyright owner. Further reproduction prohibited without permission.

Figure 2-8

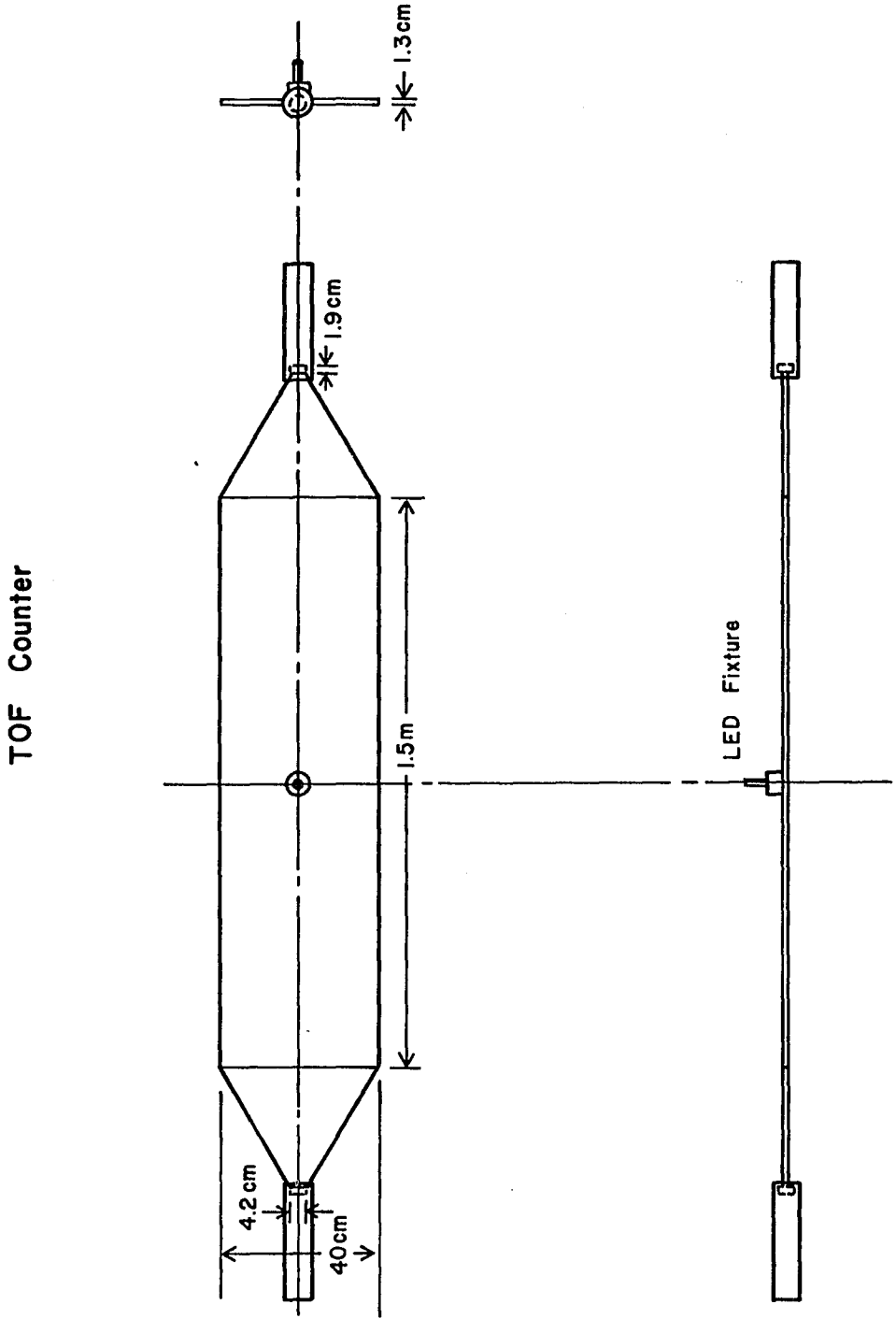

Reproduced with permission of the copyright owner. Further reproduction prohibited without permission.

Figure 2-9

Recoil Detector Assembly

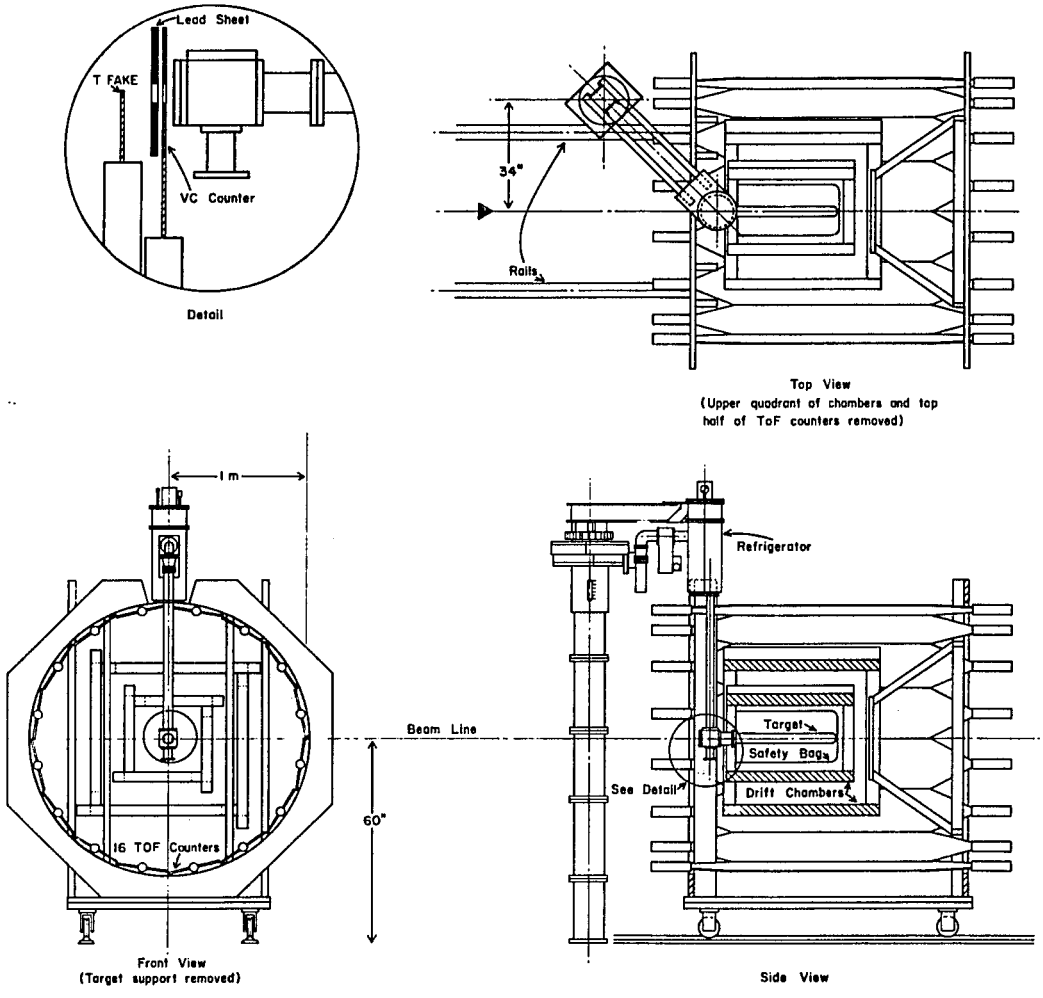

Reproduced with permission of the copyright owner. Further reproduction prohibited without permission.

Figure 2-10

Forward Detector Assembly: side view

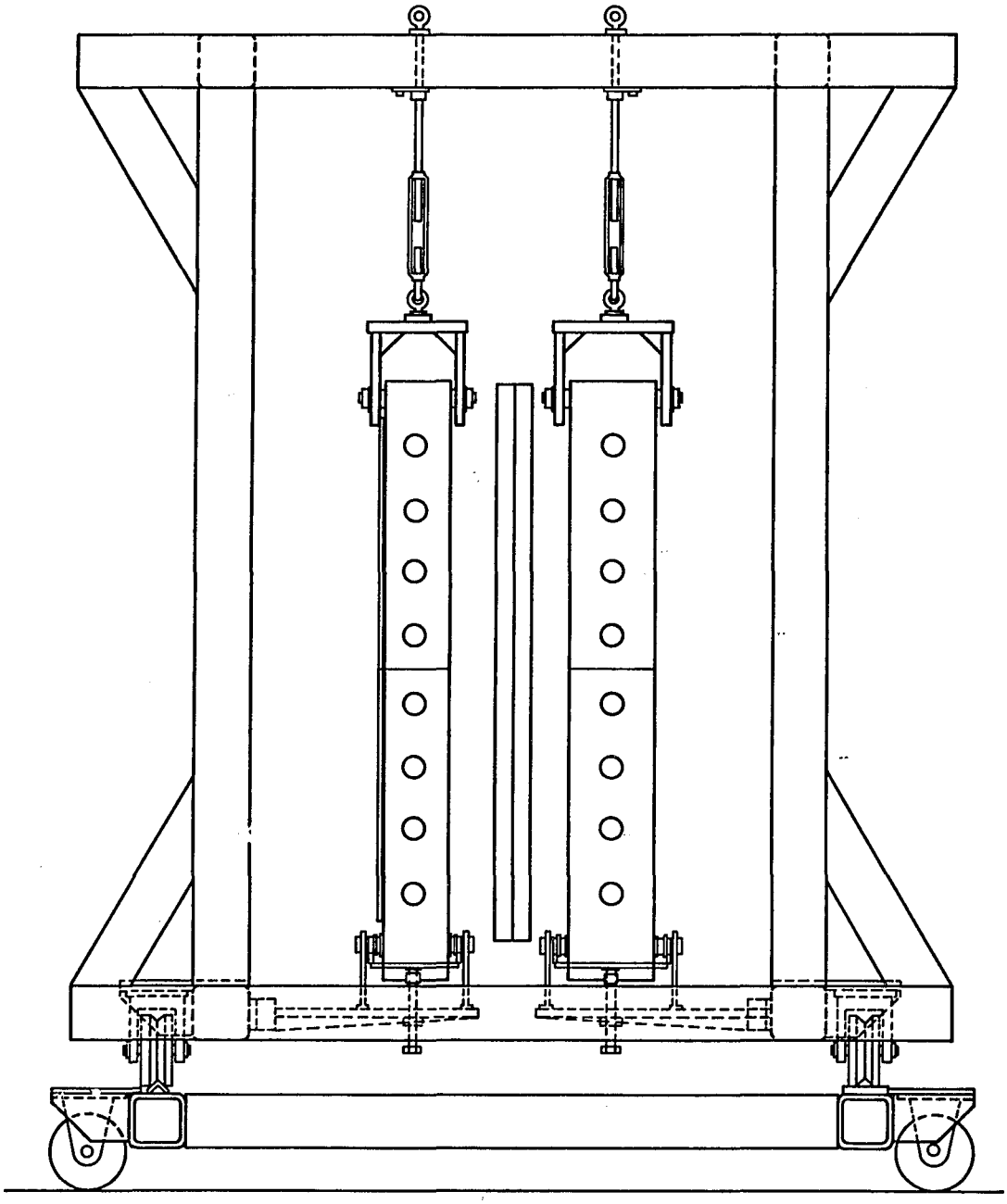

Reproduced with permission of the copyright owner. Further reproduction prohibited without permission.

Figure 2-11

Forward Detector Assembly: front view

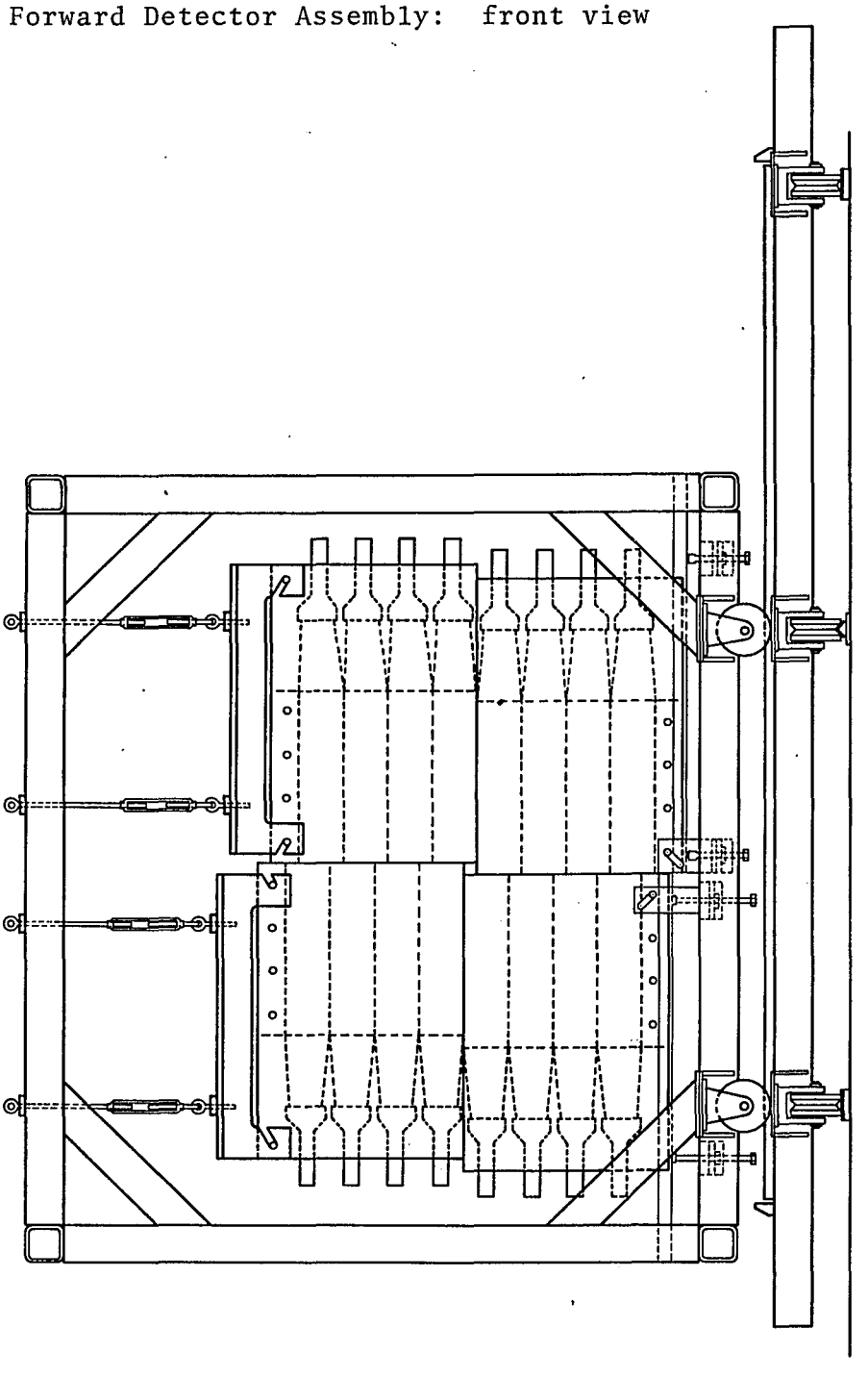

Reproduced with permission of the copyright owner. Further reproduction prohibited without permission.

Each counter in the forward detector uses a ten-stage phototube with a bialkali photocathode. Further details on the design and construction of these counters may be found in Appendix A. The entire assembly of shower counters and scintillator hodoscope is mounted on a cart which allows side-to-side motion transverse to the beamline. This cart is, in turn, mounted on a cart which can move upstream or downstream over a range of roughly 25 m on a set of rails. This arrangement allows great kinematic flexibility and provides a relatively easy way to calibrate the detector in place.

In the far forward direction, covering the beam hole in the forward detector, we have a set of two shower counters (the "beam plug" counters in Figure 2-5), one behind the other, to monitor the beam and to measure the energy of showers which go through the beam hole in the forward detector in multi-photon events. The upstream counter is a lead-acrylic plastic sandwich counter, while the downstream counter is a lead-scintillator sandwich. Each counter has 16 layers. The total thickness of lead is 28 radiation lengths. The active area of the counters is approximately 20 cm horizontally by 30 cm vertically with the beam centered on the counter. These counters are at a fixed position 30 m downstream of the hydrogen target. Just upstream of the beam plug counter we have a segmented wire ionization chamber (SWIC), provided by Fermilab, to measure the beam position and shape.

Reproduced with permission of the copyright owner. Further reproduction prohibited without permission.

Just upstream of the forward detector we have a set of half-inch-thick scintillation counters (the J counters in Figure 2-5) to latch charged particles which would hit the shower counters (Figure 2-12), while just downstream of the target we have a set of four planes of drift chambers with an active area of 60 cm horizontally by 80 cm vertically. However, because of the relatively long drift time (up to 800 ns) and the high rates of charged particles in the beam from Bethe-Heitler pairs, the central wires in the drift chamber are essentially always on, severely limiting the usefulness of this chamber. As a substitute for this chamber, we placed a scintillation counter (the C counter in Figure 2-5) of dimensions 20 cm x 20 cm x 1/4 inch thick approximately 1 m downstream from the end of the hydrogen target. The counter has a 6 cm diameter hole in its center which shadows the active area of the forward detector so that we minimize the amount of material that the scattered photons go through on their way to the shower counters.

Immediately upstream of the target we have a scintillation counter (VC in Figure 2-5) also of dimensions 20 cm x 20 cm x 1/4 inch thick, but with a 3 cm diameter hole in its center which we use to veto beam halo particles and events in which the photon interacts upstream of the hydrogen target. This counter is very important in that it reduces the trigger rate by a factor ranging from two to ten, depending on the beam conditions and the position and shower energy threshold of the forward detector which is used for the

Reproduced with permission of the copyright owner. Further reproduction prohibited without permission.

Figure 2-12

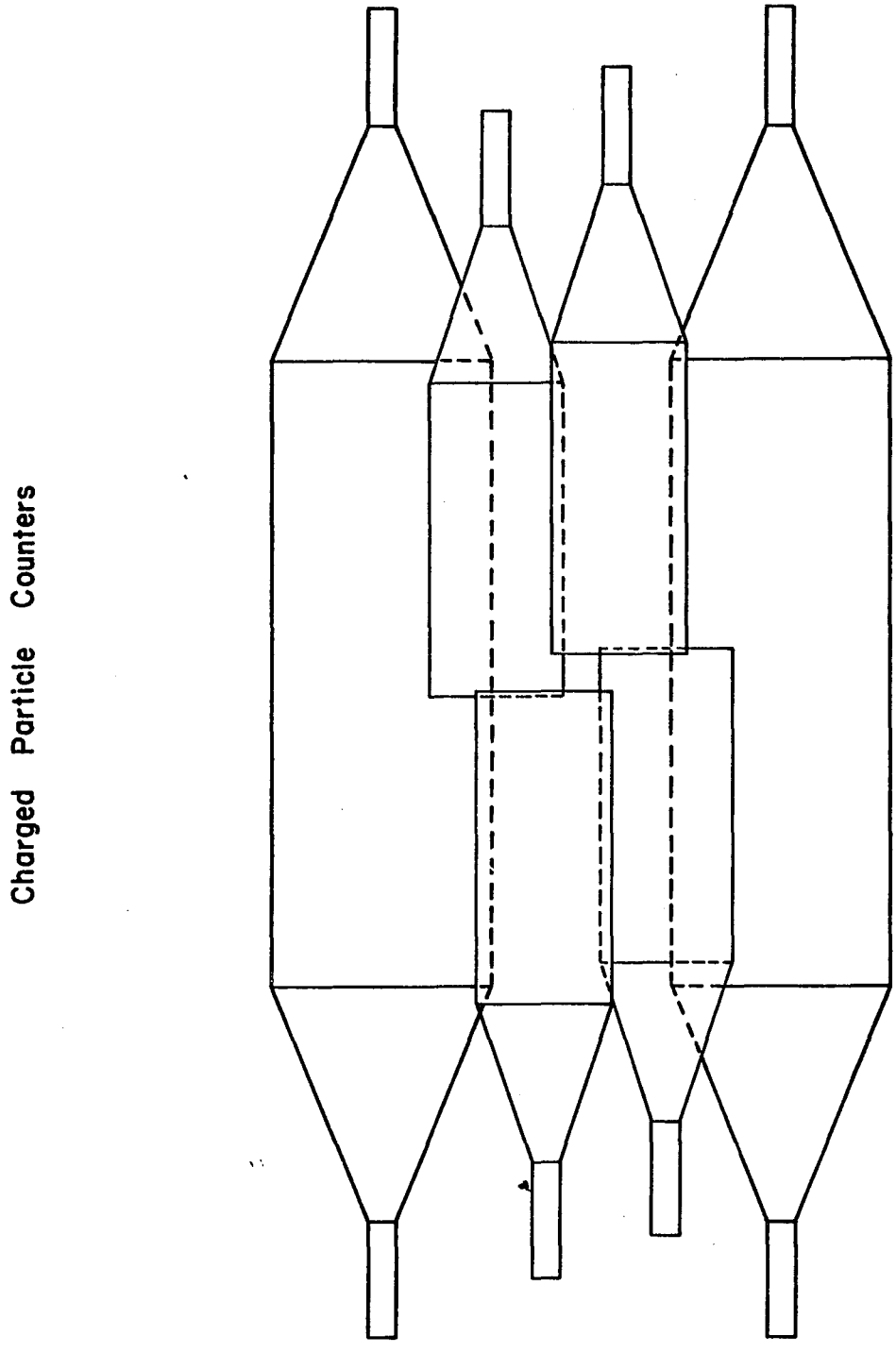

Reproduced with permission of the copyright owner. Further reproduction prohibited without permission.

event trigger.

In addition to the VC counter, we installed a small scintillation counter (TFAKE in Figure 2-5), 2 cm x 2 cm x 1/4 inch thick, which is put in the beam only when we run an electron beam into the target for various calibration purposes. Its sole purpose is to provide a signal to the fast logic to be used instead of the usual tag signal when we are in data taking mode.

Finally we have a 10 m long by 56 cm diameter helium bag just downstream of the recoil house. It is used to reduce the number of interactions of photons downstream of the target. This bag was removed for data taking with the forward detector in the 10 m position.

Reproduced with permission of the copyright owner. Further reproduction prohibited without permission.

Chapter 3

Data Collection Procedure

In the following sections I will briefly describe the system used to collect and store the data for this experiment. We used conventional fast logic to decide what constituted an event and only collected data when the counter hits satisfied the trigger criteria. In addition several different triggers were used to monitor the performance of the apparatus. The data were read into a computer via a CAMAC system, which consists of a set of standardized electronic modules addressed by the computer that provides an interface between the signals coming in from the counters (or other sources) and the computer. These data were processed by the computer and written onto magnetic tapes to be analysed at a later time.

After describing the hardware I will discuss the procedures used to set up the experiment and collect the data. The actual data taking was preceded by an approximately one-week period of calibration of the apparatus. Also at this time the monitors were recorded so that they could provide gain tracking of all the phototubes in the forward detector throughout the experiment. Once we felt we understood the apparatus, we began data taking while continually checking the integrity of the apparatus using the data

Reproduced with permission of the copyright owner. Further reproduction prohibited without permission.

itself as well as the various monitors described in Section 3.5.

3.1. Trigger Logic

The event trigger used for the experiment required a coincidence of the following elements:

1) a beam gate
2) a good tag
3) a pulse height in the front bank of shower counters (U plane) above a certain threshold
4) a pulse height in the total absorption counters (sum of U and V planes) above a certain threshold

in anticoincidence with the veto counter labeled VC in Figure 2-5. Figure 3-1 gives a block diagram of the trigger logic. The threshold for showers in the total absorption counters was varied by changing an attenuator at the input to the discriminator where the summed signal from the U and V planes arrived. This was done to make the trigger threshold easily reproducible, since it was changed several times during the course of the experiment. The bulk of the data was taken with the U + V threshold set to correspond to 34 GeV showers with the requirement that the energy deposition in the U plane exceeds a minimum of 3 GeV.

Various other triggers existed to monitor the tagging system and the detection apparatus. In this section I will briefly describe each of them. Further details are in [Breakstone 80].

Reproduced with permission of the copyright owner. Further reproduction prohibited without permission.

Figure 3-1

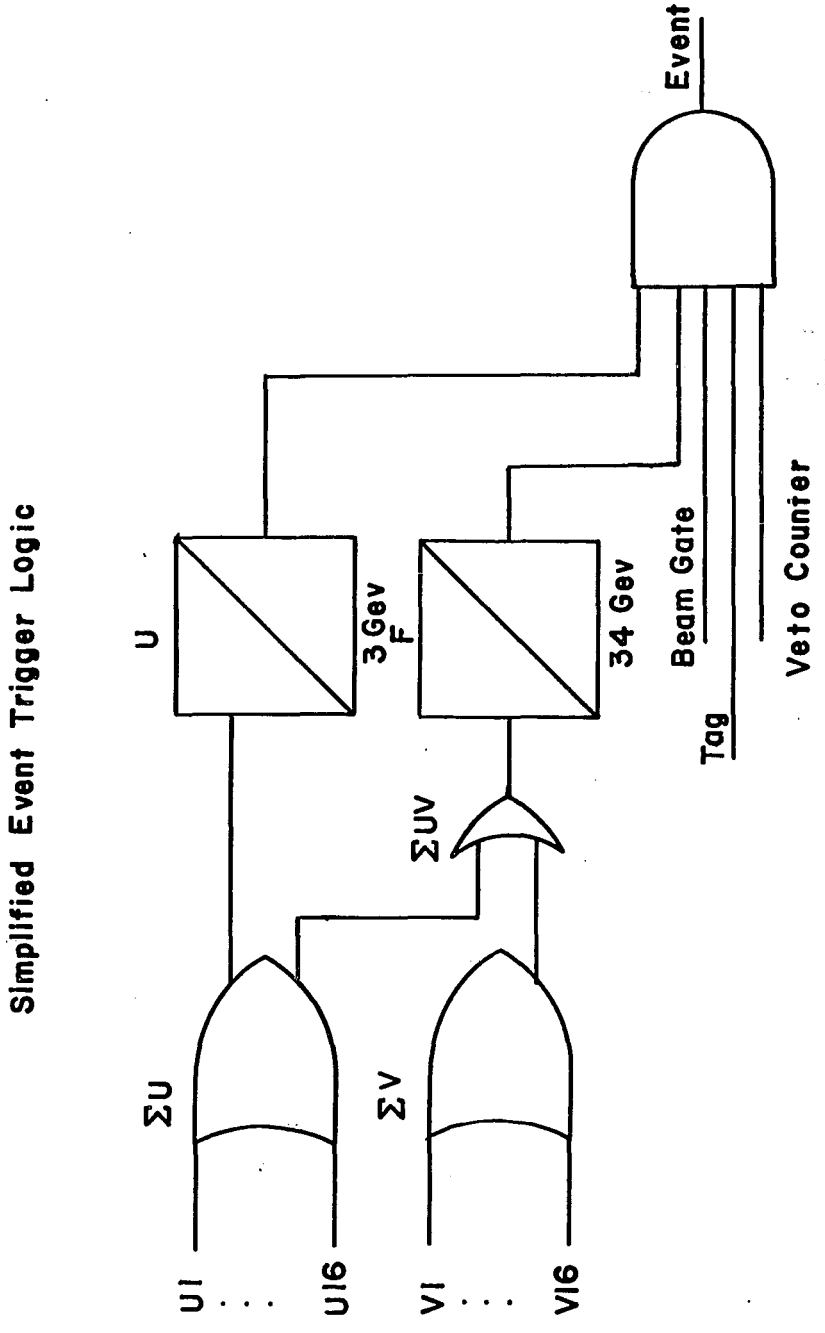

Reproduced with permission of the copyright owner. Further reproduction prohibited without permission.

The simplest of these triggers was a pedestal trigger which used a pulse generator to trigger the ADC gate generation logic. This was done during the beam spill as well as out of spill to provide a check that the ADC gates were being generated properly. The pedestal triggers were used for calculating the value of the ADC pedestals which were then cross-checked by another method during the analysis of the data. I discuss this further in Sections 4.2.1. and 4.2.4.

To monitor the tagging system we set up a trigger consisting of a coincidence of the beam plug counters with the tagging system (T·BP). A coincidence with a gate generator allowed us to manually vary the rate of this trigger.

For the recoil detector we had a trigger which used a coincidence of the time-of-flight (TOF) counters with either the tag or the forward detector or both. This was originally intended to be an alternative type of event trigger, but the rates due to delta ray production from Bethe-Heitler pairs produced in the target was too large to permit this, so we merely counted the number of these triggers. In addition, to provide straight tracks for aligning the drift chambers, we used a coincidence of various sets of TOF counters to define a cosmic ray trigger.

Several monitoring systems were used for the forward detector: passing muons, americium sources, and light-emitting diodes (LED's) for the total absorption counters,

Reproduced with permission of the copyright owner. Further reproduction prohibited without permission.

the latter two only for the hodoscope. The trigger logic for all of these as well as for the time-of-flight LED system is discussed in detail in Appendix C.

Finally we had a trigger to provide a beginning- and end-of-beam-spill pulse to the computer as well as a beam gate to use in coincidence with the event trigger. The timing information was provided by signals generated by the accelerator via a CAMAC unit.

3.2. CAMAC and Computer

The data were read in by a NOVA 840 minicomputer via a CAMAC branch system. The data consist of a set of integer numbers from the various CAMAC units: pulse heights of the lead glass, time-of-flight, beam plug, hodoscope, and total absorption counters from the analog-to-digital converters (ADC's), time-of-flight information from one set of time-to-digital converters (TDC's), drift chamber drift times from a different type of TDC, and counter latches and scalers which recorded hits and rates on all the counters and triggers used in the experiment.

3.2.1. CAMAC System

The CAMAC branch system consists of a series of CAMAC crates, each one with its own crate controller module. The crate controllers were daisy-chained together, with the far end terminated and the front end going to a master

Reproduced with permission of the copyright owner. Further reproduction prohibited without permission.

controller which communicated with the computer. Event and monitor triggers signaled the computer via a CAMAC priority interrupt module. It basically functioned as a NIM input register but had the capability to interrupt the computer from whatever it was doing and tell it to read the various CAMAC units. The structure of the data taking program was such that it read in events with the following priorities:

1) beam start
2) beam stop
3) real events
4) U/V americium
5) U/V LED
6) U/V muon
7) X/Y LED
8) X/Y americium
9) TOF LED
10) Tag-beam plug (T·BP)
11) Pedestal

3.2.2. Computer Configuration and Data Flow

The configuration of the NOVA 840 minicomputer and its peripherals is shown in Figure 3-2. It consists of a central processor with 48K of main-frame core memory, 256K of outboard memory, a moving head disk, two tape drives, a line printer, a storage display unit (oscilloscope) with a digital-to-analog converter (DAC), a teletype, and two CAMAC interfaces.

The experiment was controlled almost exclusively by the computer via commands typed into the teletype. The software was written such that there were two separate programs running at any one time in a foreground/background environment.

Reproduced with permission of the copyright owner. Further reproduction prohibited without permission.

Reproduced with permission of the copyright owner. Further reproduction prohibited without permission.

Figure 3-2

NOVA 840 Configuration

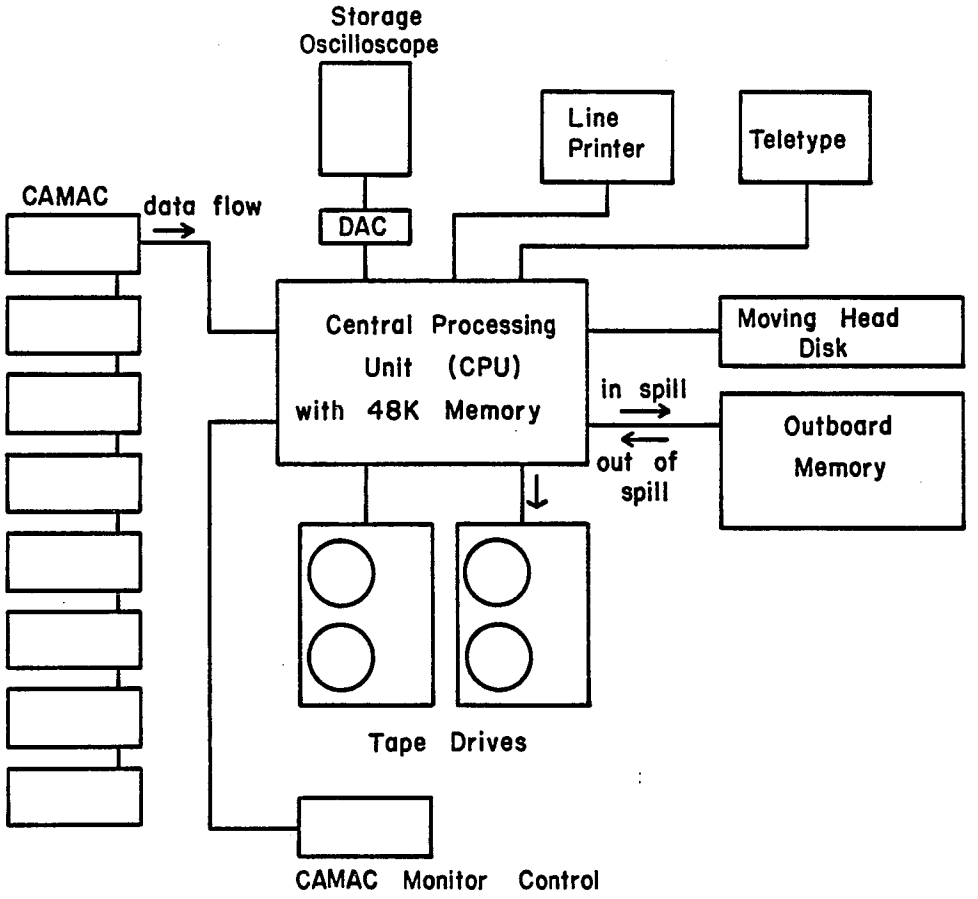

The foreground program controlled CAMAC. When an interrupt from an event came, it read the data into core. When time was available during the beam spill, the data were transferred to the outboard memory. Then at the end of the spill the data were written onto magnetic tape from the outboard memory. Communication with the background was kept to a minimum. The background program was a multi-task program that allowed the person on shift to control the experiment through a set of teletype commands and to monitor the experiment using a set of on-line checks. The foreground and background programs and their support routines resided on the moving head disk and were brought into core for execution by a set of commands typed in on the teletype. More details on the on-line data collection programs may be found in [Grillo 80].

3.3. Setup of the Experiment

The final assembly of the experiment occurred in September and October of 1977. During the preceding two years we had been building the pieces of the detection apparatus and had been setting up as much as possible without interfering with the then running experiment. By this time nearly all of the detectors had arrived at Fermilab for assembly. The physical layout of the Tagged Photon Lab is such that there is a large underground pit for the beam and detection apparatus and a ground-level counting room which houses most of the trigger logic, the computer, various

Reproduced with permission of the copyright owner. Further reproduction prohibited without permission.

monitors and controls, and, of course, the experimenters.

The physical setup of the experiment culminated in an approximately one-month-long setup run during which we did the timing of the trigger logic, tested and set high voltages on all the counters and drift chambers, did preliminary checks on the monitors, tuned the beam, and so on. One of the most important things we did at this time was to make adjustments of the beam and apparatus to reduce the trigger rate which was initially too high to allow reasonable data taking. It was at this time that after studying the delta ray production in the hydrogen target, we abandoned plans to include a trigger requiring only a tag and a time-of-flight counter hit. By mid-October we were at the stage where we could do a full calibration of the forward detector and subsequently commence data taking.

3.4. Calibration Runs

Prior to taking data we required a full knowledge of the behavior of the detection apparatus under beam conditions. To obtain the required information we set aside approximately one week prior to the data taking to calibrate the apparatus. The bulk of this time was spent on the forward detector.

Since I devote Appendix B to a detailed discussion of the calibration runs, the analysis of the calibration data, and extraction of the relevant quantities, I will only

Reproduced with permission of the copyright owner. Further reproduction prohibited without permission.

briefly discuss the procedures used, highlighting the important results.

We calibrated the apparatus with an electron beam of known energy which was focussed on various spots on the forward detector by a combination of bending the beam with a magnet and moving the forward detector laterally with respect to the beam. Most of the calibration was done with a 30 GeV electron beam because that was the highest energy beam which the magnet could bend to cover the full extent of the forward detector. The tagged photon beam was also used occasionally to establish the differences between electron-initiated and photon-initiated showers. At various times the monitors were turned on and their values calibrated to the electron beam.

Aside from providing the relative gains of the phototubes and an initial calibration of the monitors, the calibration runs provided us with a number of other results, the most important of which are listed below.

For the total absorption counters:

1) The attenuation function was mapped and found to vary by approximately 30% over the entire length of the counter.

2) The energy response is linear from 15 to 185 GeV with a slope of 6.01 ADC counts per GeV.

3) The energy resolution can be parametrized by a Gaussian width $\sigma(E) = 18\% / \sqrt{E}$, where E is measured in GeV.

For the hodoscope:

Reproduced with permission of the copyright owner. Further reproduction prohibited without permission.

1) The attenuation length is about 150 cm.

2) The energy resolution of a single plane is approximately parametrized by 140% / $\sqrt{E}$ (in GeV).

3) The position resolution improves with increasing energy with a value of 2.6 mm (Gaussian standard deviation) at 135 GeV.

3.5 Data Runs

After calibrating the detection apparatus, we began data taking using the foreground/background programs previously described to control the experiment and log the data. Typical running conditions were such that with 3×10^{12} protons per beam spill and a 135 GeV electron beam, we got 200,000 tags, yielding roughly 30 events. Of these triggers, roughly one in two thousand is an elastic scattering event.

A great deal of monitoring information was accumulated during the data taking, much of which was written onto magnetic tape along with the data. The beam quality and intensity were monitored in a number of ways, most of which were provided by Fermilab. The intensity of protons on the primary target was measured by a secondary emission monitor (SEM) which gives a number proportional to the number of protons. We put this number into a CAMAC scaler which was displayed on a television screen and written onto tape along with many other scalers every beam spill. The beam profile was measured at various points along the beam line with seg-

Reproduced with permission of the copyright owner. Further reproduction prohibited without permission.

mented wire ionization chambers (SWIC's), which were also displayed on a television monitor.

We found that our data rate was quite sensitive to the tuning of the last horizontal bending magnet and the tagging magnets. For this reason we monitored the current in these magnets using an analog voltage readout into the digital voltmeter (DVM) system. In addition the temperature at various points in the hydrogen target was monitored using a set of resistors whose resistance is a function of temperature. The voltage drop across these resistors was fed into the DVM system, allowing us to keep track of temperature variations in the target. The DVM system was also used to monitor the high voltages on all the counters and the drift chambers. Periodically the computer read in the DVM values, wrote them onto magtape, and checked them against a set of standard values. If the values were off by more than a specified tolerance, typically .1%, a message was printed on the line printer telling which channel was bad and what its value was so that the person on shift could adjust it. The high voltages were stable to the .1% level, requiring little adjustment throughout the course of the experiment.

At the beginning and end of every spill all the scalers were read in by the computer. A number of counters and trigger rates were monitored this way. One of the most important of these is the number of tags, which serves to normalize the cross sections. Some of the scalers were

Reproduced with permission of the copyright owner. Further reproduction prohibited without permission.

reset every spill, others were allowed to count until the tape was finished. When a new tape was started, all the scalers were reset. Most of the scalers were gated on only during the beam spill, of these about half required the computer to be ready as well. This provides a means to correct for the computer dead-time, since many of the scalers are counted in both categories. Thus a simple subtraction gives the computer dead-time correction.

A number of monitors of the forward and recoil detectors were read in concurrently with the data: the LED's for the time-of-flight, hodoscope, and total absorption counters, the americium monitor for the hodoscope and total absorption counters, and the muon monitor for the total absorption counters. The average value and width of the pulse height distributions for all of the above-mentioned monitors were checked during the course of the data taking and messages printed on the line printer if one was found to be out of tolerance.

Another way of monitoring the counters is to have a counter hit histogram, in which the number of times a counter has a pulse height above some threshold is histogrammed versus the counter number. We used this a great deal to debug problems with the counters. This histogram was printed out along with other summary information at the end of each file on the tape.

Pedestal runs were taken only at the request of the

Reproduced with permission of the copyright owner. Further reproduction prohibited without permission.

person on shift by typing in a command on the teletype. Since the pedestals were found to be quite stable, for the most part only varying by one or two ADC channels over the course of the experiment, we only did pedestal runs every one or two days.

Finally we had another monitor of the tagging system which we read in once or twice per beam spill. This was a trigger consisting of a coincidence of the tag and the beam plug counters. Due to rate problems in the beam plug counters, this did not serve a very useful function and we decided to use a different method of calibrating and monitoring the tagging system which I will discuss a bit later.

In addition to the monitors taken during the course of normal data taking, we had a number of special runs we did from time to time to serve a calibration or monitoring purpose. To get a handle on the kinds of events that occur outside the hydrogen target, or in its walls, we emptied it periodically and took data for four hours or so. The trigger rate was about one-fifth the normal rate, which shows that most of our events come from scattering in the target. We took one data tape using a pulser as a trigger, but with the beam on, to measure accidental rates. We also took one data tape with the forward detector removed from the trigger as a separate type of background event study.

An occasional check on the timing of the TOF counters used a SWIC which was just upstream of the hydrogen target.

Reproduced with permission of the copyright owner. Further reproduction prohibited without permission.

When this SWIC and the lead in front of it were inserted in the beam, a huge number of particles were sprayed into the TOF counters. The forward detector was removed from the trigger so that only the tag was required. This gave a set of events which had the TOF start and TOF counters on and allowed them to be timed to each other relatively easily. More details on the use of these sets of runs can be found in [Grillo 80].

An additional check on the recoil system used cosmic rays. When the beam died for a long time, which was an all too frequent occurrence at Fermilab, we would switch over the event trigger to a coincidence of two or more TOF counters on opposite sides of the beam line. This defined a set of minimum ionizing cosmic ray tracks which were used to calibrate the TOF counters and align the drift chambers. Further discussions of this appear in [Grillo 80 and Palladino 80].

Due to the lack of viability of the T·BP trigger we used another method of calibrating the lead glass in the tagging system. We moved the forward detector such that it intercepted the beam and then used the normal electron-proton and photon-proton triggers with the collimators stopped down so we got about 3000 triggers per spill. The electrons recalibrate the forward detector and then when we turned on the tagging system we used the electron beam energy minus the energy from the forward detector to deter-

Reproduced with permission of the copyright owner. Further reproduction prohibited without permission.

mine the absolute gains of the lead glass blocks. This worked extremely well and has become our primary way of calibrating the lead glass. This is very important since we found that the lead glass blocks closest to the beam line yellowed appreciably in the few-week period between calibrations. A few times during the experiment we cleared these lead glass blocks using an ultraviolet lamp and recalibrated them immediately afterwards.

3.6. Summary of Data Collected

During the course of the major data taking phase of the experiment, which lasted from May to November of 1978 (with many interruptions), we logged data on approximately 400 magnetic tapes. Our running was divided into two major blocks depending on the position of the forward detector. We took the bulk of our data with the forward detector roughly 30 m from the hydrogen target. This was split into two parts. Roughly one-quarter of the data was taken with a 160 GeV electron beam, the rest with a 135 GeV beam. The purpose of this running is to measure elastic scattering, quasi-elastic vector meson production, and low-to-intermediate-transverse-momentum inclusive photon, neutral pion, and eta photoproduction. The ten meter running consists of approximately one-third 80 GeV and two-thirds 135 GeV running. The purpose of these runs is primarily to measure inclusive photoproduction at larger transverse momentum over a wider energy range. During part of this

Reproduced with permission of the copyright owner. Further reproduction prohibited without permission.

running the recoil detector was under repair and not operational. In total we took over four million triggers of photon-proton scattering. Table 3-1 summarizes the various run conditions, including the electron-proton scattering, giving the dates and number of triggers for each set of conditions. [Breakstone 78f] contains a more complete summary of the contents of the data tapes.

Reproduced with permission of the copyright owner. Further reproduction prohibited without permission.

Table 3-1

Summary of Run Conditions

a) Photon-Proton Scattering

Forward Detector Position (m)	Electron Beam Energy (GeV)	Forward Detector Threshold (Db)	Dates (All in 1978)	Triggers
30	135	0	5/21	20871
30	135	6	5/21 to 5/22	109538
			7/12 to 7/27	944485
			8/17 to 8/23	318755
			10/27 to 11/13	1025726
			Subtotal:	2398504
30	160	6	6/19 to 7/12	766951
10	80	0	10/24 to 10/27	360168
10	135	0	10/16	89091
10	135	6	8/24 to 8/25	56193
			10/15 to 10/23	548585
			Subtotal:	604778
			Total:	4219492

Empty target runs (various conditions) 66368

Reproduced with permission of the copyright owner. Further reproduction prohibited without permission.

Table 3-1 (Continued)

b) Electron-Proton Scattering

Forward Detector Position (m)	Electron Beam Energy (GeV)	Forward Detector Threshold (Db)	Dates (All in 1978)	Triggers
30	60	9	5/21	35911
30	80	9	8/16	39281
			11/11	84167
			Subtotal:	123448
30	80	12	10/29 to 10/30	51017
30	135	12	10/29	13015
30	135	15	7/14	15539
			7/18	16444
			Subtotal:	31983
30	160	6	6/22	1684
30	160	17	6/22	15472
			6/25	13171
			7/1	17560
			Subtotal:	41203
			Total:	298261

Reproduced with permission of the copyright owner. Further reproduction prohibited without permission.

Chapter 4

Analysis Procedure

The following chapter deals with the off-line analysis of the data, i.e. how we turn the numbers on tape into yields or scattering cross sections. I will begin by briefly describing the preliminary steps taken to reduce all the data and then go into some detail on the extraction of the inclusive neutral pion and eta distributions. I will only touch briefly on the analysis of other processes such as elastic scattering and quasi-elastic vector meson production which are described in detail in [Grillo 80 and Palladino 80].

4.1. Tape Copying

The first step in analysis of the data was to simply make a copy of the original data tape. This insured against the loss of data in the event that the original data tape was destroyed somehow. Each tape was then translated from NOVA (16-bit word) to CDC (60-bit word) format. See [Breakstone 78e] for more details. All further data processing was done on this set of CDC tapes.

4.2. Monitor Programs

Before we could run analysis programs over the entire

Reproduced with permission of the copyright owner. Further reproduction prohibited without permission.

data set, we had to determine how various calibration quantities varied with time during the experiment. In particular such quantities as the ADC pedestals and the gains of the lead glass blocks in the tagging system and hodoscope and total absorption counters in the forward detector varied on a day-to-day basis, requiring continual updating of the pedestal and gain values for each data tape.

We had a two-pronged effort to monitor these quantities. First we had programs to establish the pedestals or gains on special runs or special trigger types which were taken at various times during the experiment. I discuss these programs in Sections 4.2.1. through 4.2.3. Secondly, we wrote one rather long program to check that the gains and pedestals are reasonable by plotting various distributions using the data itself. In addition this set of routines went over the scalers and looked at various distributions for the drift chambers and time-of-flight counters. I will discuss this program in greater detail in Section 4.2.4.

4.2.1. ADC Pedestals

Since we only took pedestal runs about once a day during the data taking, we have roughly sixty tapes on which we did pedestal runs. We ran a program to calculate the pedestals on these sixty tapes. The only tricky aspect of the program was the algorithm to find the average value and width of the pedestal distribution, throwing away occasional

Reproduced with permission of the copyright owner. Further reproduction prohibited without permission.

garbage triggers and tails of the distribution in the process. Two slightly different algorithms were used depending on the shape of the distribution. For most of the counters the pedestal peak was quite narrow, one or two channels wide (FWHM). For these counters we defined the pedestal value to be the lowest bin with at least the height of the mean height of all contiguous bins that had at least 30% of the height of the peak. This was often the peak bin itself. The width was calculated assuming a Gaussian distribution, rounding off to the nearest integer value. It was usually just one ADC count. For the counters with amplifiers on them (the lead glass blocks and the U/V muon ADC's), the amplifier noise caused the ADC pedestal distribution to be wider, so the previous algorithm did not produce the correct result. The distributions looked Gaussian, so for these ADC's, we defined the pedestal to be the average value of the distribution with the pedestal width defined to be the Gaussian width (σ). The pedestal widths were typically two or three ADC counts for the lead glass ADC's and five to eight counts for the U/V muon ADC's. The pedestals and widths were checked against a set of standard values and, if a calculated value was off by more than one ADC count from the standard value, its histogram was printed, so we could figure out what the pedestal should be by directly looking at the distribution. We found that the pedestals were quite constant with time. The pedestal values and widths thus calculated were then written onto a tape.

Reproduced with permission of the copyright owner. Further reproduction prohibited without permission.

4.2.2. Lead Glass Gains

Approximately a dozen times during the course of the experiment, we moved the forward detector into the beam to recalibrate one of the total absorption counters with an electron beam and then calibrate the lead glass using tagged photons hitting the forward detector. Using the known electron beam energy, we established the gain of the U and V counters hit by the beam. Then, using tagged photons and the pulse height versus energy curve established by the calibration, we calculated the lead glass gains since the energy in the lead glass was simply the beam energy minus the energy in the forward detector. We used only events which hit roughly the centers of the lead glass blocks (as determined by requiring overlapping counters in the tagging hodoscope to be hit) to determine the gains. Even with this precaution, there was still a slight spread of the shower into neighboring lead glass blocks, so we used an iterative procedure to precisely calculate the gain of an individual lead glass block. The gain for the ith counter for the kth iteration is defined by the following formula:

$$g_{i,k} = \frac{E_{beam} - E_{fwd} - g_{i-1,k-1}P_{i,i-1} - g_{i+1,k-1}P_{i,i+1}}{P_{i,i}}$$

where $P_{i,j}$ is the average pulse height in the jth counter when the recoil electron hits the ith counter. E_{beam} and E_{fwd} are the energies of the beam and the tagged photon as measured by the forward detector. We used five iterations

Reproduced with permission of the copyright owner. Further reproduction prohibited without permission.

of this algorithm, but it converged so quickly that the gains did not change significantly after the third pass.

4.2.3. Gains of the Hodoscope and Total Absorption Counters

The program to calculate the gains of the hodoscope and total absorption counters consisted of two separate pieces. The first piece calculated the average value and width of the various monitors for each counter. These values were written on a tape which was read by a second program which calculated the gains based on these values and the standard values derived from the initial calibration.

Since the trigger for each of the monitors consisted basically of a logical "or" of many counters, the ADC for a particular counter was usually at the pedestal value, while only occasionally reading a value corresponding to the monitor for that counter. Thus the program took two passes of the data for each monitor. In the first pass, it calculated the pedestal and found the approximate location of the peak due to the monitor. In the second pass, it histogrammed the monitor (with pedestal subtracted) on a finer scale and calculated the average value and width. In doing so it only included events within a range defined by the set of contiguous bins with at least 20% of the height of the maximum bin. It further required there to be a minimum number of events in this range. This minimum varied from 20 to 100 events depending on the type of monitor. Finally, these

Reproduced with permission of the copyright owner. Further reproduction prohibited without permission.

values were written onto magnetic tape and checked against a set of standard values. If the average or width disagreed with the standard by more than a certain tolerance (5% for the U/V americium and LED and the hodoscope LED, 20% for the U/V muon and hodoscope americium monitors), the histograms were printed out for all the monitors on that particular counter.

This program was run on approximately 100 tapes for which there was sufficient monitor data. Figures 4-1 and 4-2 show the results for typical total absorption and hodoscope counters. We have plotted the average value for the various monitors as a function of tape number. The ratio of the various monitors is also plotted. The tracking of the LED and americium monitors for the total absorption counters is quite good as is evidenced by the nearly constant ratio shown in Figure 4-1d. For the hodoscope the tracking between the two monitors is not as good.

Based on the results of the average value versus tape number plots, we found that the hodoscope gains were constant to about the 10% level, so when calculating the gains as a function of time, we simply used the gain calculated when the counters were calibrated. For the total absorption counters, there were substantial gain shifts for several of the counters, so we calculated the gain on a tape-by-tape basis, smoothing over any rapid fluctuations which occurred. Primarily we used the americium monitor to calculate the

Reproduced with permission of the copyright owner. Further reproduction prohibited without permission.

Figure 4-1

Monitors for the Total Absorption Counters

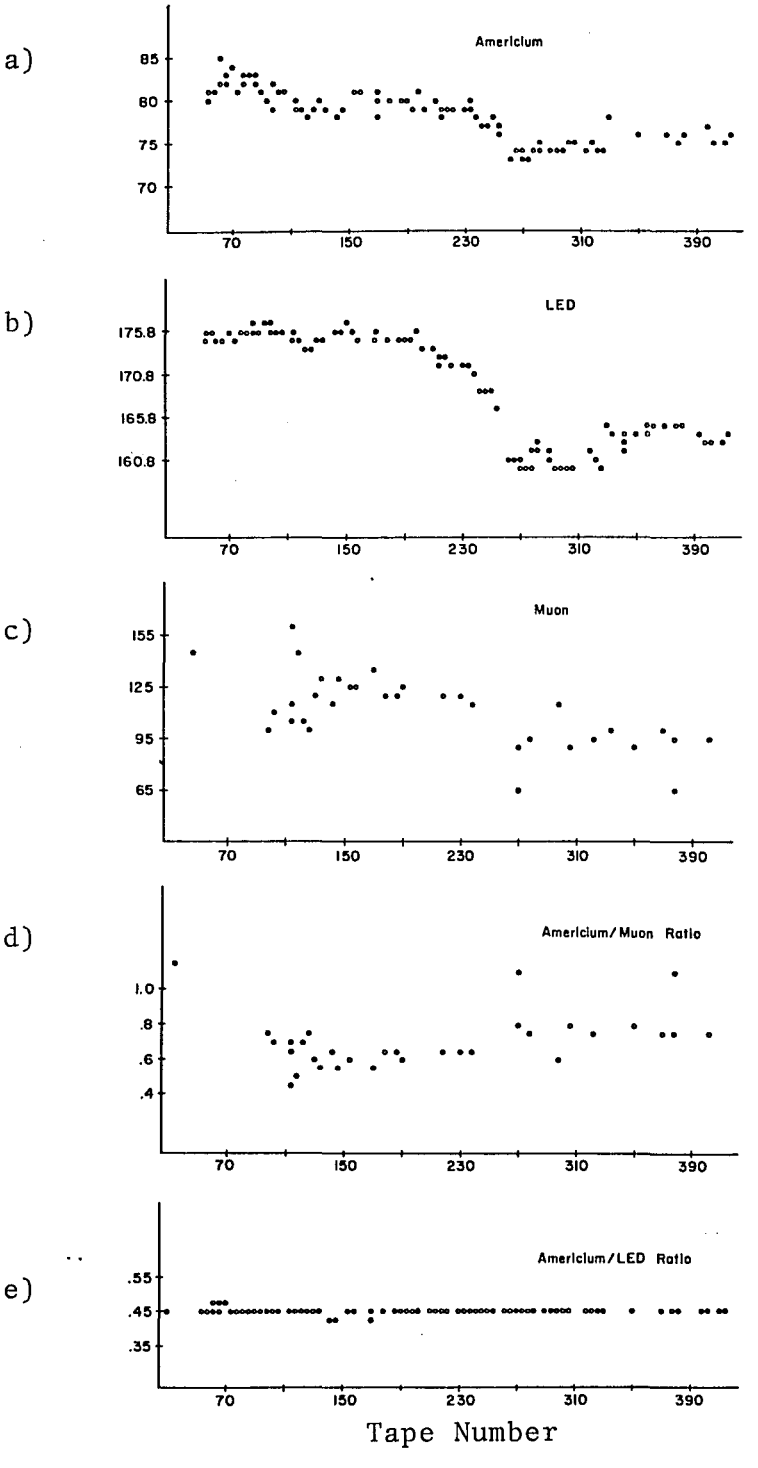

Reproduced with permission of the copyright owner. Further reproduction prohibited without permission.

Figure 4-2

Monitors for the Hodoscope

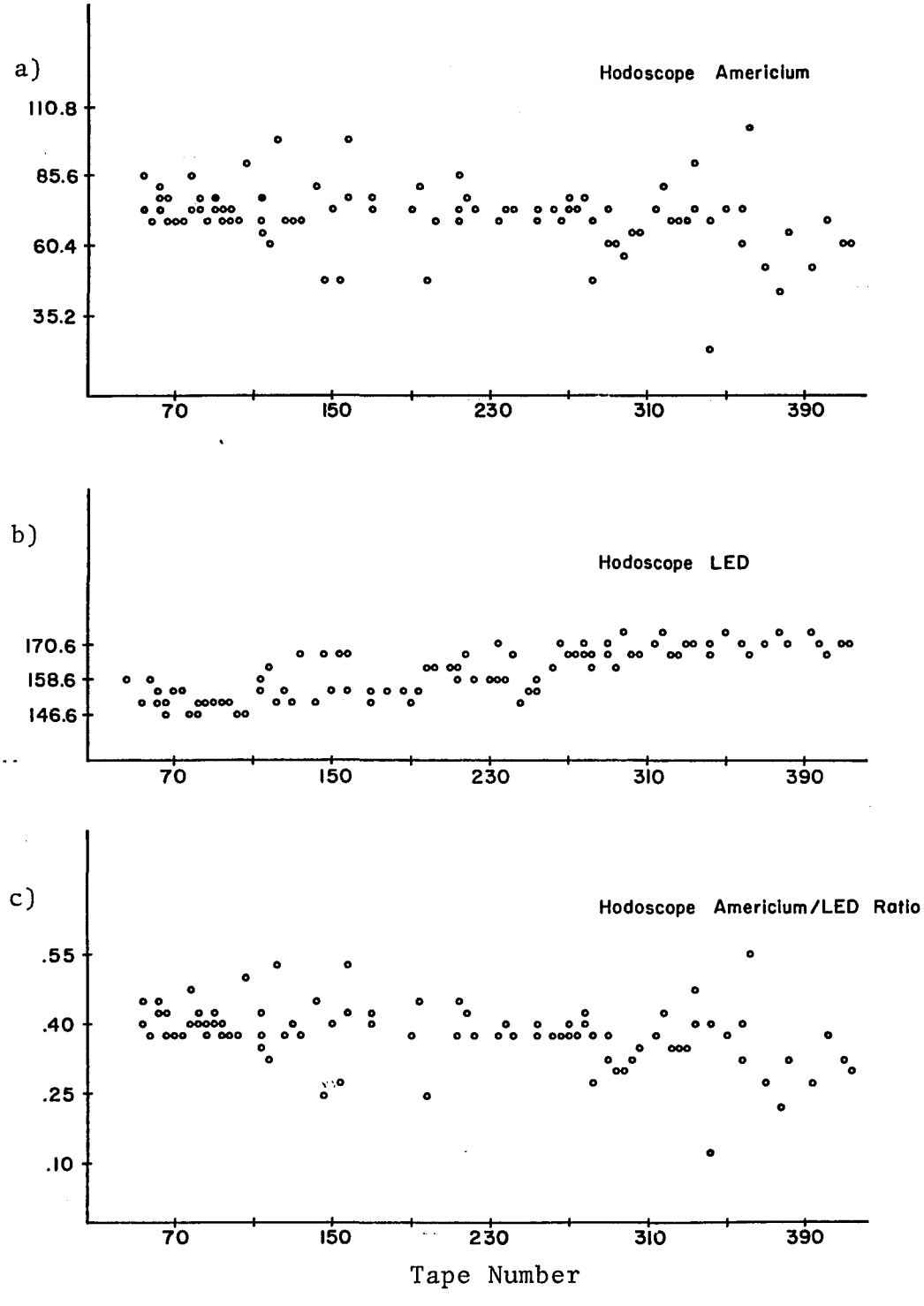

Reproduced with permission of the copyright owner. Further reproduction prohibited without permission.

gain; however, there were cases where the data were lacking or where there were inexplicable fluctuations, in which case we used the LED for the gain calculation. The gain is defined such that the product of the gain and the average value of the monitor is a constant, i.e., $g \cdot \langle PH \rangle = \text{const}$. Note that this is the inverse of what is traditionally called the gain since its value goes down when the pulse height goes up. Figure 4-3 shows this gain as a function of tape number for a typical total absorption counter.

4.2.4. The Grand Monitor Program

There are a number of quantities to calculate or histogram for each data tape before further processing the data. For example, the scalers must be checked, the lead glass gains calculated, the gains of the hodoscope and total absorption counters checked, etc. To do this we wrote a large program which consisted of three separate programs run sequentially.

The first of these read the scaler information from the beam start and stop event types, summing the scaler values for the entire tape. At the end of the file, it printed out the accumulated sums, wrote them onto a tape along with a number indicating from which tape and file they are accumulated, and calculated and printed out various ratios of the scalers.

The second program used the T·BP events to see if the

Reproduced with permission of the copyright owner. Further reproduction prohibited without permission.

Figure 4-3

Total Absorption Counter Gain

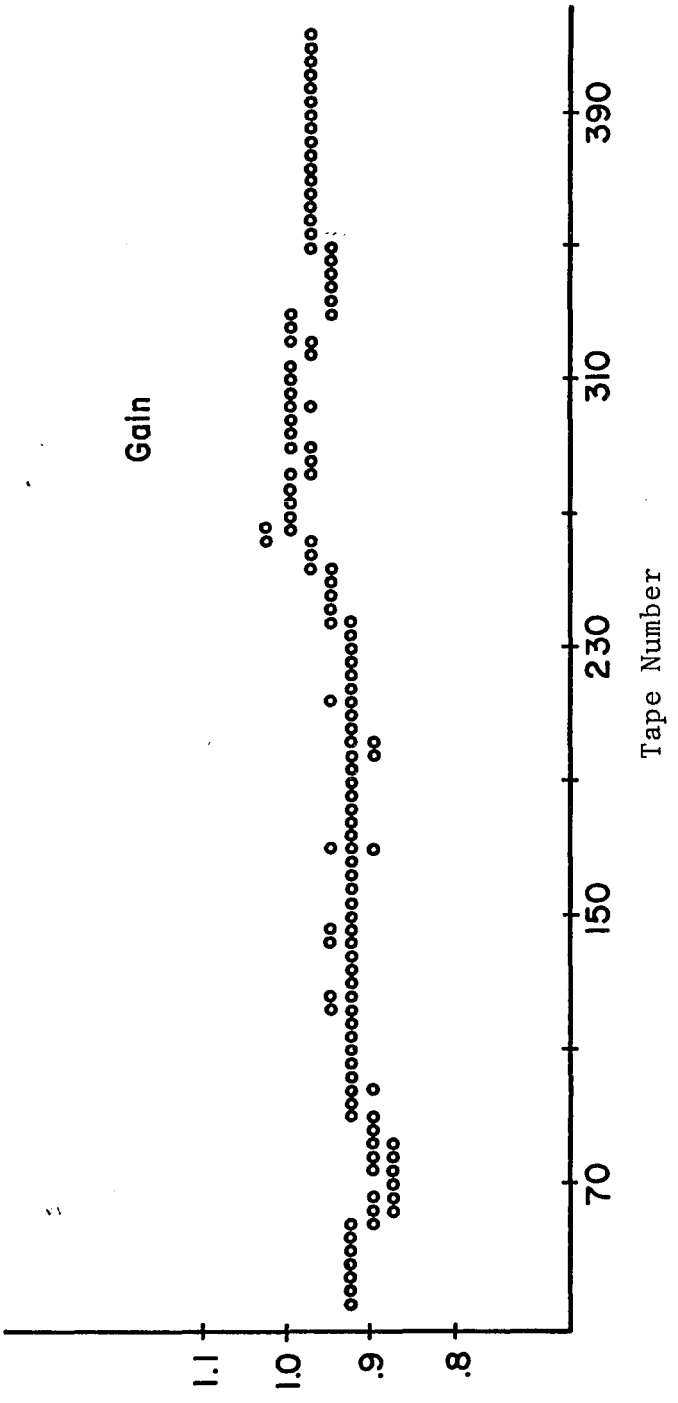

Reproduced with permission of the copyright owner. Further reproduction prohibited without permission.

beam plug counters were working properly by histogramming the pulse height spectra in the two beam plug counters using various cuts on the lead glass and hodoscope counters in the tagging system.

The third program of this series was run on the real events and has several sections to it. It:

1) Histogrammed all the ADC's to calculate the pedestals and check them against the values calculated by the pedestal program described in Section 4.2.1. The same algorithms were used here as well. The pedestal values and widths were then printed out and written onto tape.

2) Histogrammed the U + V pulse height before and after gain corrections for each of the sixteen U/V combinations.

3) Histogrammed the uncorrected sums of pulse heights in the U bank of total absorption counters and in both banks as a check on the proper functioning of trigger thresholds.

4) Made a hit frequency plot of the hodoscope counters so we could spot bad counters. Also we plotted the average pulse height in each hodoscope counter before and after gain corrections as a check on the hodoscope gains.

5) Histogrammed the pulse height in each beam plug counter.

6) Calculated the lead glass gains using the previously discussed algorithm (Section 4.2.2.). It also calculated pedestal correction factors due to rate effects in some of the lead glass counters. The gains and pedestal correction factors were printed out and also written onto a tape.

7) Made a consistency check of the TOF ADC's, TDC's, and latches for each tube, made a hit frequency plot, and checked other quantities related to the time spectra. [Grillo 80] describes these checks in greater detail.

8) Histogrammed several distributions for the drift chambers, among which were a wire hit frequency plot, a TDC time spectrum for each module, the number of hits per quadrant, and the average TDC value for each wire. More details on these distributions as well as a full

Reproduced with permission of the copyright owner. Further reproduction prohibited without permission.

description of other checks that are done on the drift chambers may be found in [Palladino 80].

A large number of monitoring quantities were calculated and printed out along with about a hundred histograms. Much of the summary information was written onto a tape as well to aid in relating these quantities from different data tapes and to be used by other programs for further processing. [Breakstone 80] contains more details about this set of programs.

4.3. Forward Detector Analysis Routines

In order to extract neutral pions and other radiatively decaying mesons from the data, it is necessary to have a set of routines which isolate showers in the forward detector, giving their energy, position, and width. This is complicated because showers are quite wide in the detector due to the air gaps between the U counters, hodoscope, and V counters. They may overlap or have missing energy in the beam hole or at the edge of the array. In addition hadrons in the event complicate the reconstruction problem. We have written a set of routines to try to solve these problems by separating them into a number of steps.

The first few steps are to simply input various flags and counters for the tape reading routines, cuts and tolerances used by the analysis routines, read in the pedestals and gains from tape, and set limits for any histograms or

Reproduced with permission of the copyright owner. Further reproduction prohibited without permission.

scatter plots that one wishes to make. At this point one is ready to read in events from tape and process them one at a time. This begins with a set of routines which check the tagging system information to see if we have a good tag. For example, it checks that the tagging hodoscope and lead glass information are compatible, it checks that the energy deposited in the lead glass is sensible, makes sure that there are no extraneous hits in the tagging hodoscope or lead glass, etc. About 20% of the events are rejected due to bad tags. This is followed by a routine to zero all the variables in common blocks that the analysis routines use so that data from a previous event cannot find its way into the current event. Next we call a routine to subtract pedestals from the ADC's for the hodoscope and total absorption counters and multiply them by the gains.

This is followed by a routine to find hits in the total absorption counters. A hit is defined by a U + V pulse height sum of 5 ADC counts or more of which at least 5 counts must be in the U bank. This corresponds to showers of approximately 1 GeV. At this point no shower position information is known, so no attenuation corrections are made. After all hits are found, the hits are reordered by their pulse heights.

Next comes a pair of routines to find clusters in the x and y planes of the hodoscope. A cluster is defined as a set of at least three contiguous strips, where each has a

Reproduced with permission of the copyright owner. Further reproduction prohibited without permission.

pulse height above a cut of 4 ADC counts, corresponding to about 0.5 GeV of energy deposition.

At this point the basic information from the total absorption counters and hodoscope is known and the only problem that remains is to match them together. This is an extremely difficult problem. The program attempts to solve this problem by sorting the events according to the number of hits in each plane of the hodoscope and then branching to the appropriate ambiguity handling routine to try to do the matching. If the number of x and y clusters agree, the routines match the hodoscope clusters in each plane, using the combination that yields the best energy match consistent with the total absorption counter hits. If the number of clusters in each plane does not agree, the program associates one cluster in one plane with two in the other plane using energy match criteria and compatibility with the total absorption counter hits. It then tries to split the one cluster into two by searching for a minimum between two maxima in the pulse height distribution, requiring at least two strips to be above the minimum on each side to reduce misidentification of the minimum due to lateral fluctuations in the shower. If this procedure fails, one can still calculate the mean position of each shower in the plane in which they overlap if one assumes that the energy and shower widths are similar in both planes. The formula (derived in Appendix D) is

Reproduced with permission of the copyright owner. Further reproduction prohibited without permission.

$$x_{1,2} = \bar{x} \pm \left(\frac{E_{2,1}}{E_{1,2}}\sigma_x^2 - \frac{E_{2,1}}{E}\sigma_{1,2}^2 - \frac{E_{2,1}^2}{EE_{1,2}}\sigma_{2,1}^2\right)^{1/2}$$

where $E = E_1 + E_2$ and the σ's are rms widths. E, x, and σ_x are measured quantities while E_1, E_2, σ_1, and σ_2 are taken from the other plane. The assumption that the shower widths and energies are similar in the two planes leads to errors in the calculation of x_1 and x_2, but in testing the algorithm using both Monte Carlo events and real showers artificially displaced in one plane, we found that the error in the position of individual showers is less than 1 cm. In each of the ambiguity routines, as soon as the hodoscope clusters are successfully associated with the total absorption counters, attenuation corrections are applied. The shower energy is determined by including pulse height from all U and V counters with which the hodoscope cluster overlaps. Energy information from the hodoscope is used to apportion energy to showers which overlap in the total absorption counters.

At the conclusion of the analysis package the program provides a certain number of reconstructed showers, giving their energies, positions, widths, and a few other quantities relating to the probability of being a single photon or a neutral pion, which are discussed below. Approximately 4% of the events cannot be properly reconstructed by this set of routines. The Monte Carlo efficiency calculation

Reproduced with permission of the copyright owner. Further reproduction prohibited without permission.

corrects for this loss.

One of the most difficult problems confronting these analysis routines is how to resolve showers which are too close together to form two separate clusters in the hodoscope. This occurs quite frequently in decays of neutral pions, where, for example, the minimum opening angle is only 2.7 mr for a 100 GeV π^0, yielding a separation of only 8 cm in the hodoscope when it is 30 m from the target. Because of large fluctuations in the pulse heights of individual hodoscope strips, these showers can look like showers due to single photons and visa versa. We have devised a rather simple test which we use to decide whether the shower is due to a single photon or two photons. It has the additional benefit that it gives us the mass of the two-photon system if the shower is due to two photons. We define the following quantity:

$$m^2_{\gamma\gamma} = \frac{E^2}{z^2} (\sigma^2_x + \sigma^2_y - \sigma^2_{xo} - \sigma^2_{yo})$$

where E is the energy of the shower as measured in the total absorption counters, z is the distance from the target to the hodoscope, σ_x and σ_y are the measured widths of the shower in the x and y hodoscope planes, and σ_{xo} and σ_{yo} are the parametrized widths of single showers. Thus if the shower is due to one photon, ideally $\sigma_x = \sigma_{xo}$ and $\sigma_y = \sigma_{yo}$ and we get $m^2_{\gamma\gamma} = 0$. In practice there is a spread of values about zero which gets worse as the energy gets higher

Reproduced with permission of the copyright owner. Further reproduction prohibited without permission.

due to the E^2 term in the expression.

Complications are caused by the facts that the parametrized widths of single showers, σ_{xo} and σ_{yo}, are not equal and increase with increasing shower energy. Showers in the y plane are wider than those in the x plane because the y plane is in front and absorbs many of the low-energy, wide-angle particles in the shower. Using the methods described in the next section, we have established the following parametrization:

$$\sigma^2_{xo} = \begin{cases} 5.0 + .333\ E & \text{for } E < 20 \text{ GeV} \\ 11.0 + .10\ (E-20) & \text{for } E > 20 \text{ GeV} \end{cases}$$

$$\sigma^2_{yo} = \begin{cases} 7.0 + .50\ E & \text{for } E < 20 \text{ GeV} \\ 17.0 & \text{for } 20 < E < 50 \text{ GeV} \\ 17.0 + .18\ (E-50) & \text{for } E > 50 \text{ GeV} \end{cases}$$

For showers with their centers in the narrow hodoscope strips, the squares of the widths are approximately 20% smaller. We include this effect in the parametrization as well.

Because of the energy dependence of the widths, one must be careful what value of the energy to use for the parametrized width to get the correct $m^2_{\gamma\gamma}$. If there really is only one photon, the full energy should be used; however, if there are two photons, the true widths of each shower are smaller, thus one must use a lower value for the energy. For symmetric decays this is E/2, whereas for extremely asymmetric ones, it approaches E. On the average the value

Reproduced with permission of the copyright owner. Further reproduction prohibited without permission.

is 2/3 E. This point is discussed more fully in Appendix D, where I go through the full derivation of all these formulas.

Using the above-mentioned parametrization, we calculate the quantity $m^2_{\gamma\gamma}$ for each shower which gets through the ambiguity handling routines. A histogram of this quantity for a subset of the data is shown in Figure 4-4. One can see peaks due to single photons and neutral pions. The pion peak is quite broad due to the combined effects of the energy resolution, uncertainties in the gains, and variations in the widths of showers. The photon peak is displaced slightly from zero because of the 2/3 factor in the energy used for the parametrized widths.

Using the widths and the calculated mass squared, we form two chi-squared tests for single photon and pion hypotheses. For the single photon hypothesis we define

$$\chi^2_\gamma = \frac{[(\sigma^2_x-\sigma^2_{xo})+(\sigma^2_y-\sigma^2_{yo})]^2}{\delta^2_1} + \frac{[(\sigma^2_x-\sigma^2_{xo})-(\sigma^2_y-\sigma^2_{yo})]^2}{\delta^2_2}$$

where $\delta^2_1 = 67$ and $\delta^2_2 = 45$ as found from single photon calibration data. We use the sum and difference of the differences in width squared in each hodoscope plane because we want to separate effects due to overall width from those due to skewness of the pulse height distributions. For this test we use the full energy to calculate the parameterized widths σ_{xo} and σ_{yo}. For the neutral pion hypothesis we define

Reproduced with permission of the copyright owner. Further reproduction prohibited without permission.

Figure 4-4

Mass Squared for Individual Showers
with E > 35 GeV and $(x^2+y^2)^{1/2}$ > 25 cm

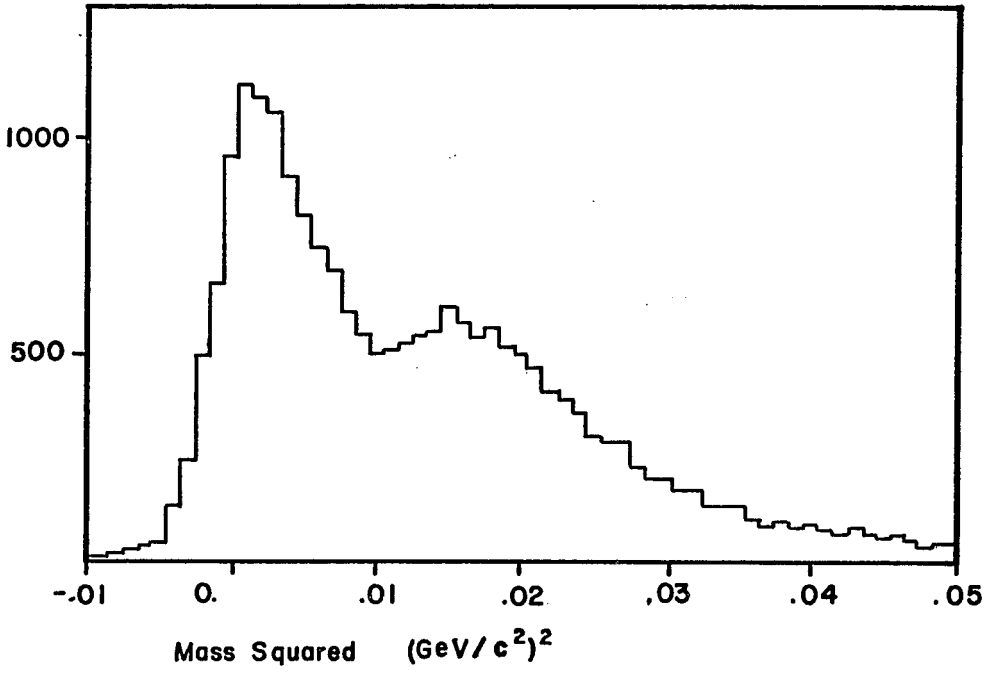

Reproduced with permission of the copyright owner. Further reproduction prohibited without permission.

$$\chi^2_\pi \quad \{ \frac{m^2_{\gamma\gamma} - m^2_\pi}{\sigma^2_\pi} \}^2$$

The value of σ^2_π is determined by taking two single photons showers from the calibration data, artificially displacing them in the hodoscope by the right distance to form the invariant mass of a π^o, and looking at the $m^2_{\gamma\gamma}$ distribution. It increases with energy according to the following parametrization:

$$\sigma^2_\pi = \begin{array}{ll} .0020 + .000028\ E & \text{for } E < 50 \text{ GeV} \\ .0034 + .000064\ (E-50) & \text{for } 50 < E < 64 \text{ GeV} \\ .0043 + .000243\ (E-64) & \text{for } 64 < E < 88 \text{ GeV} \\ .01 & \text{for } E > 88 \text{ GeV} \end{array}$$

For this test we use two-thirds of the energy in determining σ_{xo} and σ_{yo}. These tests give us the relative likelihood that the unresolved shower is a single photon or is actually two overlapping showers from a neutral pion.

4.4. Corrections to Shower Energy, Position, and Width

As we proceeded with the analysis of the data, we found that the mass peaks due to the π^o and ω were not centered at their proper values. We eventually traced the problem to non-linearities in the forward detector response and energy normalization difficulties. The calibration procedures were not sensitive to some of these effects since the exact value of the beam energy was not known with sufficient precision.

Reproduced with permission of the copyright owner. Further reproduction prohibited without permission.

These effects are particularly important for low energy showers (below 30 GeV) for which there is practically no calibration data.

Fortunately, the data provide a means to correct for these deficiencies. We isolated a sample of quasi-elastic omegas by methods described in [Palladino 80]. We then ran this sample through the forward detector analysis package and found that most of the time it reconstructs two showers, one for the photon and one for the neutral pion. This is expected since for pions above about 30 GeV, the two photons from its decay are not resolved by the detector. Using the known masses of the ω and π^0, the measured opening angle, and the tagged photon energy ($E_\omega \simeq E_{tag}$ for quasi-elastic production), we calculate the energies of the γ and π^0 using

$$E_1 = \frac{E_\omega}{2} \left[1 + \left(1 - \frac{4(m_\omega^2 - m_\pi^2)}{E_\omega^2 \theta^2}\right)^{1/2} \right]$$

and $$E_2 = E_\omega - E_1$$

and compare them to the reconstructed energies from the total absorption counters. There are two effects to correct. The overall gains of most of the U and V counters needed adjustment. The multiplicative gain correction factors are given in Table 4-1. The gains of the outermost counters cannot be corrected due to lack of statistics. Secondly, there is an energy non-linearity in the total absorption counters which we correct by simply adding 3 GeV to the energy of each reconstructed shower. When we correct

Reproduced with permission of the copyright owner. Further reproduction prohibited without permission.

Table 4-1

U and V Gain Correction Factors

Counter Number	Correction Factor U	V
1	-	-
2	1.1	-
3	1.1	1.0
4	.95	.95
5	1.05	.9
6	1.0	1.0
7	1.2	-
8	-	-
9	-	-
10	1.2	-
11	1.05	1.2
12	1.2	.9
13	1.08	.88
14	1.1	.9
15	1.05	-
16	-	-

Reproduced with permission of the copyright owner. Further reproduction prohibited without permission.

Figure 4-5

Reconstructed versus Calculated Energy of
Showers from Omega Decays

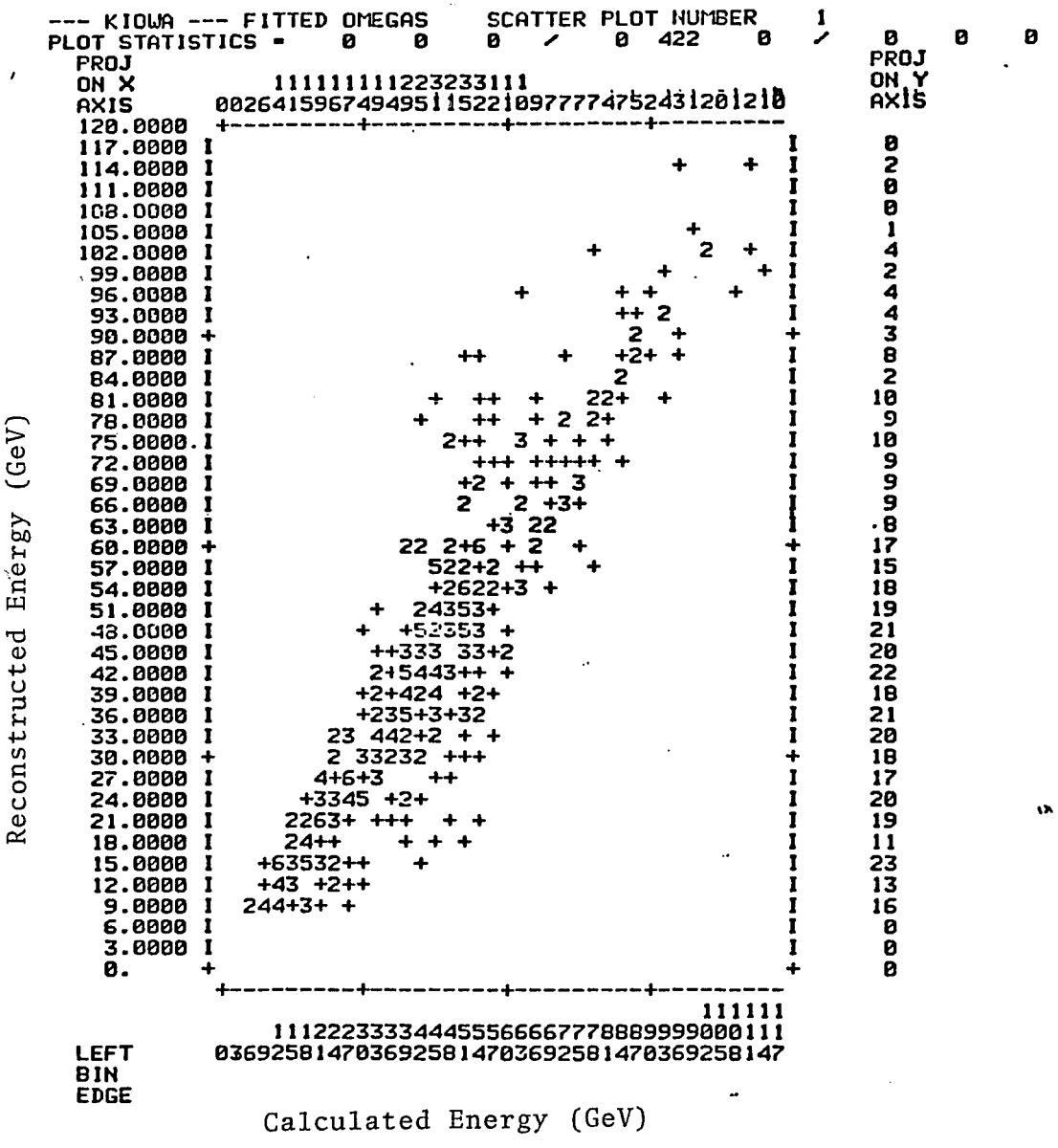

Reproduced with permission of the copyright owner. Further reproduction prohibited without permission.

for these effects and redo the analysis, we find that the calculated and reconstructed energies of showers from omegas agree quite well as shown in Figure 4-5.

The hodoscope has a known problem with linearity at low energies, which we first noticed at the time of the calibration. Using omega events, single photon calibrations, and isolated showers from the data, we have plotted the X and Y plane energies versus those measured by the total absorption counters (with their corrections) for the full energy range from 3 to 150 GeV. An eyball fit to these yields the following multi-linear expressions for the hodoscope energies:

$$E_x = \begin{cases} .2\ PH & \text{for } 0 < PH < 150 \\ 30. + .12\ (PH-150) & \text{for } 150 < PH < 400 \\ 60. + .075\ (PH-400) & \text{for } 400 < PH < 666 \\ 80. + .09\ (PH-666) & \text{for } PH > 666 \end{cases}$$

$$E_y = \begin{cases} .171\ PH & \text{for } 0 < PH < 175 \\ 30. + .12\ (PH-175) & \text{for } 175 < PH < 342 \\ 50. + .086\ (PH-342) & \text{for } 342 < PH < 575 \\ 70. + .1\ (PH-575) & \text{for } 575 < PH < 675 \\ 80. + .12\ (PH-675) & \text{for } PH > 675 \end{cases}$$

where PH is the pulse height summed over all the strips in the hodoscope cluster.

In addition the parametrization for the widths of showers in the hodoscope is extended reliably to lower energy using the previously-mentioned data sets to yield the parametrization given in the previous section.

Finally, there is a correction of a different nature for showers which overlap the beam hole. Sometimes the cal-

Reproduced with permission of the copyright owner. Further reproduction prohibited without permission.

culated position ends up to be inside the beam hole, which is obviously impossible. Thus, for showers with centers within three strips (9 cm) of the beam hole, we recalculate the position in each hodoscope plane as follows. First we search for the strip with the maximum pulse height. If that strip is adjacent to the beam hole, we set the position of the shower to the center of that strip and set the error in the position to 9 mm. If the strip is one strip away from the beam hole, we use it and one neighbor on each side to determine the position and error. If neither of these cases occurs, then we leave the position as is. This corrects the position of most of the showers which would otherwise be incorrectly positioned inside the beam hole.

4.5. Inclusive Filters

After fully debugging the analysis routines, we wrote filter programs to reduce the data sample to a manageable size for subsequent analysis. The results discussed in the next chapter are based on a sample of about three-fourths of the 135 GeV, 30 m running. We ran the filter in two stages. The first stage merely requires a good tag and the forward detector analysis package to reconstruct from one to four showers. This eliminates about 25% of the events, mostly due to bad tags. The events are then written out onto another tape in a densely packed format. This reduces the data sample from 1.54 million triggers on 91 data tapes to 1.15 million triggers on 10 summary tapes.

Reproduced with permission of the copyright owner. Further reproduction prohibited without permission.

The second stage of filtering consists of isolating samples of events which contain neutral pions and eta mesons. Separate filters were run for each. The eta filter requires at least two reconstructed showers. Pairs of showers are made for which each must pass a hadron cut (U/total pulse height greater than .1) and a requirement that it be due to a single photon, rather than a coalesced pion (chisquared for the single photon hypothesis less than 20). The mass squared of the pair is calculated and the event kept if it is between .1 and 1.0 $(GeV/c^2)^2$ for at least one pair in the event. This eliminates 87% of the events, further reducing the sample from 1.15 million to 151 thousand events.

The pion filter takes into account that most pions with energies above the trigger threshold will be coalesced into a single reconstructed shower. For this reason it puts no limit on the number of reconstructed showers, but has a more complicated algorithm for rejecting events. An event is kept if it has a single shower with energy greater than 38 GeV, passes the previously mentioned hadron cut, has a mass squared based on the shower width algorithm between .002 and .1 $(GeV/c^2)^2$, and its center is within a fiducial area from 8.5 to 60 cm in each hodoscope plane. Also, for events in which two or more showers are reconstructed, pairs are formed with the same cuts as for the eta filter for each shower, with an additional fiducial cut. In addition the energy of the pair must exceed 38 GeV and its mass squared

Reproduced with permission of the copyright owner. Further reproduction prohibited without permission.

be in the range .002 to .1 $(GeV/c^2)^2$. This eliminates 68% of the filtered events, reducing the sample to 367 thousand events.

4.6. Mass Fits, Efficiency, and Normalization

The final steps to calculate the inclusive cross sections are to histogram the mass and mass squared of the forward object, fit the histograms with a given mass hypothesis to get the number of events in the peak above background, correct this number for the detection efficiency, and normalize it using the number of tagged photons incident on the target and the target length and density. This is done separately for each bin of tagging energy, and transverse momentum and Feynman x of the forward object. Mathematically this can be expressed as follows:

$$\frac{d\sigma(E_\gamma)}{dx_F dp_t^2} = \frac{\frac{dN}{dx_F dp_t^2}(E_\gamma, x_F, p_t)}{\varepsilon(E_\gamma, x_F, p_t)\cdot BR\cdot N_\gamma(E_\gamma, x_F)\cdot\rho\cdot\frac{N_p}{\mu}\cdot N_o\cdot L}$$

where N is the number of events (signal above background),

ε is the detection efficiency,

BR is the branching ratio for the two photon decay,

(.38 for the η, .9885 for the π^o)

N_γ is the number of tagged photons,

ρ is the target density (.0708 g/cm^3),

N_p is the number of protons per molecule (2),

μ is the molecular weight (2 g/mole),

N_o is Avagadro's number (6.022×10^{23} molecules/mole),

Reproduced with permission of the copyright owner. Further reproduction prohibited without permission.

and

L is the length of the target (75 cm).

$\rho N_p N_o L/\mu = 3.198 \times 10^{24}$ protons/cm^2

The number of events is determined by fitting each mass or mass squared histogram with a Gaussian peak on a polynomial background:

$$f(m) = A\,(1 + a_1P_1(m) + a_2P_2(m) + a_3P_3(m)) + \frac{N}{\sigma\sqrt{2\pi}}\, e^{-(m-m_o)^2/2\sigma^2}$$

We use Legendre polynomials to fit the background. An example of such a fit for the entire inclusive η sample is shown in Figure 4-6.

The normalization is obtained by counting the number of tagged photons which can contribute to a given bin. Using the T·BP events and the scaler information, we have determined the number of tagged photons for each data tape as a function of their energy (in 5 GeV bins). The computer dead time correction is made at this time. For details on how this was done see [Palladino 80]. Summing over the data tapes in the inclusive sample, one obtains the total number of tagged photons as a function of energy (dN_γ/dE_γ). The total number of photons summed over all energy bins is 1.001×10^{10}. To calculate the number of photons which can contribute to a bin defined by E_γ^{min}, E_γ^{max} and x_F^{min}, x_F^{max}, one uses

Reproduced with permission of the copyright owner. Further reproduction prohibited without permission.

Figure 4-6

Two Shower Mass Histogram with Fit

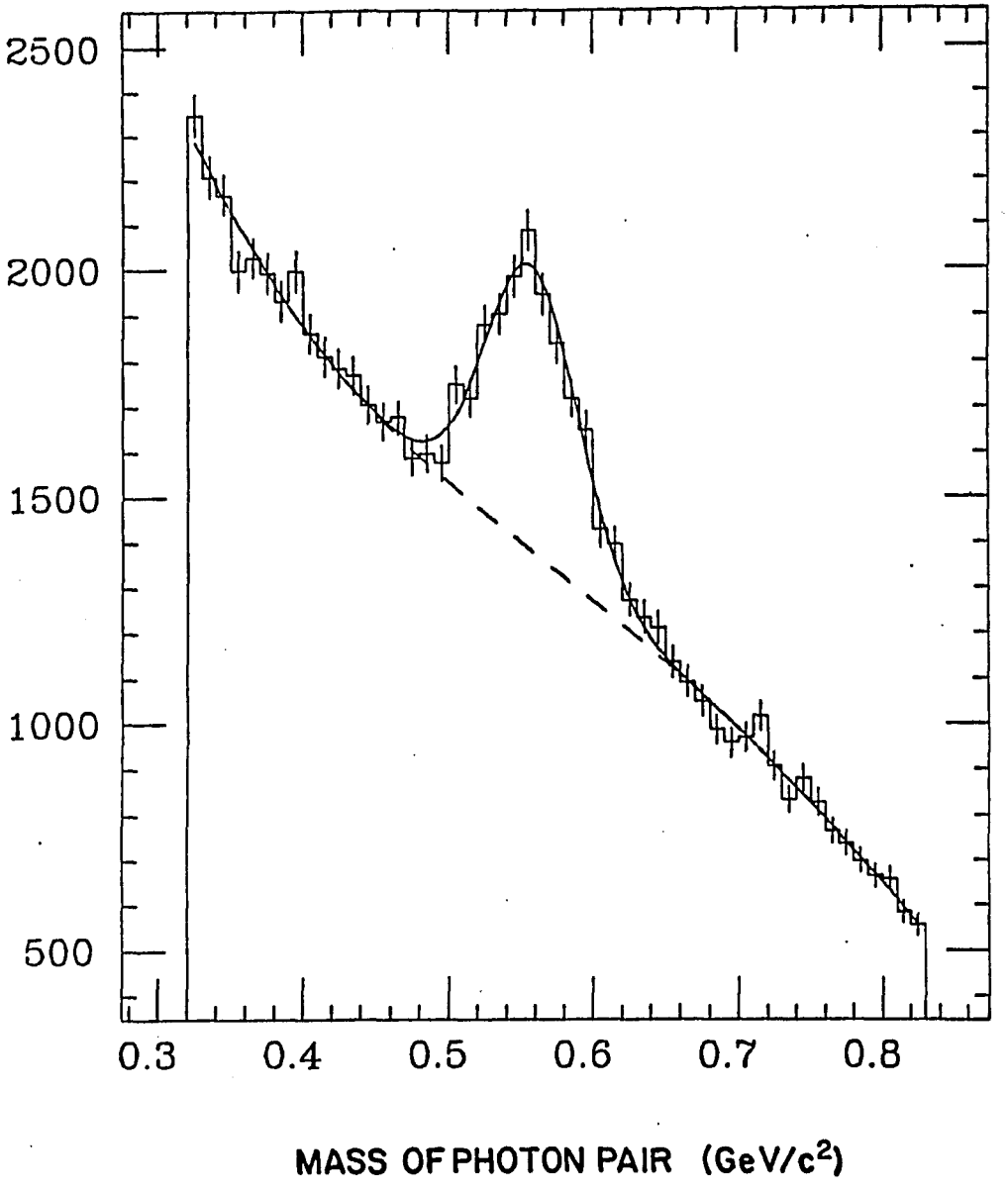

Reproduced with permission of the copyright owner. Further reproduction prohibited without permission.

$$N_\gamma(E_\gamma,x_F)= \int_{E_\gamma^{min}}^{E_\gamma^{max}} \frac{dN_\gamma}{dE_\gamma}\, \theta(E-E_{cut})\,[\theta(\frac{E}{E_\gamma} -x_F^{min})-\theta(\frac{E}{E_\gamma} -x_F^{max})]\; dE_\gamma$$

where E is the energy of the π^o or η, and E_{cut} is an energy cut of 38 GeV (below 38 GeV, trigger bias corrections would be large). θ is the standard mathematical function that is zero for negative values of its argument and one for positive values. Since we use a statistical method for extracting the signal from the background, we need to make the assumption that on the average $E = \overline{x_F}\; E_\gamma$, where $\overline{x_F}$ is the average value of Feynman x for η's or π^o's contributing to the particlular mass histogram in question. Doing this we get

$$N_\gamma(E_\gamma,x_F) = \int_{E_\gamma^{min}}^{E_\gamma^{max}} \frac{dN_\gamma}{dE_\gamma}\; \theta(E_\gamma\overline{x}_F - E_{cut})\; dE_\gamma$$

which gives us the number of tagged photons that contribute to a given bin of E_γ, x_F, and p_t.

To obtain the detection efficiency for a given bin, we wrote a Monte Carlo program which generates events using a quark cascade model [Seiden 76]. Multiple bremsstrahlung in the tagging radiator is included for the generation of the incoming photon. We keep only events with a π^o or η above 38 GeV and have all η's decay via the two photon mode. This reduces the running time of the job considerably. The generation routine writes a separate tape, each containing

Reproduced with permission of the copyright owner. Further reproduction prohibited without permission.

10,000 Monte Carlo events, for the π^0 and η inclusives.

Another program reads these tapes and tracks particles to the forward detector. It simulates the behavior of electromagnetic showers in the detector using various functions for the lateral and longitudinal development (including fluctuations) for each detection element (X, Y, U, and V planes) based on the data. The effect of hadrons is simulated by giving a hadron which hits the detector a 50% chance of converting into a photon having one-third of the hadron's energy. The parametrized shower information is used to generate pulse heights in the various counters, including gain, attenuation, and pedestal corrections. This information is then written out onto another tape in a format which is very similar to that of real data tapes.

These Monte Carlo tapes are then analyzed by the same routines which do the data. The number of reconstructed η's or π^0's is counted and compared to the number generated as a function of tagged photon energy, Feynman x, and transverse momentum. This ratio gives the efficiency for each bin. The efficiencies are discussed further in the next chapter.

Reproduced with permission of the copyright owner. Further reproduction prohibited without permission.

Chapter 5

Results

5.1. Results

Using the analysis procedures described in the previous chapter, we obtained the results given in this chapter. Some additional cuts were placed on the data, including mass cuts and fiducial cuts, to decrease the backgrounds in the mass and mass squared plots before fitting them. These cuts are summarized in Table 5-1. For the η inclusive cross sections, we fit the mass histograms over the interval from .325 to .825 GeV/c^2 in .01 GeV/c^2 bins. The peaks are best fit with a mass of .558 GeV/c^2 and a width of .032 GeV/c^2. The mass is systematically high by 2%, indicating a slight overall error in the energy calibration. The width (6%) is consistent with our energy resolution, including effects due to gain variations with time from counter to counter. For the π^0, the fits are done in mass squared over the interval from .0065 to .0415 $(\mathrm{GeV}/c^2)^2$ in .001 $(\mathrm{GeV}/c^2)^2$ bins. They yield a mass squared of .020 $(\mathrm{GeV}/c^2)^2$ with a width of .0050 $(\mathrm{GeV}/c^2)^2$. The peaks for the π^0 are non-Gaussian, yielding poorer fits in general than for the η. The π^0 mass squared is systematically high by 10% and its width large (20%) due primarily to fluctuations coming from the shower width algorithm used to determine the mass squared and the parametrization of these widths. There is also a larger systematic

Reproduced with permission of the copyright owner. Further reproduction prohibited without permission.

Table 5-1

Cuts on the η and π^0 Data Samples

η

Tagged photon energy: $50 < E_\gamma < 130$ GeV
Require 2 or more reconstructed showers in event
For each shower: $\chi^2_\gamma < 20$ (single photon cut)
$U/(U + V) < .1$ (hadron cut)
inside box from 8.5 to 60 cm in each plane (fiducial cut)
$E > 8$ GeV (energy cut)
For two shower object: $E_\eta > 38$ GeV (energy cut)
$.1 < m^2 < 1.0$ $(GeV/c^2)^2$ (mass cut)

π^0

Tagged photon energy: $50 < E_\gamma < 130$ GeV

For each shower: $U/(U + V) < .1$ (hadron cut)
inside box from 8.5 to 60 cm in each plane (fiducial cut)
$E_\pi > 38$ GeV (energy cut)
$.003 < m^2_{\gamma\gamma} < .05$ $(GeV/c^2)^2$ (mass cut)

or

Require 2 or more reconstructed showers in event and
For each shower: $\chi^2_\gamma < 20$ (single photon cut)
$U/(U + V) < .1$ (hadron cut)
inside box from 8.5 to 60 cm in each plane (fiducial cut)
$E > 8$ GeV (energy cut)
For two shower object: $E_\pi > 38$ GeV (energy cut)
$.003 < m^2 < .05$ $(GeV/c^2)^2$ (mass cut)

Reproduced with permission of the copyright owner. Further reproduction prohibited without permission.

uncertainty for the π^0 than for the η because the average values and widths of the mass squared peaks for the π^0 vary as a function of energy, but this was not taken into account in the fits.

The detection efficiencies for η's and π^0's, based on the Monte Carlo program, are given in Tables 5-2 through 5-5. The average efficiency for detecting both η's and π^0's is about 20%. The size of the detector provides the major cutoff in efficiency for transverse momenta above 1.2 GeV/c. The beam hole fiducial cut makes the efficiency for detecting pions low for p_t below .3 GeV/c, whereas for η's, the opening angle of the decay photons reduces the importance of this effect. The detection efficiency is quite different for π^0's and η's as a function of their energy due to the different opening angles of photons from π^0 and η decays. For the π^0, the detection efficiency is lower for high energy π^0's because the showers coalesce to such a degree that it becomes difficult to separate them from single photons. For η's the opposite is the case, since for low energy η's, one or both of the decay photons will miss the detector.

We have plotted the π^0 and η inclusive cross sections as a function of transverse momentum, integrated over Feynman x from .35 to 1.0, for three tagged photon energy bins and integrated over tagged photon energy from 50 to 130 GeV, for three Feynman x bins (Figures 5-1, 5-2a, b, c, 5-4, and

Reproduced with permission of the copyright owner. Further reproduction prohibited without permission.

5-5a, b, c). Also we have plotted the Feynman x distributions, integrated over transverse momentum, for three energy bins (Figures 5-3 and 5-6). For the η, the integral is over all transverse momenta, whereas for the π^0, a lower limit of .3 GeV/c is used. These distributions are given in tabular form in Tables 5-2 to 5-5, where we have included the relative flux (the ratio of the number of photons which can contribute to the bin to the total number of photons), the Monte Carlo efficiency, and the number of events derived from the fit.

The errors given in the tables and shown in the figures correspond primarily to random errors from the fits, but also include estimates of some of the systematic errors. The major source of systematic errors in the fits comes from over- or under-estimating the background under the mass or mass squared peaks. For the π^0, the mass squared peaks shift and widen with increasing energy due to effects from the shower width algorithm for coalesced pions. This major source of systematic errors is not included in the cross section. We are undertaking a further study of these effects so that we can reduce the systematic errors from this source.

We have calculated the η/π^0 ratio averaged over all tagged photon energies. The values of this ratio as a function of p_t and x_F are given in Table 5-6 and Figures 5-7 and 5-8.

Reproduced with permission of the copyright owner. Further reproduction prohibited without permission.

Table 5-2

Transverse Momentum Distributions for Etas

p_t Limits GeV/c	$\langle p_t^2 \rangle$ $(GeV/c)^2$	Relative Flux	Monte Carlo Efficiency	Number from Fit	$\frac{d\sigma}{dp_t^2}$ $\mu b/(GeV/c)^2$
	$.35 < x_F < .9$		$50 < E_\gamma < 70$ GeV		
.2- .3	.062	.243	.068±.027	31± 9	3.12± 1.54
.3- .5	.160	.237	.048±.020	76± 15	3.44± 1.58
.5- .7	.351	.239	.044±.015	43± 15	1.39± .49
.7-1.0	.597	.265	.024±.016	12± 6	.29± .25
	$.35 < x_F < .9$		$70 < E_\gamma < 90$ GeV		
0- .1	.005	.265	.273±.057	37± 19	4.22± 2.33
.1- .2	.024	.265	.237±.041	100± 21	4.38± 1.19
.2- .3	.063	.265	.289±.043	81± 35	1.75± .80
.3- .5	.157	.265	.223±.026	386± 40	3.37± .53
.5- .7	.350	.265	.185±.022	281± 30	1.97± .32
.7-1.0	.643	.265	.145±.021	171± 20	.71± .14
	$.35 < x_F < .9$		$90 < E_\gamma < 130$ GeV		
0- .1	.005	.422	.267±.100	97± 33	7.34± 3.72
.1- .2	.024	.422	.288±.035	221± 51	4.99± 1.30
.2- .3	.064	.422	.299±.028	358± 41	4.67± .69
.3- .5	.160	.422	.313±.016	672± 64	2.61± .28
.5- .7	.351	.422	.300±.077	741±100	2.01± .31
.7-1.0	.661	.422	.286±.045	530± 50	.71± .13
1.0-1.4	1.263	.422	.168±.058	103± 15	.12± .05

Reproduced with permission of the copyright owner. Further reproduction prohibited without permission.

Table 5-2 (continued)

p_t Limits GeV/c	$\langle p_t^2 \rangle$ $(GeV/c)^2$	Relative Flux	Monte Carlo Efficiency	Number from Fit	$\frac{d\sigma}{dp_t^2}$ $\mu b/(GeV/c)^2$
	$.35 < x_F < .45$		$50 < E_\gamma < 130$ GeV		
0- .1	.005	.368	.182 ± .159	58 ± 21	7.13 ± 6.75
.1- .2	.024	.364	.118 ± .094	99 ± 31	6.37 ± 5.48
.2- .3	.064	.365	.188 ± .060	142 ± 29	3.41 ± 1.29
.3- .5	.161	.365	.132 ± .036	205 ± 47	2.19 ± .78
.5- .7	.348	.369	.140 ± .042	156 ± 41	1.03 ± .42
.7-1.0	.631	.376	.038 ± .030	73 ± 30	.82 ± .74
	$.45 < x_F < .6$		$50 < E_\gamma < 130$ GeV		
.1- .2	.024	.642	.181 ± .030	114 ± 40	2.68 ± 1.05
.2- .3	.064	.639	.301 ± .045	160 ± 43	1.37 ± .42
.3- .5	.160	.638	.210 ± .035	517 ± 64	1.99 ± .25
.5- .7	.351	.640	.196 ± .028	468 ± 50	1.27 ± .22
.7-1.0	.662	.646	.068 ± .027	246 ± 35	.91 ± .38
	$.6 < x_F < .9$		$50 < E_\gamma < 130$ GeV		
0- .1	.004	.957	.211 ± .060	69 ± 30	2.81 ± 1.47
.1- .2	.024	.940	.266 ± .025	96 ± 30	1.05 ± .34
.2- .3	.063	.937	.235 ± .023	162 ± 30	1.22 ± .25
.3- .5	.159	.930	.233 ± .015	427 ± 50	1.01 ± .14
.5- .7	.355	.928	.242 ± .016	435 ± 50	.67 ± .08
.7-1.0	.675	.928	.223 ± .023	401 ± 30	.31 ± .04
1.0-1.4	1.279	.935	.196 ± .058	83 ± 30	.039 ± .018

Reproduced with permission of the copyright owner. Further reproduction prohibited without permission.

Table 5-3

Feynman x Distributions for Etas

x_F Limits	$\langle x_F \rangle$	Relative Flux	Monte Carlo Efficiency	Number from Fit	$\frac{d\sigma}{dx_F}$ μb
all p_t			$50 < E_\gamma < 70$ GeV		
.55-.65	.607	.133	.040±.018	60± 20	9.27± 5.14
.65-.75	.695	.242	.074±.019	71± 16	3.23± 1.09
.75-.90	.817	.287	.029±.006	55± 15	3.70± 1.29
all p_t			$70 < E_\gamma < 90$ GeV		
.45-.55	.505	.194	.114±.021	205± 40	7.62± 2.03
.55-.65	.595	.265	.254±.032	386± 40	4.73± .77
.65-.75	.694	.265	.366±.094	273± 33	2.32± .35
.75-.90	.815	.265	.244±.028	199± 30	1.69± .32
all p_t			$90 < E_\gamma < 130$ GeV		
.35-.45	.401	.422	.161±.023	723±100	8.75± 1.73
.45-.55	.495	.422	.255±.042	777±100	5.96± 1.26
.55-.65	.595	.422	.383±.038	652± 60	3.31± .45
.65-.75	.694	.422	.434±.042	363± 42	1.64± .25
.75-.90	.813	.422	.313±.045	164± 50	.69± .22

Reproduced with permission of the copyright owner. Further reproduction prohibited without permission.

Table 5-4

Transverse Momentum Distributions for Neutral Pions

p_t Limits GeV/c	$\langle p_t^2 \rangle$ $(GeV/c)^2$	Relative Flux	Monte Carlo Efficiency	Number from Fit	$\frac{d\sigma}{dp_t^2}$ $\mu b/(GeV/c)^2$
	$.35 < x_F < .9$		$50 < E_\gamma < 70$ GeV		
.5- .7	.367	.233	.071±.031	266±100	2.12± 1.23
.7-1.0	.681	.242	.072±.027	328± 74	1.16± .52
	$.35 < x_F < .9$		$70 < E_\gamma < 90$ GeV		
.1- .2	.028	.265	.083±.055	300±200	14.4 ±13.6
.2- .3	.063	.265	.134±.055	246± 54	4.39± 2.06
.3- .5	.160	.265	.305±.055	1869±286	4.57± 1.08
.5- .7	.357	.265	.306±.071	2048±200	3.33± .84
.7-1.0	.680	.265	.229±.055	2206±300	2.26± .63
1.0-1.4	1.249	.265	.123±.098	394± 60	.41± .33
	$.35 < x_F < .9$		$90 < E_\gamma < 130$ GeV		
.2- .3	.064	.422	.167±.044	1347±355	12.1 ± 4.53
.3- .5	.160	.422	.237±.026	5585±538	11.0 ± 1.61
.5- .7	.355	.422	.190±.048	5107±372	8.37± 2.18
.7-1.0	.685	.422	.195±.047	4296±399	3.24± .84
1.0-1.4	1.278	.422	.072±.048	985±200	1.08± .75

Reproduced with permission of the copyright owner. Further reproduction prohibited without permission.

Table 5-4 (continued)

P_t Limits GeV/c	$\langle p_t^2 \rangle$ $(GeV/c)^2$	Relative Flux	Monte Carlo Efficiency	Number from Fit	$\frac{d\sigma}{dp_t^2}$ $\mu b/(GeV/c)^2$
	$.35 < x_F < .45$		$50 < E_\gamma < 130$ GeV		
.2- .3	.064	.366	.177±.113	934±254	9.13± 6.32
.3- .5	.161	.367	.191±.069	3007±400	8.49± 3.27
.5- .7	.354	.368	.265±.071	3125±900	4.22± 1.76
.7-1.0	.673	.371	.137±.039	2248±225	2.74± 1.47
	$.45 < x_F < .6$		$50 < E_\gamma < 130$ GeV		
.1- .2	.029	.631	.091±.057	610±200	11.2 ± 7.84
.2- .3	.064	.637	.129±.072	822±271	6.32± 4.08
.3- .5	.160	.639	.373±.050	3592±300	2.98± .48
.5- .7	.356	.640	.315±.057	3423±339	2.24± .46
.7-1.0	.687	.643	.349±.058	3129±300	.87± .17
	$.6 < x_F < .9$		$50 < E_\gamma < 130$ GeV		
.3- .5	.161	.928	.189±.063	1189±293	1.33± .56
.5- .7	.355	.926	.162±.049	1037±200	.92± .32
.7-1.0	.693	.924	.201±.067	1455±300	.49± .20
1.0-1.4	1.314	.931	.185±.095	407±200	.084 ± .056

Reproduced with permission of the copyright owner. Further reproduction prohibited without permission.

Table 5-5

Feynman x Distributions for Neutral Pions

x_F Limits	$\langle x_F \rangle$	Relative Flux	Monte Carlo Efficiency	Number from Fit	$\frac{d\sigma}{dx_F}$ μb
	$p_t > .3$ GeV/c		$50 < E_\gamma < 70$ GeV		
.55-.65	.607	.133	.263±.099	302± 83	2.73± 1.27
.65-.75	.696	.243	.103±.039	400±150	5.07± 2.29
.75-.90	.817	.287	.034±.017	200± 50	4.31± 2.40
	$p_t > .3$ GeV/c		$70 < E_\gamma < 90$ GeV		
.45-.55	.506	.196	.245±.082	2678±300	17.6 ± 6.2
.55-.65	.596	.265	.263±.088	2400±400	10.9 ± 4.07
.65-.75	.693	.265	.367±.075	800±188	2.60± .81
.75-.90	.807	.265	.116±.075	99± 60	.69± .55
	$p_t > .3$ GeV/c		$90 < E_\gamma < 130$ GeV		
.35-.45	.402	.367	.216±.058	8612±800	34.4 ± 9.8
.45-.55	.495	.422	.415±.077	5678±500	10.3 ± 2.10
.55-.65	.594	.422	.274±.059	2000±600	5.48± 2.03
.65-.75	.693	.422	.270±.090	3000±2000	5.55± 2.49

Reproduced with permission of the copyright owner. Further reproduction prohibited without permission.

Table 5-6

η/π^0 Ratio

Averaged Over Tagged Photon Energy in the Range

$50 < E_\gamma < 130$ GeV

a) as a function of transverse momentum for $.35 < x_F < .9$

p_t Limits GeV/c	$\langle p_t^2 \rangle$ $(GeV/c)^2$	η/π^0 Ratio
.3- .5	.16	.61 ± .13
.5- .7	.35	.39 ± .09
.7-1.0	.63	.26 ± .10
1.0-1.4	1.22	.09 ± .07

b) as a function of Feynman x for $.3 < p_t < 1.4$ GeV/c

x_F Limits	$\langle x_F \rangle$	η/π^0 Ratio
.35- .45	.4	.25 ± .09
.45- .55	.5	.49 ± .14
.55- .65	.6	.91 ± .35
.65- .75	.7	.54 ± .17
.75- .9	.81	.41 ± .25

Reproduced with permission of the copyright owner. Further reproduction prohibited without permission.

Figure 5-1

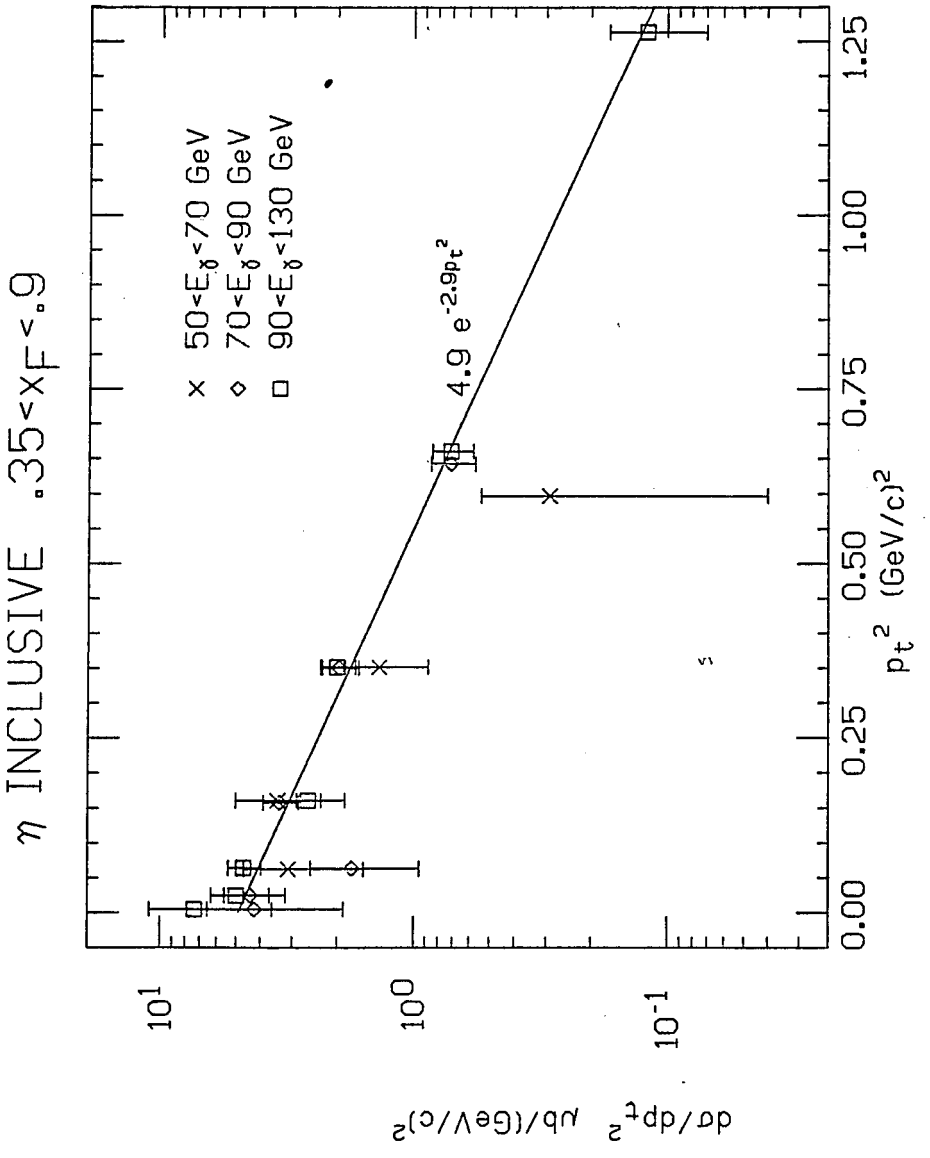

Reproduced with permission of the copyright owner. Further reproduction prohibited without permission.

Figure 5-2a

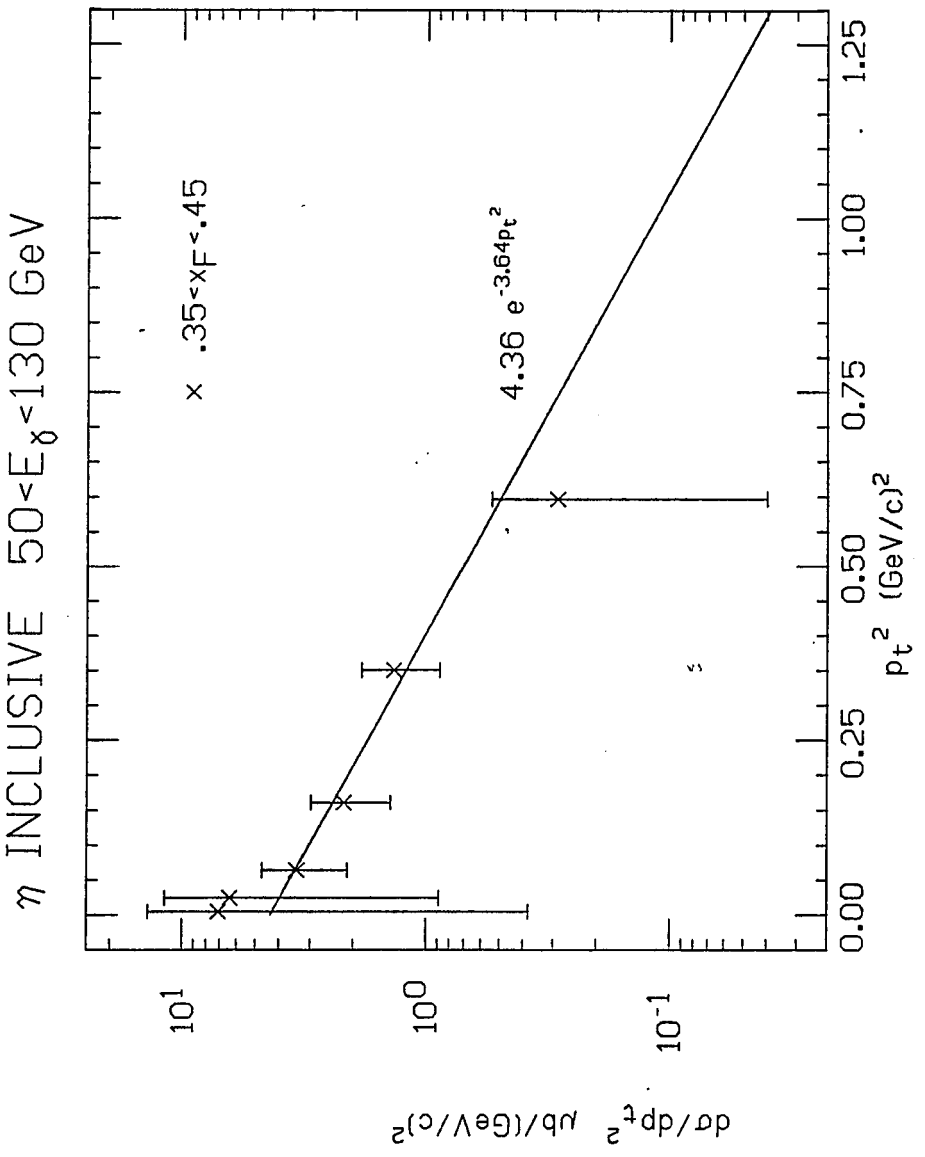

Reproduced with permission of the copyright owner. Further reproduction prohibited without permission.

Figure 5-2b

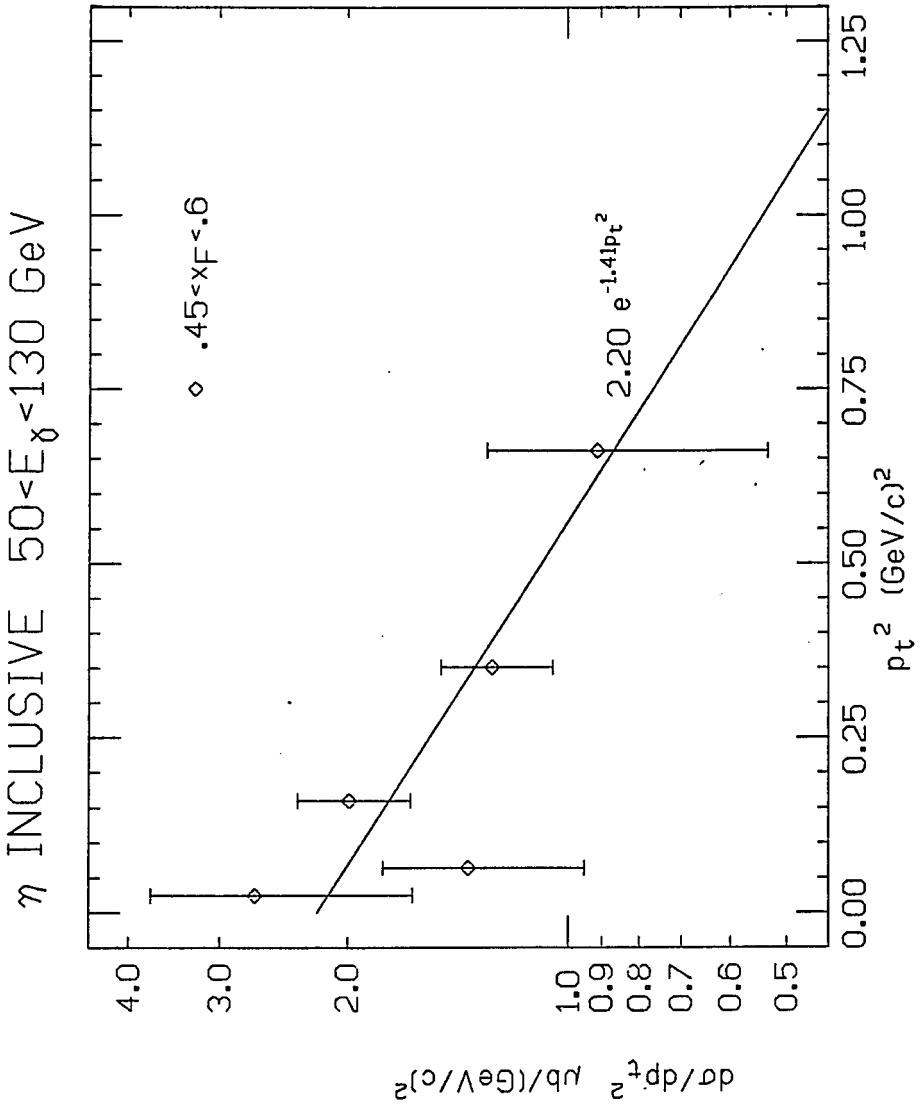

Reproduced with permission of the copyright owner. Further reproduction prohibited without permission.

Reproduced with permission of the copyright owner. Further reproduction prohibited without permission.

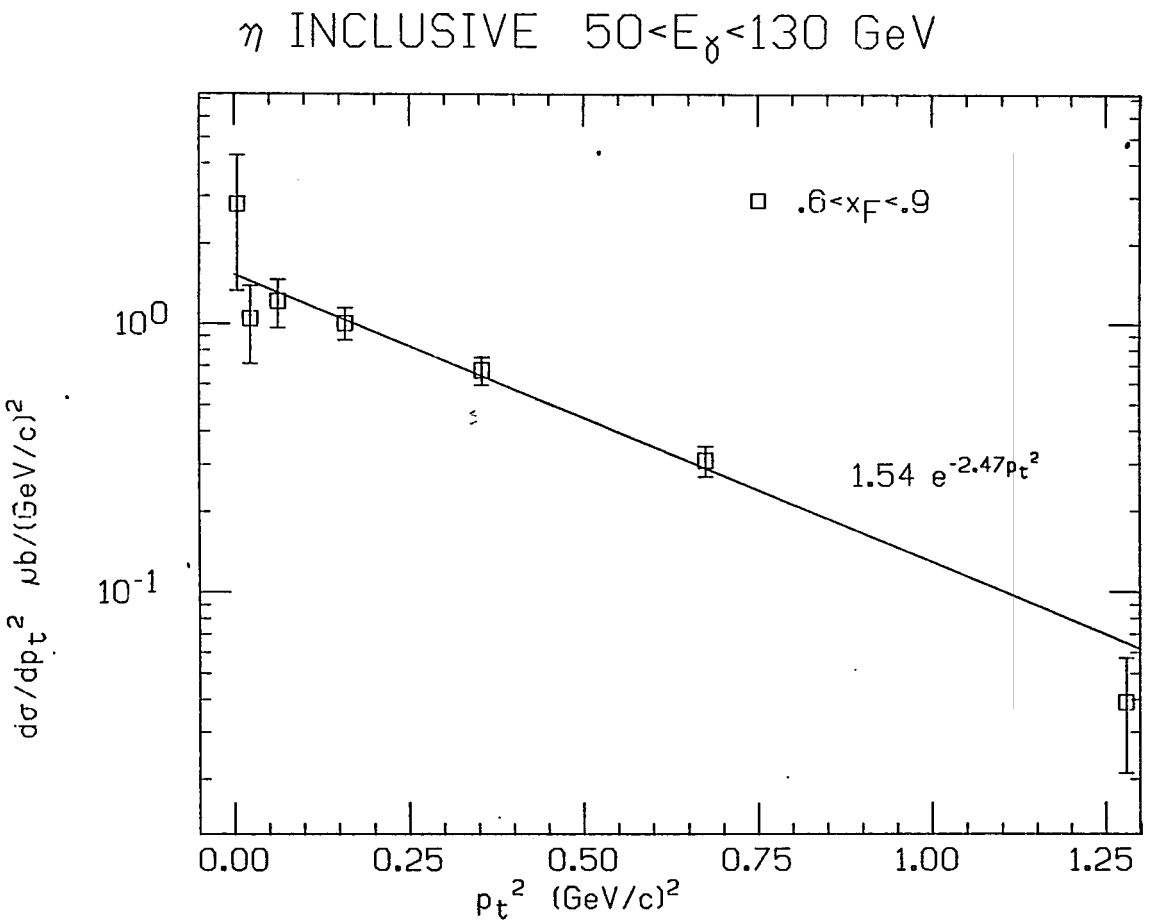

Figure 5-2c

Figure 5-3

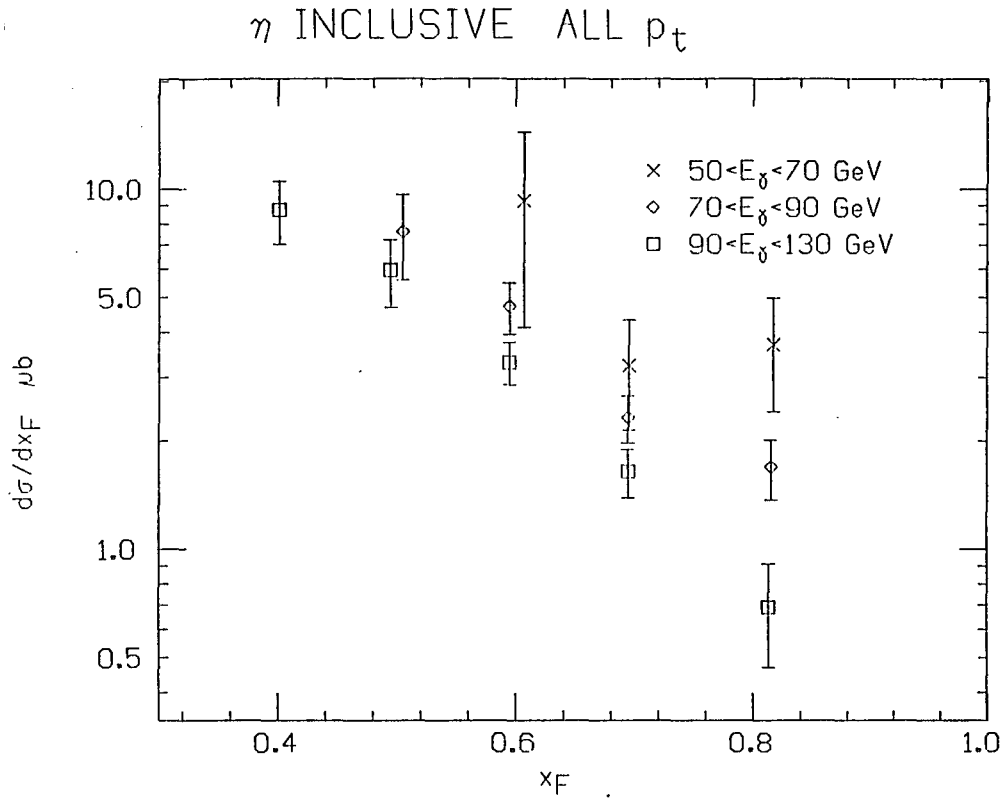

Reproduced with permission of the copyright owner. Further reproduction prohibited without permission.

Reproduced with permission of the copyright owner. Further reproduction prohibited without permission.

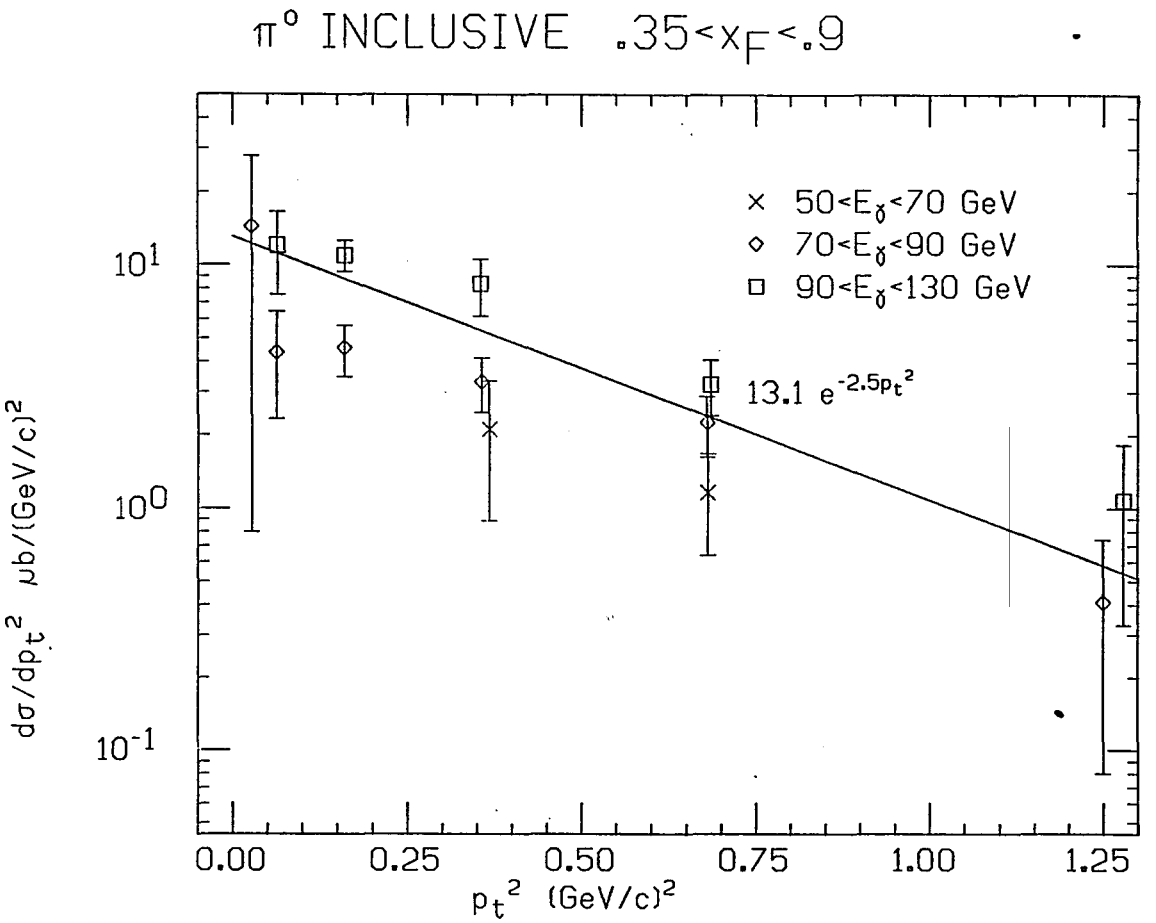

Figure 5-4

Figure 5-5a

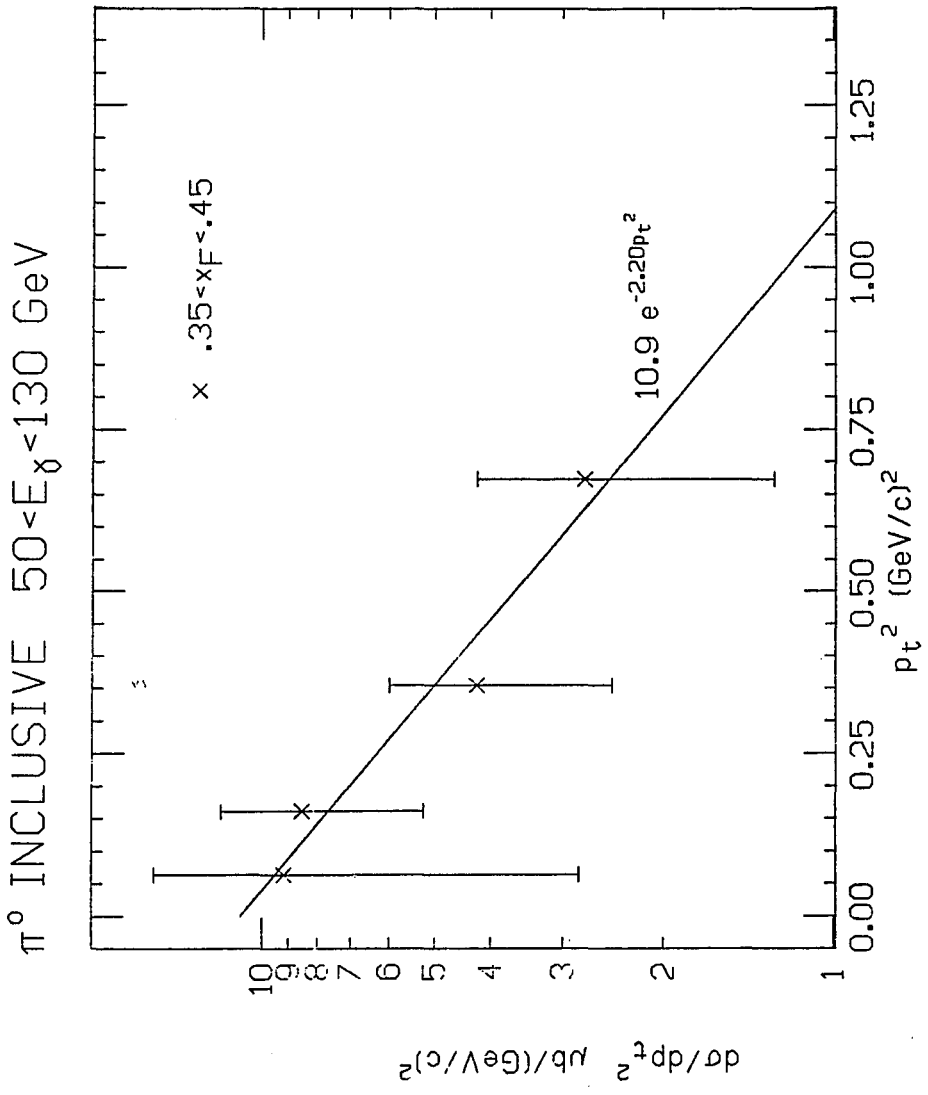

Reproduced with permission of the copyright owner. Further reproduction prohibited without permission.

Figure 5-5b

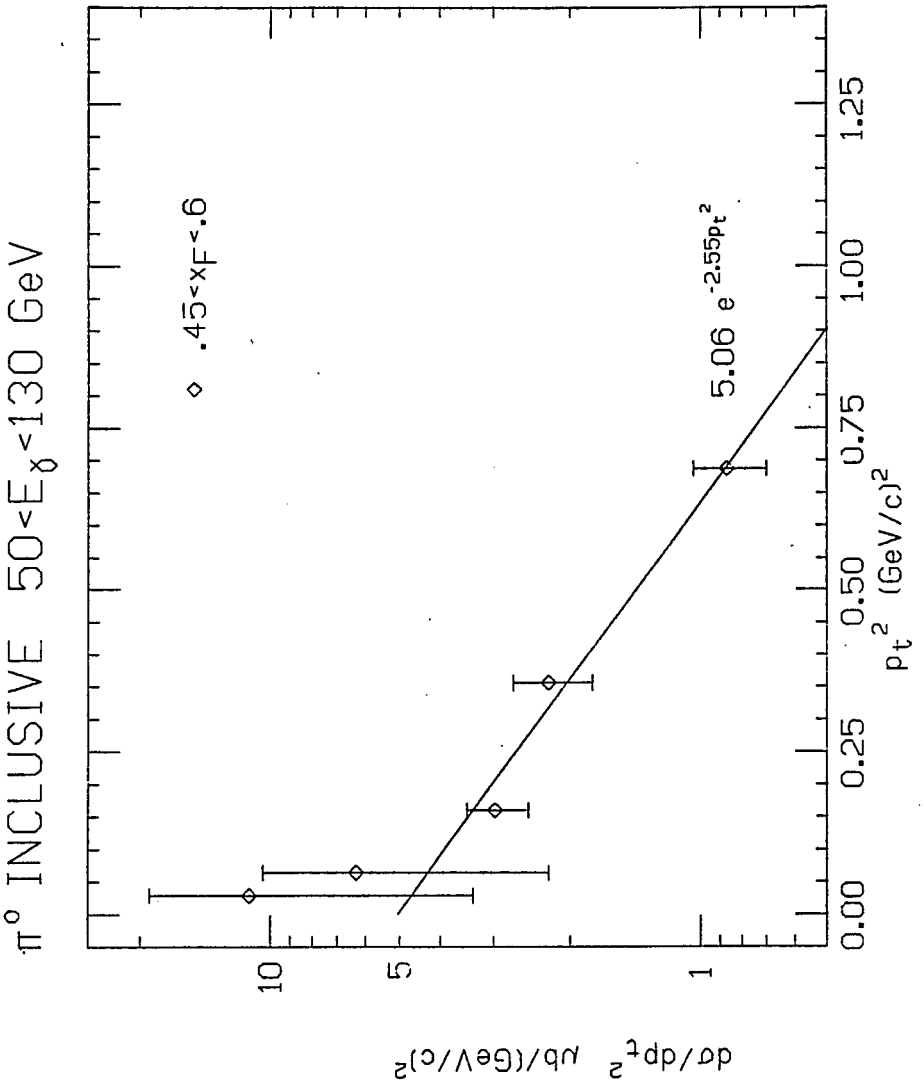

Reproduced with permission of the copyright owner. Further reproduction prohibited without permission.

Figure 5-5c

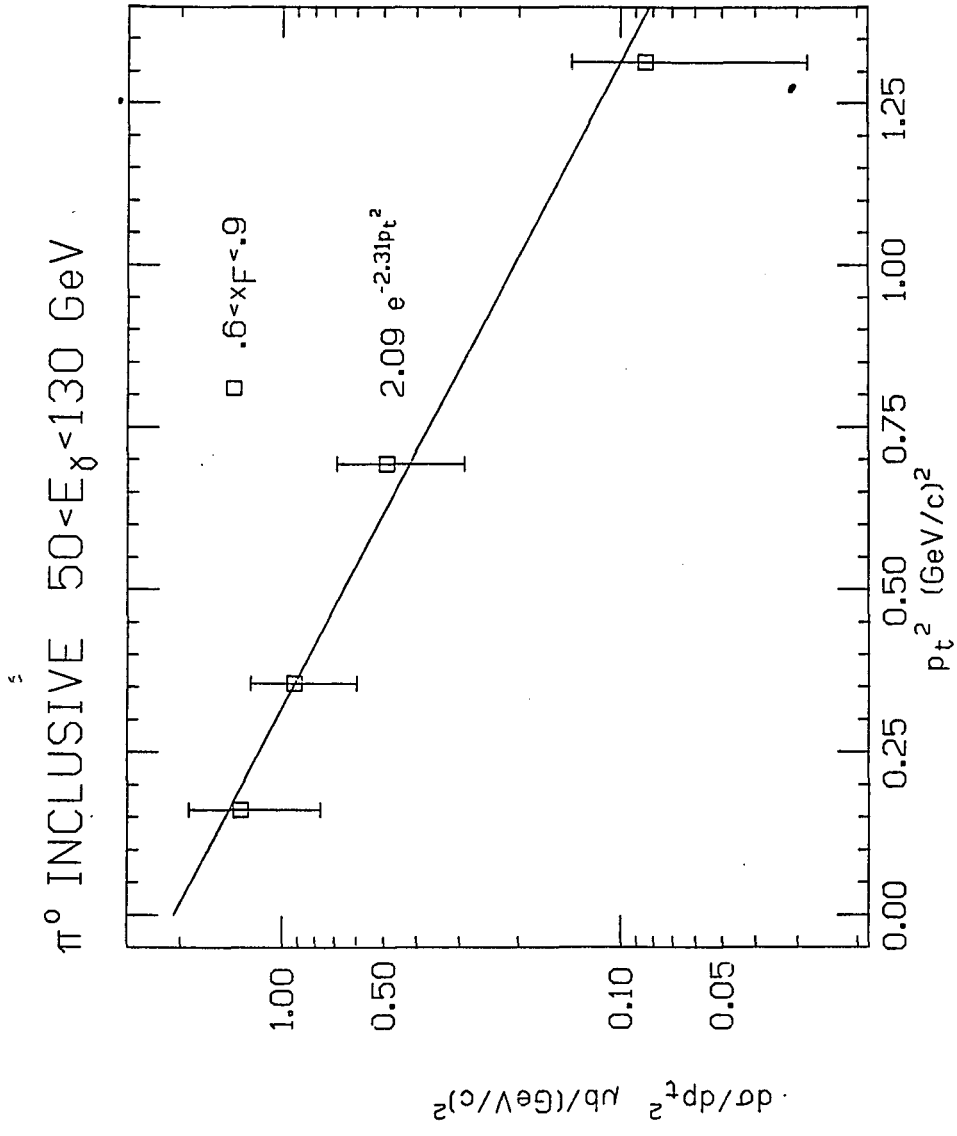

Reproduced with permission of the copyright owner. Further reproduction prohibited without permission.

Figure 5-6

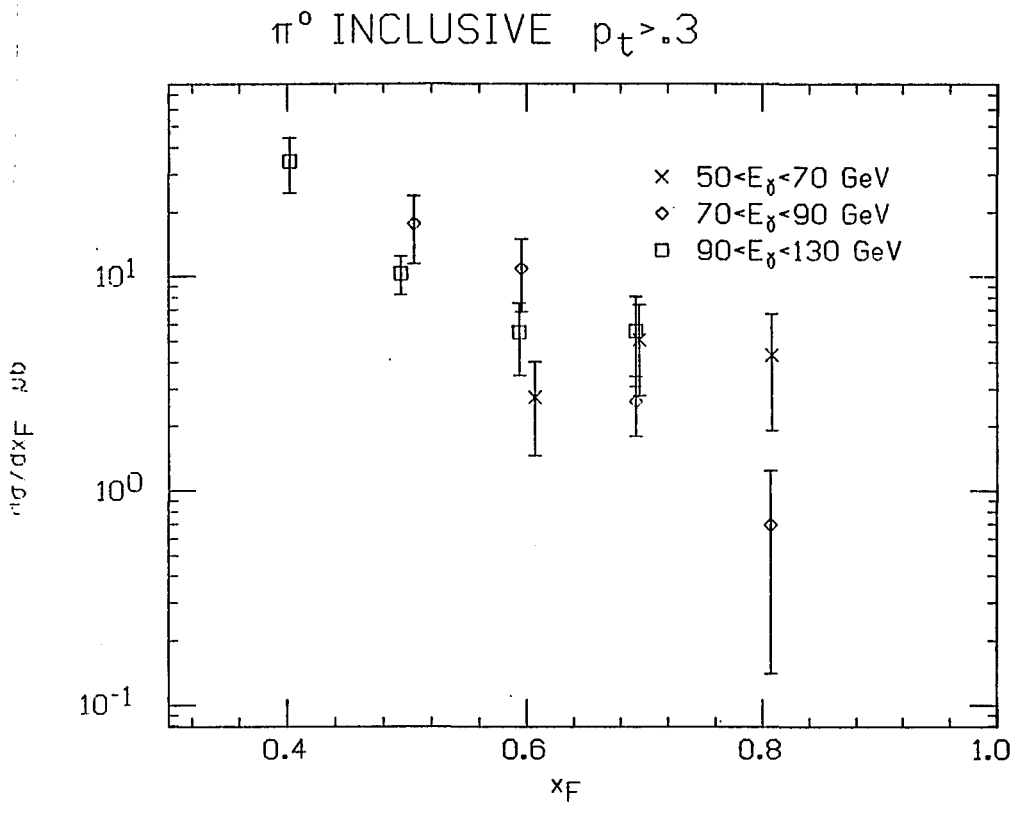

Reproduced with permission of the copyright owner. Further reproduction prohibited without permission.

Figure 5-7

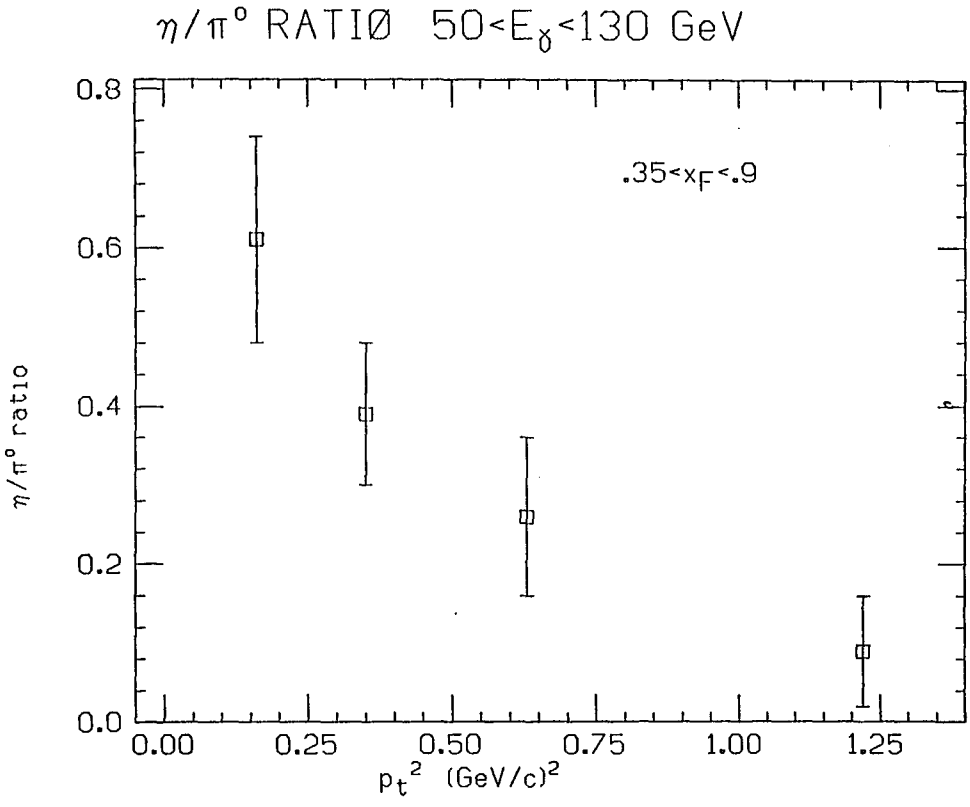

Reproduced with permission of the copyright owner. Further reproduction prohibited without permission.

Figure 5-8

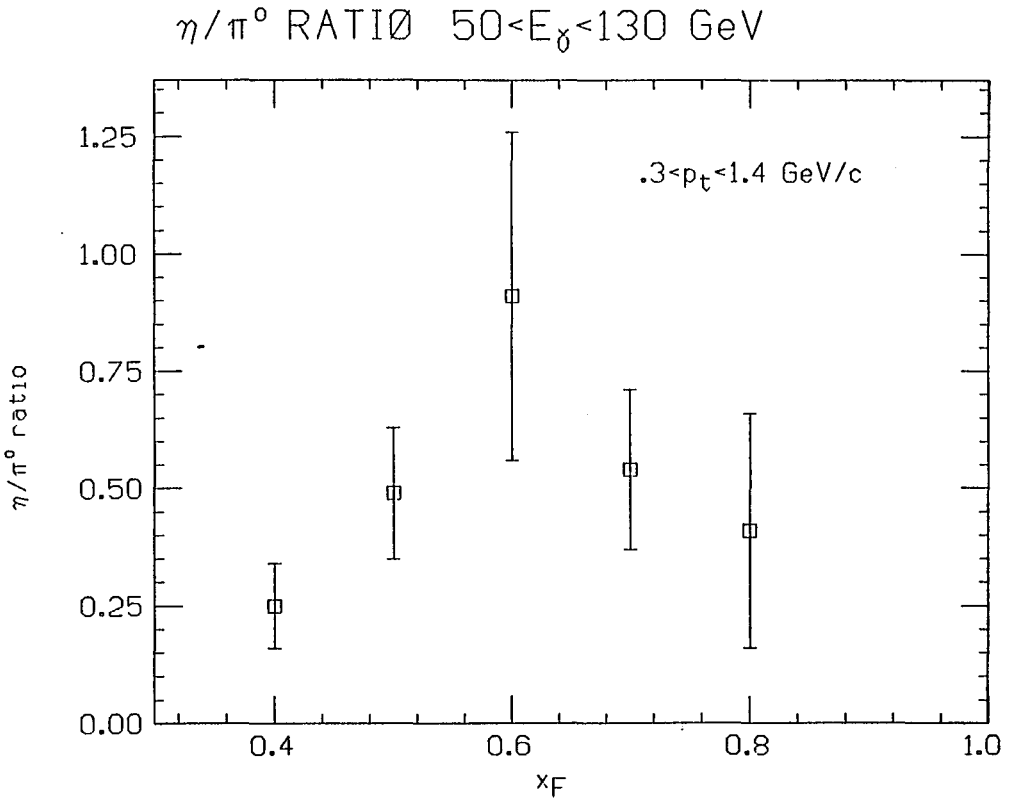

Reproduced with permission of the copyright owner. Further reproduction prohibited without permission.

5.2. Discussion

For the η we observe scaling in both the transverse momentum and Feynman x distributions, as evidenced by the overlap of these distributions for different energies in Figures 5-1 and 5-3. For the π^0(Figures 5-4 and 5-6) the data suggest scaling, although the evidence is not as clear as for the η. This observation of scaling is in accord with expectations from the general features of inclusive scattering discussed in Section 1.1.

The feature of limited transverse momentum suggests an exponential falloff of the transverse momentum distributions. We observe this and have fit these distributions with and exponential of the form

$$\frac{d\sigma}{dp_t^2} = A\ e^{-bp_t^2}$$

for different Feynman x bins. The results of these fits are given in Table 5-7 and are also indicated by the straight lines in the figures. There does not appear to be any systematic increase or decrease in the slope parameter, b, but one must note that the errors are large. If we average over all x_F, we find a slope of 2.9 ± .2 for the η and 2.5 ± .3 for the π^0. In Table 5-8, we compare these results with those from similar fits to the transverse momentum distributions in high energy electroproduction of charged hadrons [Loomis 79], and low energy photoproduction and electroproduction of neutral pions [Berger 73 and 77]. We find

Reproduced with permission of the copyright owner. Further reproduction prohibited without permission.

Table 5-7

Average Transverse Momentum of π^0 and η Mesons

as a Function of Feynman x

Based on Fits of the Form

$$\frac{d\sigma}{dp_t^2} = A\ e^{-bp_t^2}$$

π^0

	x_F Range		
	.35-.45	.45-.6	.6-.9
A $\mu b/(GeV/c)^2$	10.91 ± 1.53	5.06 ± 1.21	2.09 ± 1.46
b $(GeV/c)^{-2}$	2.20 ± 1.16	2.55 ± .46	2.31 ± .63
χ^2/NDOF	.3/2	1.8/3	.3/2
$\langle p_t \rangle$ GeV/c	.58	.55	.60
$\langle p_t^2 \rangle$ $(GeV/c)^2$	.45	.39	.43

η

	x_F Range		
	.35-.45	.45-.6	.6-.9
A $\mu b/(GeV/c)^2$	4.36 ± 1.37	2.20 ± 1.21	1.54 ± 1.12
b $(GeV/c)^{-2}$	3.64 ± 1.31	1.41 ± .66	2.47 ± .25
χ^2/NDCF	1.0/4	3.2/3	5.0/5
$\langle p_t \rangle$ GeV/c	.46	.75	.56
$\langle p_t^2 \rangle$ $(GeV/c)^2$	.27	.71	.41

Reproduced with permission of the copyright owner. Further reproduction prohibited without permission.

Table 5-8

Comparison of Transverse Momenta from Different Experiments

Based on Fits of the Form

$$\frac{d\sigma}{dp_t^2} = A\, e^{-bp_t^2}$$

	b $(GeV/c)^{-2}$	$\langle p_t \rangle$ GeV/c	$\langle p_t^2 \rangle$ $(GeV/c)^2$
This experiment:			
$50 < E_\gamma < 130$ GeV			
$.3 < x_F < .9$			
η $0 < p_t < 1.4$ GeV/c	2.9 ± .2	.52	.34
π^0 $.3 < p_t < 1.4$ GeV/c	2.5 ± .3	.57	.41
$\mu p \rightarrow \mu h^\pm X$ [Loomis 79]			
$E_\mu = 150$ GeV			
$.3 < x_F < .85$			
$0 < p_t < 1.8$ GeV/c	2.6	.55	.38
$ep \rightarrow e\pi^0 X$ [Berger 77]			
$4 < E_e < 7$ GeV			
$.05 < p_t < .8$ GeV/c	4.4	.42	.23
$\gamma p \rightarrow \pi^0 X$ [Berger 73]			
$E_\gamma = 6$ Gev			
$.2 < x_F < .8$			
$.2 < p_t < 1.4$ GeV/c	3.5	.47	.29

Reproduced with permission of the copyright owner. Further reproduction prohibited without permission.

general agreement with the results of these experiments; the average transverse momentum is approximately .5 GeV/c in all cases.

As previously mentioned, the Feynman x distributions exhibit scaling within the errors on the data points. To compare the data with those from other experiments, we have taken $d\sigma/dx$ for our pion data, divided it by the photon-proton total cross section, taken from [Caldwell 78], and plotted the results in Figure 5-9 along with those from [Loomis 79] and [Berger 77]. Our results follow the same trend as the other data, but are systematically low by about a factor of two. This could be due to our systematic errors in extracting the pion data. However, the fact that our data has nearly the same falloff with increasing Feynman x as the other data is in accord with the quark cascade model prediction that similar processes should yield similar Feynman x distributions.

The average value of the η/π^0 ratio taken over all our data is .52 ± .10. This is in good agreement with the value of .55 ± .07 measured in proton-proton collisions at the CERN ISR [Kourkoumelis 79]. We see no clear trend with Feynman x, but the η/π^0 ratio does appear to decrease with increasing transverse momentum. This disagrees with the ISR results, where the η/π^0 ratio is constant over a p_t range from 3 to 11 GeV/c, and with expectations from quark cascade models.

Reproduced with permission of the copyright owner. Further reproduction prohibited without permission.

Figure 5-9

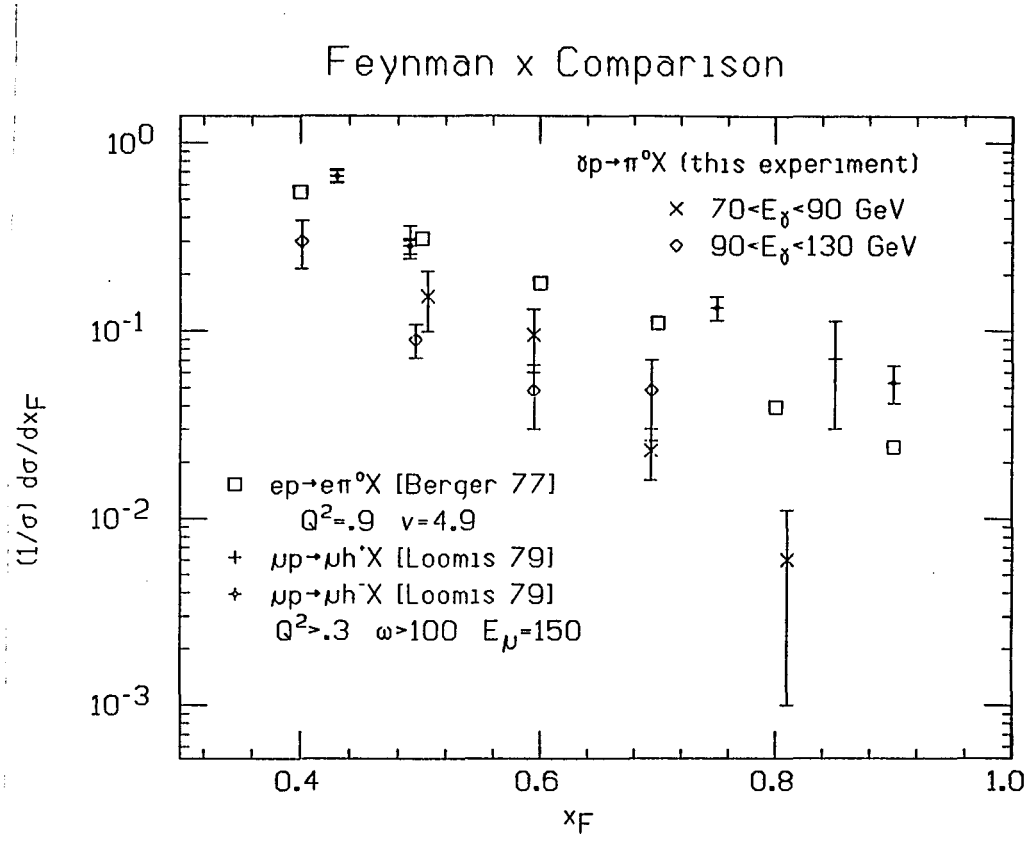

Reproduced with permission of the copyright owner. Further reproduction prohibited without permission.

5.3. Conclusions

We have undertaken a study of inclusive photoproduction of π^0 and η mesons at high energy. We have found general agreement both with other experiments and with predictions of quark cascade models: we find scaling in the inclusive distributions in both transverse momentum and Feynman x, an exponential transverse momentum dependence, rough agreement with others in the Feynman x distribution of pions, and an η/π^0 ratio of approximately one-half. What remains for us to do is a further study of our systematic errors for the inclusive neutral pion data and an extension of both the η and π^0 inclusive cross sections to higher transverse momenta. The data from this thesis, coupled with those of further investigations, will enable us to get a clearer picture of the structure of matter.

Reproduced with permission of the copyright owner. Further reproduction prohibited without permission.

Appendix A

DESIGN AND DESCRIPTION OF FORWARD DETECTOR COMPONENTS

A.1. General Design Considerations

The purpose of the forward detector is to measure the energy and position of electromagnetically showering particles emanating from the target. The various processes to be studied--elastic scattering, inclusive neutral pion and eta production, radiative neutral vector meson decays, inclusive photon production (particularly in the deeply inelastic region), and investigation of high-mass radiatively decaying states--require a tremendous flexibility in terms of energy range, multi-shower ambiguity resolution, and position resolution. Furthermore, one would like the detector to be large enough to simultaneously take data on as many of the above-mentioned processes as possible.

We realized that by separating the functions of energy and position measurement, we could build a large detector much cheaper than a combined function detector such as a lead glass array [Breakstone 74a]. We had also discussed the somewhat more exotic possibility of building a liquid argon shower detector, but decided it was better to stay with a more conventional approach, particularly considering the constraints on the resources of the labs at Santa Cruz.

For the total absorption function, size and cost

Reproduced with permission of the copyright owner. Further reproduction prohibited without permission.

constraints suggest the use of shower counters using ultra-violet transmitting acrylic plastic (plexiglass) interleaved between sheets of lead. There are several possibilities for the position measuring device including magnetostrictive wire chambers, multi-wire proportional chambers (MWPC's), and several counter hodoscope schemes involving either plastic scintillator or plexiglass. We conducted a number of tests in an electron beam at the Stanford Linear Accelerator Center (SLAC) which indicated a counter hodoscope scheme, preferably using plastic scintillator, is superior to MWPC's in both energy and position resolution [Breakstone 74b]. In addition the MWPC would have a more difficult time in resolving multiple showers due to large depositions of energy from delta rays produced in the shower [Grillo 76]. Thus we designed a scintillator hodoscope consisting of two sets of narrow counters at right angles to each other.

We first had to determine where to place the hodoscope in terms of depth of the shower. Fluctuations in the conversion point of the photon require the hodoscope to be at least four radiation lengths (r.l.) into the shower for better than a 98% chance of seeing the shower. In testing prototypes at SLAC we found that although the best energy resolution is obtained at shower maximum, the best position resolution is obtained slightly beyond that with only slightly decreased energy resolution. Since the depth of shower maximum is only a logarithmic function of energy ranging from about 6 to 8 r.l. in the 10 to 100 GeV energy

Reproduced with permission of the copyright owner. Further reproduction prohibited without permission.

range, we decided to place the hodoscope after nine quarter-inch (1.13 r.l.) sheets of lead.

We decided to use seven plastic "fingers" for the front section (U plane) and ten "fingers" for the back section (V plane) of the total absorption counter with a quarter-inch sheet of lead preceding each strip. These numbers represent a compromise between cost and light collection efficiency on one hand and the desire to sample the shower frequently on the other. One extra quarter-inch sheet of lead is placed in front of the entire array to reduce the shower leakage out the back at the lesser cost of losing a little of the pulse height at the front end. The total lead thickness is 4.5 inches or 20.34 radiation lengths. The lead distribution is shown in Figure A-1 which gives a cross-sectional view of the hodoscope and total absorption counters.

Using tables of photon-initiated showers prepared by Crawford and Messel [Messel 70] and the scaling laws expected to be true for showers, I have plotted in Figure A-2 the number of electrons for 10 and 100 GeV showers at a given depth of the shower in terms of radiation lengths of lead. The 10 GeV curve is multiplied by a factor of 10. The depths of the various counters are also shown. At the point where the hodoscope is located, the pulse height is still about 70% of the maximum for 10 GeV showers and over 90% of the maximum for 100 GeV showers, so the energy resolution is only slightly worse than at shower maximum. The

Reproduced with permission of the copyright owner. Further reproduction prohibited without permission.

Figure A-1

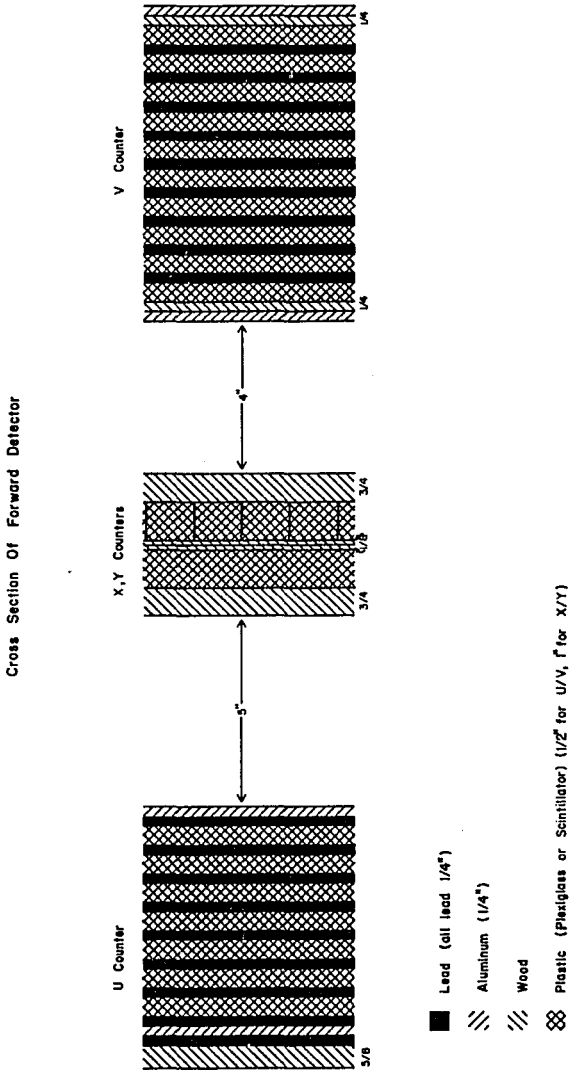

Reproduced with permission of the copyright owner. Further reproduction prohibited without permission.

Figure A-2

Shower Distribution Function

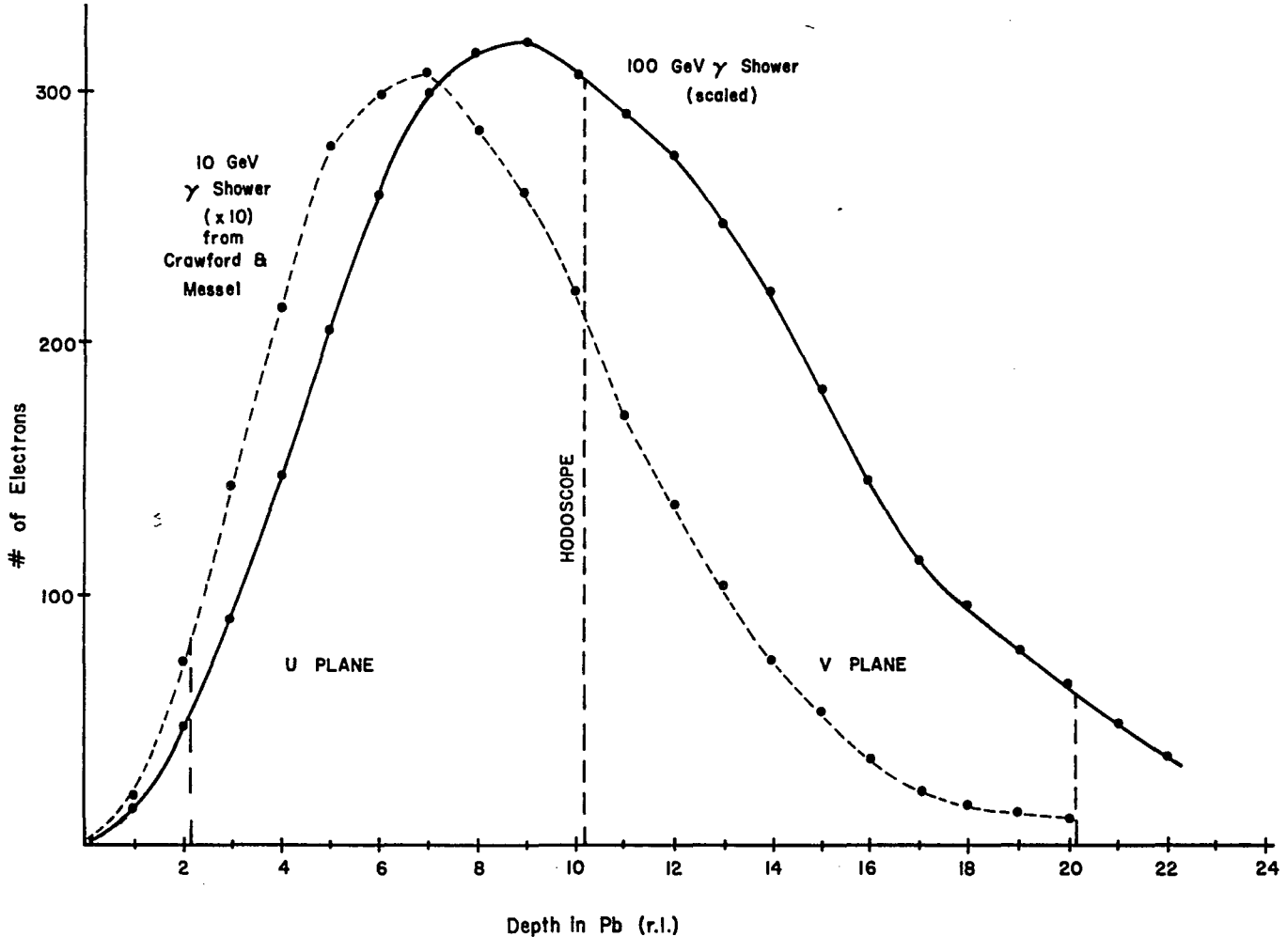

Reproduced with permission of the copyright owner. Further reproduction prohibited without permission.

amount of energy deposition expected is summarized in Table A-1. For showers below 100 GeV, 95% or more of the shower energy is deposited in the U and V planes. Above 100 GeV fluctuations on the shower leakage out the back could be a major source of degradation in the energy resolution.

A.2. Design, Testing, and Assembly of the Total Absorption Counters

We conducted a series of tests in an electron beam at SLAC on prototype total absorption counters to better understand the various design parameters and improve on them if possible [Breakstone 75a]. Three major results were obtained from this test:

1) The attenuation along the length of the counter (approximately 70 cm) is about 30%.

2) The pulse height is proportional to the beam energy and the resolution proportional to the inverse square root of the beam energy for the energy range available (4 to 12 GeV). The only difficulty with this is that the magnitude of the energy resolution, which when extrapolated to 100 GeV would give $\sigma = 4\%$, is about twice what we had hoped.

3) Investigation of the energy resolution problem revealed that it is primarily due to low photoelectron statistics at the photocathode.

These tests resulted in a two-pronged effort to optimize the design of the counters. First I wrote a Monte Carlo program [Breakstone 75c] to generate photons randomly on the Cherenkov cone for normally incident $\beta = 1$ particles (42° for plexiglass with index of refraction 1.50) at a given point on the surface of one of the strips, follow each photon to

Reproduced with permission of the copyright owner. Further reproduction prohibited without permission.

Table A-1

Expected Energy Deposition in the Total Absorption Counters

	Percentage of Total	
	10 GeV	100 GeV
Before U plane	2	1
In U plane	72	48
In V plane	25	47
After V plane	1	4

Reproduced with permission of the copyright owner. Further reproduction prohibited without permission.

see if it gets to the phototube and, if so, to see where it hits. I also allow for the possibility of absorption of photons with a somewhat conservatively estimated absorption length of one meter. Photons hitting the walls at angles less than the critical angle (42° for plexiglass) are assumed to be lost. Most of the photons which start out going towards the end of the counter away from the phototube are lost. The major loss for those headed toward the phototube occurs where the strips are bent and tapered to match the counter to the phototube. The goal that became apparent is to reduce the bends as much as possible. Since the thickness of the strips had to remain at one-half inch to keep the amount of light generated from being reduced, the distance between the strips was decreased from one-half to three-eighths of an inch to allow the bends on the outer strips to be somewhat less severe.

An interesting result of the Monte Carlo is that each strip tends to focus light on a different section of the phototube. This focusing is particularly strong for the outer strips where the focusing region is less than double the strip width. The most controversial result of the Monte Carlo concerns the shape of the plexiglass block to which the strips are glued. Traditionally it is tapered from a square or rectangular shape to a circular shape the size of the phototube with the idea that the photons are funneled onto the tube. The Monte Carlo showed that more photons are lost by doing his than by putting the phototube directly

Reproduced with permission of the copyright owner. Further reproduction prohibited without permission.

onto the square or rectangular block, allowing those that hit the corners to miss the phototube.

According to the Monte Carlo calculations, these improvements tripled the light collection efficiency of the new design over the prototype. About 10% of the photons generated at the center of the 18 cm x 72 cm active area of the counter make it to the phototube for the new design. Figure A-3 shows the final design for the U and V counters.

Concurrently with the Monte Carlo studies, we tested a number of five-inch diameter photomultiplier tubes at Santa Cruz using LED's and on the prototype counter at SLAC in an electron beam [Breakstone 75a and 75b]. We found that the key criterion is the phototube's spectral response. For Cherenkov light, the number of photons per unit wavelength is inversely proportional to the wavelength, so the light is peaked towards the ultraviolet. UVT plexiglass has a sharp transmission cutoff at 300 nm. Thus we want the phototube with the highest quantum efficiency near 300 nm. This calls for a tube with a bialkali or trialkali photocathode. We found that the energy resolution of the prototype total absorption counter at 8 GeV is 19% FWHM with a trialkali variant of the RCA 4522, whereas it is 32% FWHM for the monoalkali Amperex XP1040. This impressive difference points out the value of matching phototube spectral response to the spectrum of light generated. After testing a number of different phototubes, we decided to use the RCA 4525, a

Reproduced with permission of the copyright owner. Further reproduction prohibited without permission.

Figure A-3

Total Absorption Counters

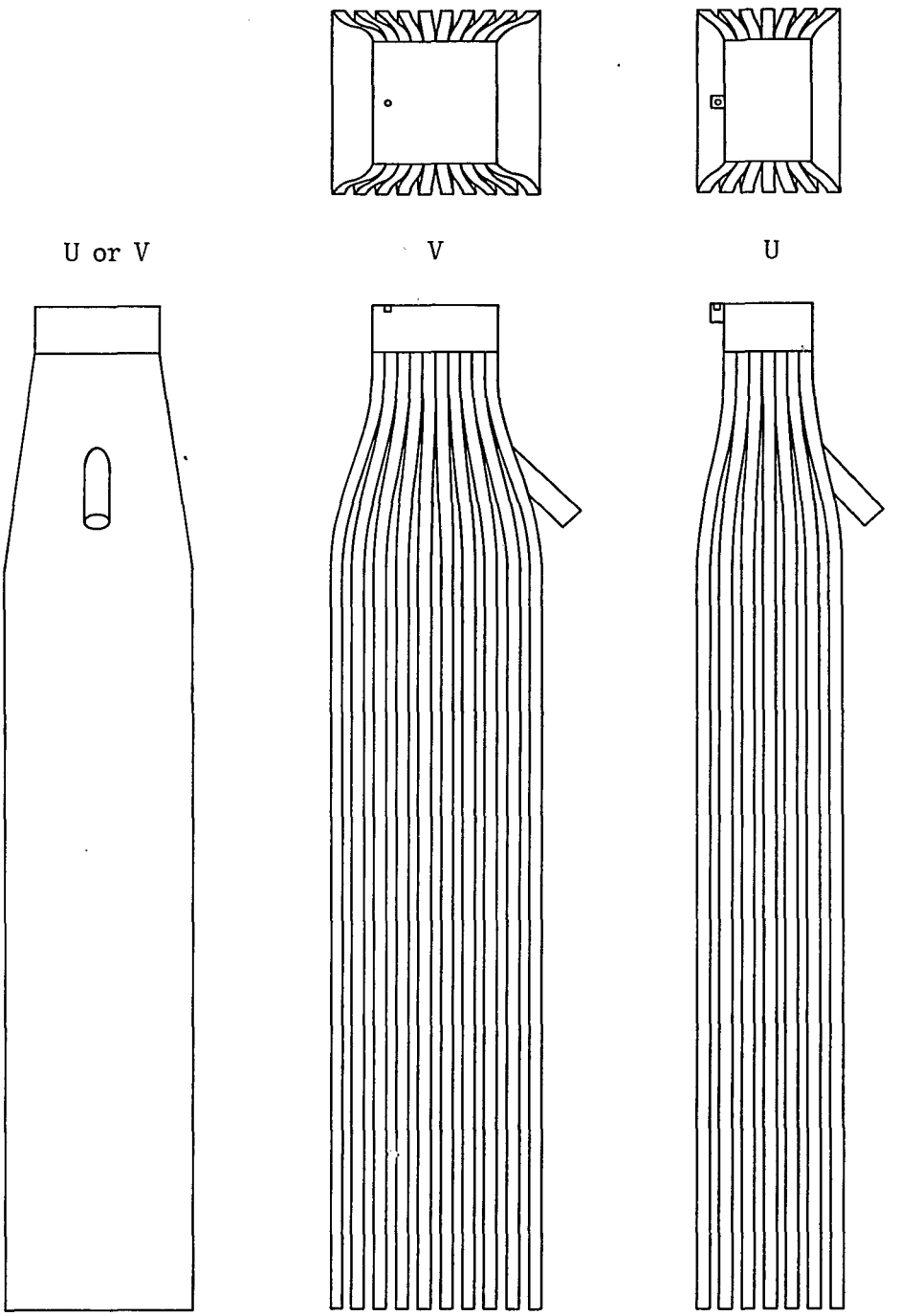

Reproduced with permission of the copyright owner. Further reproduction prohibited without permission.

10-stage, bialkali tube, for its good performance at low cost.

Finally there is the matter of designing a base for the RCA 4525 tube. Since the counters have rates well below a megahertz, we use a simple resistor chain for the voltage division with capacitors on the last five stages to keep the voltage constant for large pulses. We provided for two dynode outputs to allow daisy-chaining several tubes together to serve as a trigger on showers produced in the forward detector. The circuit diagram for this base is given in Figure A-4.

The total absorption counters (16 U counters and 16 V counters) were built by Nuclear Enterprises, Inc., in San Carlos, California. In Santa Cruz we glued an LED fixture and an americium-241 source onto each counter (see Appendix C for more details). We then wrapped each finger of the counters with one layer of .0005 inch thick aluminized mylar followed by one layer of white paper approximately .0045 inch thick. This provides for optical isolation of the fingers and protection against the lead tearing the aluminized mylar when the counters and lead are assembled. The outside face of the outer fingers and the region where the counter tapers to the block are also wrapped with black paper tape (.006 inch thick) and black plastic tape (.01 inch thick) to protect the counter during handling. No attempt was made to make the counters light tight at this

Reproduced with permission of the copyright owner. Further reproduction prohibited without permission.

Figure A-4

RCA 4525 Base Circuit Diagram

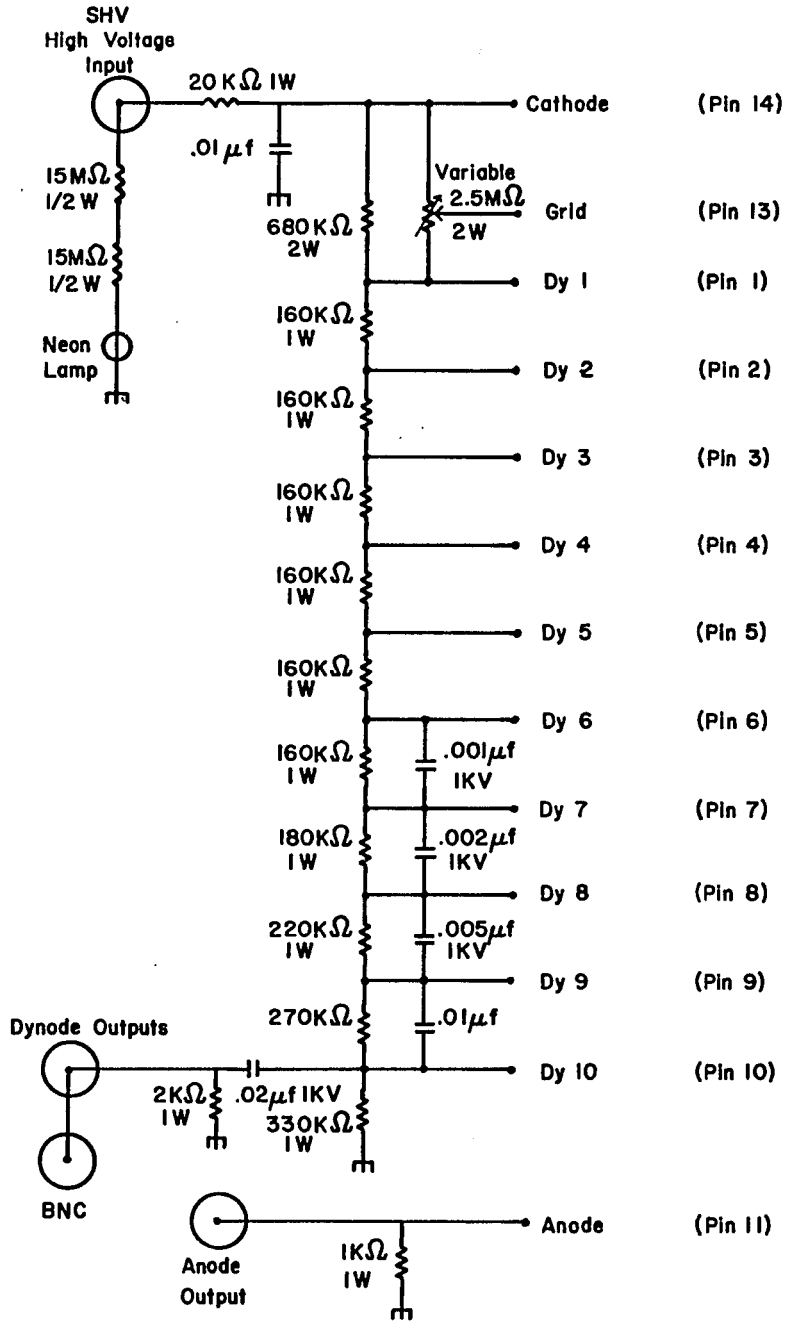

Reproduced with permission of the copyright owner. Further reproduction prohibited without permission.

stage.

We assembled the counters into modules at Fermilab. One module consists of four counters adjacent to each other with lead in between the fingers forming an active area of 72 cm x 72 cm. The front and back cover plates are one-quarter inch thick aluminum sheets with holes drilled into them to accomodate the LED fixtures and mounting bolts. The side and end plates are made of sheet aluminum 1/32 inch thick bent to fit over the cover plates. This leads to a minimum separation of 1/16 inch between quadrants. The sheet aluminum is taped to the cover plates with 10 mil black plastic tape to make the entire module light tight. To provide for electrostatic shielding, the phototubes are wrapped with aluminum foil with a 20 MΩ resistor connecting it to the cathode pin on the tube socket. This is followed by a layer of mylar and kaptan tape for electrical insulation. For magnetic shielding we use a shell of conetic alloy (Perfection Mica #23P68X57) which also provides a mechanical housing for the tube which is held to the counter with a spring loaded system. We use optical grease (Dow Corning Q-2-3067) for the optical coupling of the phototube to the counter.

A.3. Design, Testing, and Assembly of the Hodoscope

The hodoscope consists of two perpendicular planes of long, thin strips running the length of the active area of

Reproduced with permission of the copyright owner. Further reproduction prohibited without permission.

the total absorption counters. Since the counters are approximately 1.5 m long, we were quite concerned about the attenuation properties of the material as well as the amount of light produced in it. We tested three plastics: plexiglass, Pilot 425 (plexiglass doped with a wave shifter), and scintillator. The ratio of light production is approximately 1 : 1.5 : 10. The attenuation properties of all three are about the same; each has approximately a factor of two variation in pulse height over a length on the order of one meter. We chose to use scintillator of 25 mm thickness for maximum light production. Tests at SLAC had shown that a 3 cm width is sufficient to give a position resolution better than 1 cm. To provide for a hole in the array for the unscattered beam to pass through, we made a set of shorter strips. We used a width of 2 cm primarily to give us more flexibility in varying the size of the beam hole by varying the number of strips used in the center sections.

Tests were conducted at Santa Cruz on 1.5 inch diameter phototubes to determine the relative merits of a bialkali versus monoalkali photocathode. The bialkali tubes (RCA 4517) produce a 50% larger pulse height than the monoalkali (RCA 6199) tubes. Since its cost was only marginally more, we chose the 4517 and its counterpart manufactured by Amperex, the PM2012B.

The phototube base was designed with the same low-rate considerations as the one for the total absorption counters.

Reproduced with permission of the copyright owner. Further reproduction prohibited without permission.

The circuit diagram is given in Figure A-5. We made special bases with two anode outputs for counters to be used for the muon and americium source monitors.

The scintillator (Rohaglas #1921) was purchased from Rohm GMBH Chemische Fabrik in Darmstadt, Germany. There are 96 strips of size 158 cm x 3 cm x 2.5 cm and 16 strips of size 92 cm x 2 cm x 2.5 cm. The short strips are bent so the phototubes and bases can be attached without interference, while for the long strips no bending is necessary because adjacent strips have their phototubes on opposite ends of the array. Every strip is wrapped with one layer of .0005 inch thick aluminized mylar with alternate strips additionally wrapped with one layer of white paper .0045 inch thick. The long strips are mounted on 3/4 inch thick plywood boards in groups of twenty-four to form an active area of 72 cm x 158 cm. The strips are then covered by 1/8 inch thick masonite with grooves cut for the fiber optics of the LED system (see Appendix C for more details on this), followed by black paper tape (.006 inch thick), and black plastic tape (.01 inch thick) to make the entire unit light tight. The short strips are similarly mounted in groups of four counters, providing an active area of 8 cm x 75 cm. One of the outer strips in each group of four was cut 8 cm shorter than the others to provide extra clearance for the phototubes without having to bend the strip additionally.

The mechanical coupling to the phototube is provided by

Reproduced with permission of the copyright owner. Further reproduction prohibited without permission.

Figure A-5

RCA 4517 Base Circuit Diagram

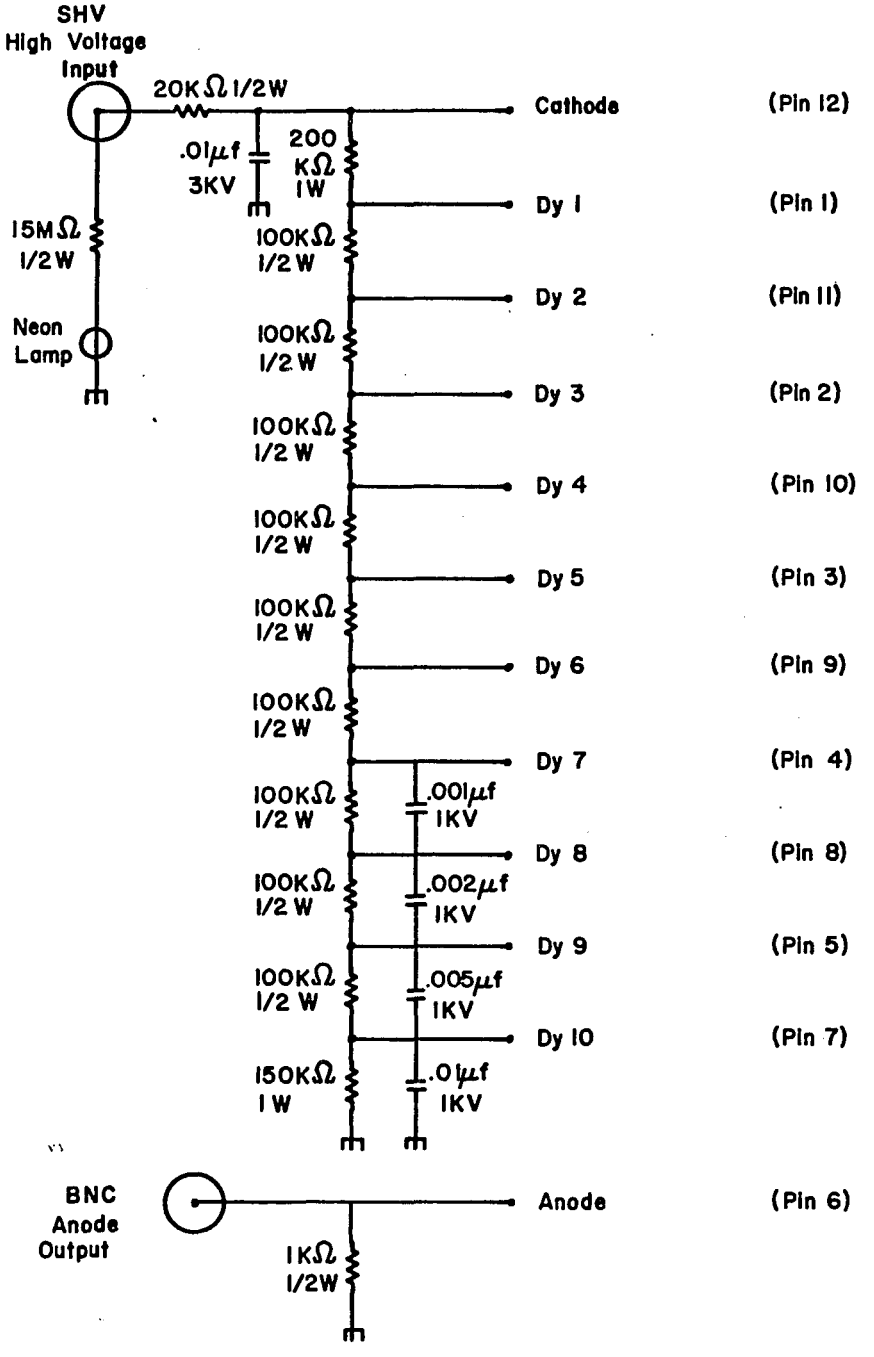

Reproduced with permission of the copyright owner. Further reproduction prohibited without permission.

a threaded 1.5 inch diameter circular block of plexiglass 3/8 inch thick glued onto the end of the counter. The phototube has a polyvinyl chloride (PVC) collar glued to it and is then screwed onto the block with optical grease (Dow Corning Q-2-3067) providing the optical coupling. The outside of the tubes are coated with a conducting paint (GC Electronics #49-2 Television Tube Coat) connected to the photocathode pin of the socket through a 10 MΩ resistor for electrostatic shielding. They are electrically insulated with mylar tape and magnetically shielded using .004 inch thick conetic foil (Advance Magnetics AD-MU #78).

A.4. Overall Assembly

Before assembling the hodoscope and total absorption counters together into a single unit, we had to decide how to orient the various pieces with respect to each other. There are three major parameters to deal with: the size of the hole for the beam, the angle of the hodoscope with respect to the U and V planes, and whether the U and V counters should be parallel or perpendicular to each other. The major concerns are ease in mechanical mounting and in reconstruction of the position and energy of showers versus multi-shower ambiguity resolution.

The major factor in determining the hole size is the size and divergence of the beam. By studying the rate dependence of the U and V counters at a distance of 20 m

Reproduced with permission of the copyright owner. Further reproduction prohibited without permission.

from the hydrogen target as a function of horizontal position, we determined the horizontal width which encloses 90% of the beam to be approximately 2.2 cm. This is roughly verified by looking at the segmented wire ionization chamber (SWIC) at 30 m from the target. The vertical width is somewhat smaller, but also on the order of 2 cm. Since the beam steering and focusing as well as the physical size of the radiator strongly affect this spot size, the beam aperature must be much larger than this. We also want the hole as small as possible to avoid losing particles from good events. We determined empirically that a square hole 8 cm x 8 cm is adequate for our purposes. This leads to a minimum angle of 1.3 mr for a particle emanating from the target to hit the detector if it is 30 m away. This corresponds to $|t| = .02$ $(GeV/c)^2$ for 100 GeV elastic photon-proton scattering. This is much smaller than the limit due to the proton stopping in the target.

To determine the effects of the orientations of the U and V counters and hodoscope, I wrote a Monte Carlo program to simulate elastic scattering, quasi-elastic vector meson production, and general background type events (multiparticle production) [Breakstone 77a]. The first two programs are rather straight-forward since all the kinematical properties of the initial and final states are determined by two parameters which I choose to be the azimuthal angle (ϕ), chosen uniformly from 0 to 2π, and the square of the four-momentum transfer (t), chosen according to a simple

Reproduced with permission of the copyright owner. Further reproduction prohibited without permission.

exponential distribution. The background events are generated using a scheme of quark-antiquark annihilation invented by Abe Seiden [Seiden 76]. An exponential transverse momentum spectrum is used which fits experimental data well for transverse momenta below about 1 GeV/c, but fits it poorly above that.

The first question we address is whether the U and V counters should be parallel or perpendicular to each other. For the parallel case, pairs of showers which hit the same U counter also hit the same V counter and thus their individual energies are not well determined. For the perpendicular configuration, if the pair hits the same U it need not hit the same V and vice versa. Thus there are three different types of ambiguities of varying severity. The resolution of these ambiguities depends on how well one can assign an energy to a shower on the basis of the U or V plane alone. For the detector 30 m from the target, about 25% of the background events have at least one ambiguous pair for the parallel case, whereas this is 37% for the perpendicular case, although of these only about one-third hit both the same U and V counter. These numbers are only slightly dependent on the energy cut we place on showers. It is interesting to note that most of the ambiguities are caused by uncorrelated photons (i.e. photons not from the same pion), especially in the perpendicular case. Since the ability of the U and V counters to separately determine shower energies is poor and the number of ambiguous events

Reproduced with permission of the copyright owner. Further reproduction prohibited without permission.

is not too large in the parallel case, we chose to go to the parallel configuration. For ease in mounting and phototube access, we put all the total absorption counters in a horizontal position.

Finally I ran the Monte Carlo to determine whether or not the hodoscope should be at an angle to the U and V counters. The key point is that the pulse height information helps tremendously to resolve ambiguous events. Assuming that shower fluctuations cause an error in assigning an energy to the shower using the hodoscope alone is $\sigma = 100\% / \sqrt{E}$, we found that only 4% of the ambiguities remain, independent of orientation of the hodoscope. Since only this small number of ambiguities can be further reduced by putting the hodoscope at an angle to the total absorption counters and since doing this reduces the overlap of the two, we decided not to rotate the hodoscope.

Thus we arrived at the overall assembly as depicted in Figures 2-10 and 2-11 in the main text. The cart on which we mounted the detector can move horizontally transverse to the beam as well as longitudinally along the beam direction, giving us great flexibility in positioning the forward detector.

Reproduced with permission of the copyright owner. Further reproduction prohibited without permission.

Appendix B

FORWARD DETECTOR CALIBRATION PROCEDURES AND RESULTS

B.1. General Remarks

In order to reconstruct showers, a calibration of the forward detector with showers of known energy is required. The calibration must provide a function to relate the pulse height in the counter to the shower energy and the error on that function for both the total absorption counters and the hodoscope. It must provide information concerning the lateral and longitudinal spread of showers to determine how to add pulse heights from adjacent counters, how to correct for shower energy losses at the edges of the detector, and what ratio to use in adding the pulse heights of the U and V counters as a function of energy. It must also give the position and energy resolution of the detector as a whole and, finally, it must provide an initial value for the relative gains and a calibration of the monitors for each counter in the forward detector. Subsequent gain tracking as a function of time is provided by the monitoring systems described in Appendix C.

B.2. Calibration Procedures

Two major calibration runs were conducted in September-October of 1977 and in May of 1978. Prior to the

Reproduced with permission of the copyright owner. Further reproduction prohibited without permission.

time of the first calibration, we had conducted two series of tests on sections of the forward detector described in [Breakstone 76e and 77b].

The procedures for each of the two sets of calibration runs are virtually identical. The forward detector is at a position approximately 30 meters downstream of the hydrogen target. Immediately upstream of the recoil house is a bending magnet set on circular gymbals so that it can be rotated. It has sufficient bending power to bend a 30 GeV electron beam over the entire forward detector's active area. The trigger used is a coincidence between the counter denoted TFAKE in Figure 2-5 and a sum of the pulse heights in the total absorption counters in anticoincidence with various veto counters to eliminate beam halo particles from the trigger. Typically the collimators in the beam are set to give a few thousand electrons per beam spill.

The calibration consists of a series of runs of about 500 to 1000 triggers, each one defined by a certain set of conditions (magnet setting, forward detector position, beam energy, etc.). The majority of these runs consist of a detailed scan of the detector with a 30 GeV electron beam to establish the relative gains of all the counters, the attenuation functions, and edge effects. The typical gain variations for the total absorption counters are ± 25% with the error in determining the gain of about 2%. For the hodoscope the gain variations are not much larger, about

Reproduced with permission of the copyright owner. Further reproduction prohibited without permission.

± 40%, but the error in determining them is about 10%, due primarily to the large fluctuations in pulse height in a single strip. Still this is quite sufficient to keep systematic errors in determining the position of the centroid of a shower below 2 mm.

In addition to the scans with the 30 GeV electron beam, we changed the beam energy to various values ranging from 15 to 185 GeV for one position in the detector. This is required to establish the energy-versus-pulse height curve, the error in assigning shower energy from a given pulse height, and to find the optimal ratio to add the U and V counters together as a function of shower energy.

Finally we changed over to a tagged photon beam to establish the differences between incident electrons and photons. One expects some differences, particularly in the hodoscope pulse heights, since on the average the shower develops further into the detector for incident photons than for incident electrons.

B.3. Analysis and Results

The previously described set of calibration runs established all the performance parameters of the forward detector for single showers. In this section I will describe the analysis of the calibration data, discussing the results as they are presented. Further details may be found in [Breakstone 77c and 78a, b, c, and d].

Reproduced with permission of the copyright owner. Further reproduction prohibited without permission.

B.3.1. Attenuation Functions and Gains

The first step is to establish the attenuation functions and relative gains for the total absorption and hodoscope counters so that pulse heights measured in one part of the detector can be normalized to those in another part.

Using a set of runs comprising a horizontal scan, I have plotted in Figure B-1 the pulse height as a function of position along the length of typical U and V counters. Note that the attenuation in the V counter is greater than in the U counter, but for both there is little attenuation beyond 30 cm. The solid lines in the figure are fits to the attenuation function as follows:

For the U counters:

$$f(D) = 1.2 - 1.1 \times 10^{-2} D + 1.72 \times 10^{-4} D^2 - 8.86 \times 10^{-7} D^3$$

For the V counters:

$$f(D) = 1.71 - 5.1 \times 10^{-2} D + 1.18 \times 10^{-3} D^2 - 9.0 \times 10^{-6} D^3$$

where the functions are normalized so that f(30 cm) = 1.

For the hodoscope the attenuation function is somewhat more difficult to extract. The reason for this is that there are systematic shifts in beam position and, hence, in pulse height, when we move the cart or rotate the magnet to cover a different section of the counter. A shift of only one millimeter yields approximately a 10% change in pulse height in the strip containing the bulk of the shower

Reproduced with permission of the copyright owner. Further reproduction prohibited without permission.

Figure B-1

Total Absorption Counter Attenuation Function

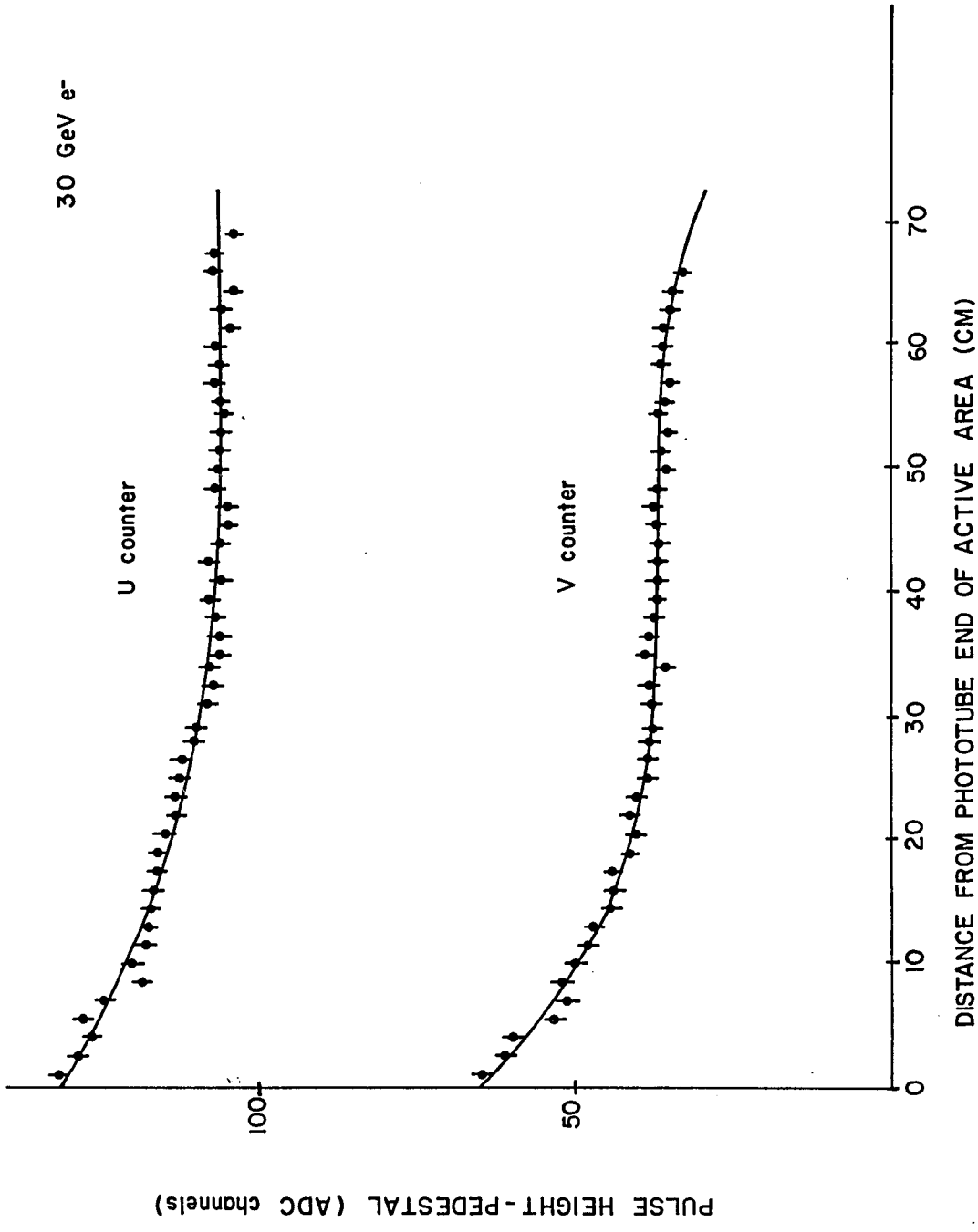

Reproduced with permission of the copyright owner. Further reproduction prohibited without permission.

energy. By matching the values of the pulse heights at the borders of each of these sections to normalize the results of each set of runs, one can arrive at the composite curve shown in Figure B-2. The solid line is a fit to the function

$$f(D) = N\ (e^{-D/L_o} + e^{-(2L-D)/L_o})$$

where N is a normalization chosen such that $f(L/2) = 1$,

D is the distance from the point to the phototube,

L is the length of the counter, and

L_o is the attenuation length. This curve is what one would expect from a simple exponential absorption of photons with perfect reflection off the end of the counter opposite the phototube. For the long strips, for which L = 158 cm, the attenuation length which yields the best fit is L = 150 cm, whereas for the short strips in the center of the hodoscope array, for which L = 92 cm, L = 75 cm. This apparent difference in attenuation length is due to the geometrical loss of light due to the bending of the light pipes for the short strips as opposed to any real difference in the absorption properties of the plastic.

The procedure for obtaining the relative gains of the U and V counters is very simple. The 30 GeV electron beam is directed at a point approximately in the center of the active area of the counter. Using the known attenuation function, the average pulse heights from each counter are corrected for the small differences in position of the beam

Reproduced with permission of the copyright owner. Further reproduction prohibited without permission.

Figure B-2

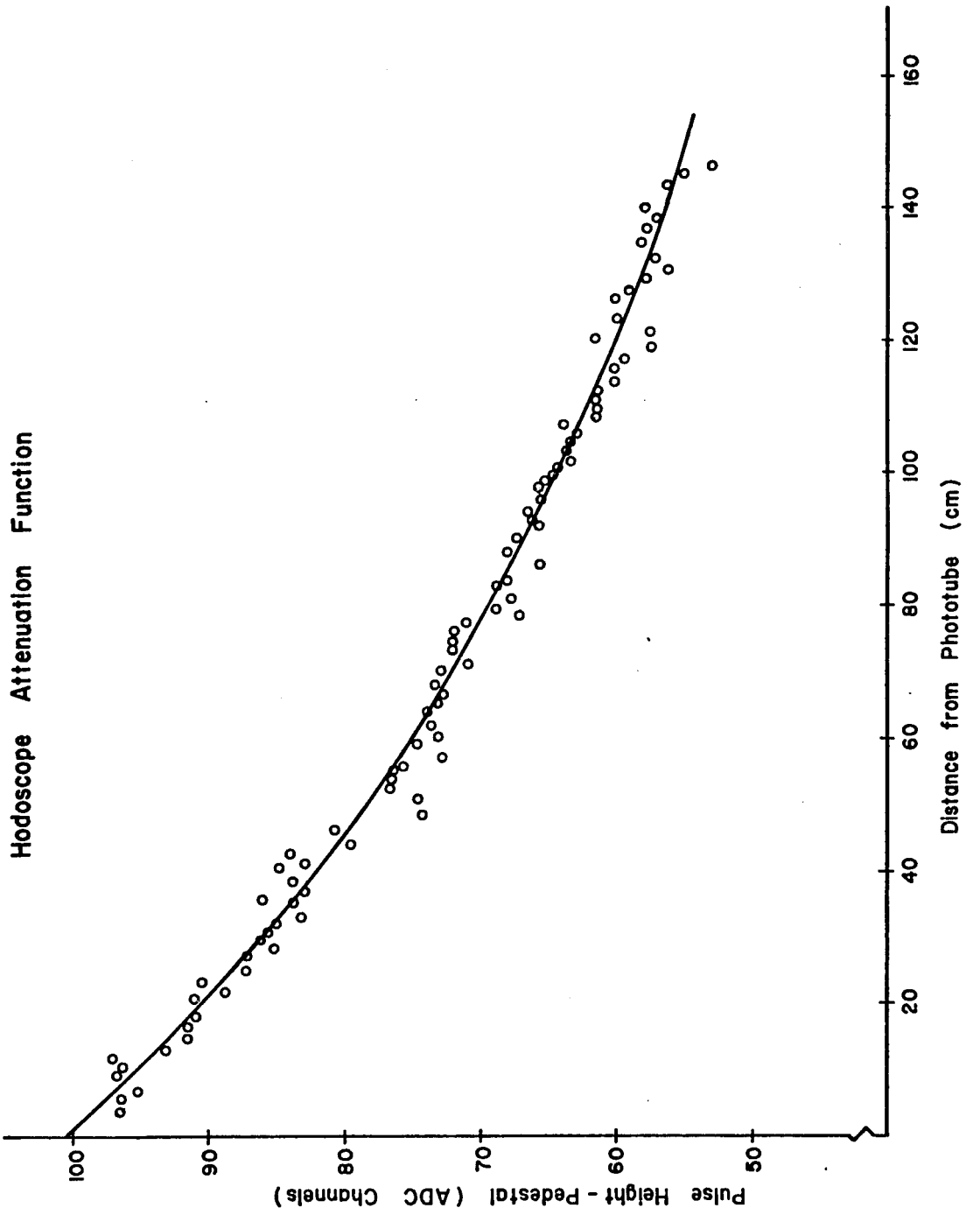

Reproduced with permission of the copyright owner. Further reproduction prohibited without permission.

relative to the counter. With U13 and V13 chosen as the standard counters for which the gain is defined to be 1.00, the relative gains of the other counters are given by the ratio of the corrected average pulse height to that of U13 and V13. For the U counters the variation in the gains is ± 10% with an estimated error in determining the gains of 1%. For the V counters, the high voltages were not set quite so carefully, so the gain variation is ± 25% with an estimated error of 2% on each gain.

For the hodoscope a two-pass procedure is used to establish the gains. On the first pass the maximum average pulse height taken over a set of runs that sweep across the counter is determined. This number is then simply divided by fifty to obtain the gain. Fifty is chosen as the nominal value a counter should have if a 30 GeV shower is centered on it. On the second pass the first pass gains are used in conjunction with the attenuation function to get a more accurate estimate of the gain by summing the average pulse heights of all the strips hit and adjusting the gains of the central three strips to get the sum to be a more or less constant value over a set of runs which sweep across that set of counters. Using this procedure I have established relative gains for all the hodoscope counters which are good to approximately 10%. The variation in the gains is about ± 40%.

Reproduced with permission of the copyright owner. Further reproduction prohibited without permission.

B.3.2. Lateral Shower Spread

Due to the gaps between the U plane and the hodoscope and the V plane, there is a great deal of lateral spreading of showers. Table B-1a gives the pulse heights in adjacent U and V counters as a 30 GeV electron beam is swept across them. The shower is much wider in the V counters than in the U counters as can be seen by comparing the ratios U12/U11 versus V12/V11. For example, at 2 cm from the edge of the counters, U12 is 12% of U11, whereas V12 is almost half of V11. This is to be expected since the shower has a chance to spread laterally in the air gap between the U and V planes. The percentage of the shower seen in adjacent counters for the sum of U and V as a function of lateral distance is given in Table B-1b and Figure B-3.

For the hodoscope the shower typically spreads over nine strips (27 cm). The front plane of the hodoscope has a slightly greater shower spread than the plane behind it due to absorption of some of the soft component of the shower which tends to go at a wider angle than the hard component. I will discuss the width of showers in the hodoscope more quantitatively in Section B.3.5.

B.3.3. Longitudinal Shower Development

As is well known, the shower maximum moves deeper into the total absorption counters as the shower energy increases. We have measured the pulse heights in the total

Reproduced with permission of the copyright owner. Further reproduction prohibited without permission.

Table E-1

Lateral Spread of Showers in the Total Absorption Counters

a) Pulse Heights

Distance From Edge (cm)	Pulse Height Minus Pedestal Corrected for Gain (ADC channels)				
	U11	U12	V11	V12	Sum
9	114	0	36	3	153
6	113	1	34	5	153
4	111	2	33	7	153
2	100	12	28	13	153
1	75	37	25	19	156
0	55	57	21	21	154
-1	34	78	17	25	154
-2	13	100	10	32	155
-4	3	110	6	37	156
-6	1	113	4	39	157

b) Percentage of Shower seen by U + V

Distance From Edge (cm)	U11 + V11 (%)	U12 + V12 (%)
9	98	2
6	96	4
4	94	6
2	84	16
1	64	36
0	49	51
-1	33	67
-2	15	85
-4	6	94
-6	4	96

Reproduced with permission of the copyright owner. Further reproduction prohibited without permission.

Figure B-3

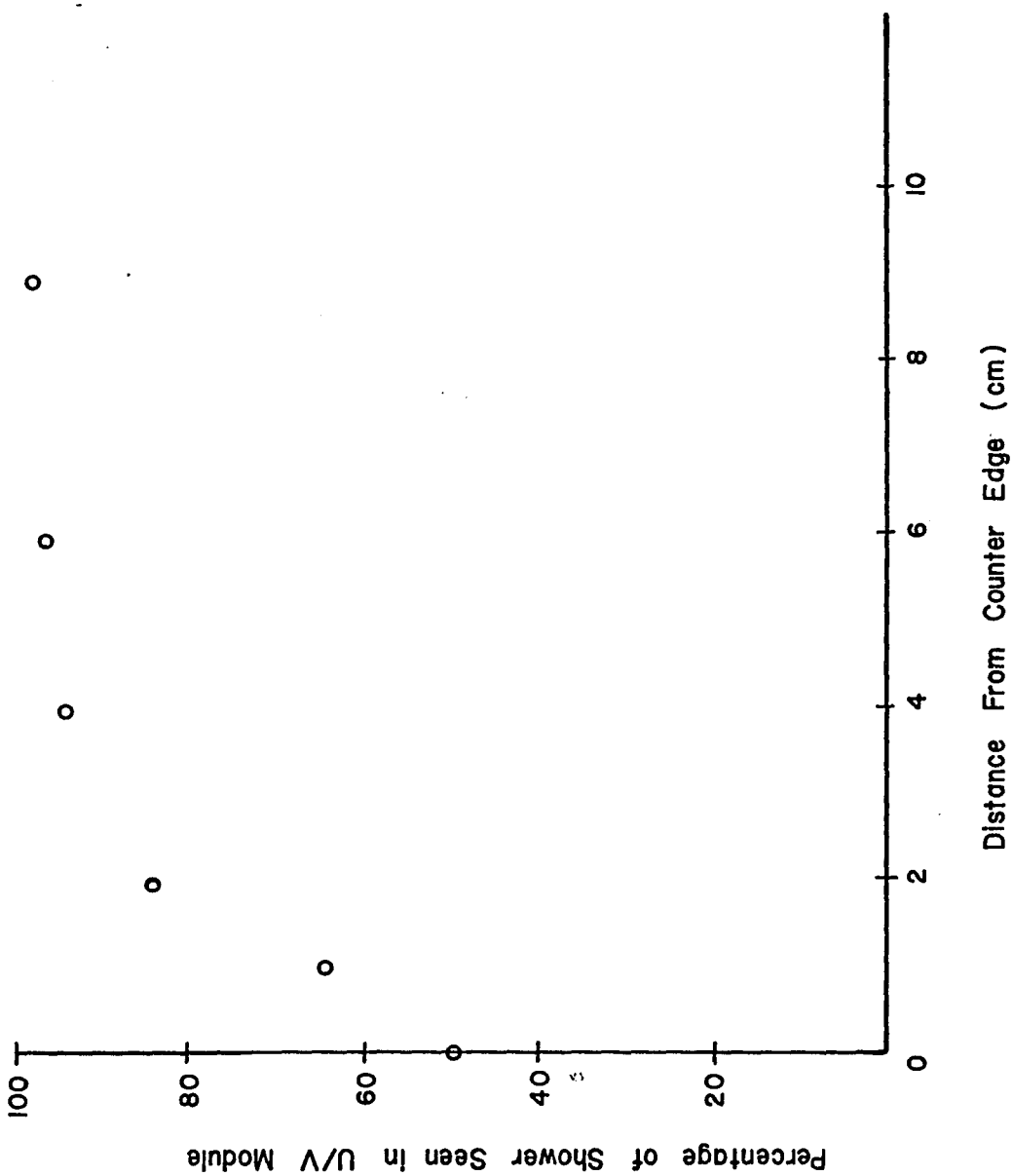

Reproduced with permission of the copyright owner. Further reproduction prohibited without permission.

absorption counters as a function of energy for electrons and tagged photons. The fraction of the shower energy deposition in the U and V counters and their ratio are given in Table B-2 and Figure B-4. As one can see, there is a marked difference between electron- and photon-initiated showers. The depth of shower maximum is greater for photon-initiated showers than for electron-initiated showers of the same energy, which is indicated by the lesser U/V ratio for photon-initiated showers.

To get a value for the energy of a particular shower, one must, of course, add together the pulse heights from the U and V counters. Although the relative gains of the U and V counters are not a function of shower energy, the ratio to add the U and V together to get the minimum error in the energy may be a function of energy. We have measured this effect and find that the ratio is only slowly varying with energy from 1.00 at 15 GeV to .80 at 185 GeV with only a weak effect on the width of the resulting pulse height distributions. To make subsequent shower reconstruction easier, we ignore this effect and simply add the U and V pulse heights together with a ratio of one for all energies.

Figure B-5 shows the raw pulse height distributions for the U and V counters and for the sum (U + V)/2 taken on an event-by-event basis. The individual distributions are quite wide, but, since the U and V pulse heights are highly correlated due to fluctuations in the longitudinal shower

Reproduced with permission of the copyright owner. Further reproduction prohibited without permission.

Table B-2

Fraction of Shower in U and V Counters
as a Function of Energy

a) Electron-Initiated Showers

Energy (GeV)	Fraction of Pulse Height in U	in V	U/V Ratio
15	.81	.19	4.25
30	.72	.28	2.57
60	.66	.34	1.95
90	.62	.38	1.62
135	.57	.43	1.33
185	.51	.49	1.04

b) Photon-Initiated Showers

Energy (GeV)	Fraction of Pulse Height in U	in V	U/V Ratio
56	.56	.44	1.26
67	.55	.45	1.23
78	.54	.46	1.17
87	.53	.47	1.13
91	.53	.47	1.13
96	.52	.48	1.08
99	.52	.48	1.08
104	.51	.49	1.04
109	.50	.50	1.00
113	.48	.52	.93
117	.44	.56	.79

Reproduced with permission of the copyright owner. Further reproduction prohibited without permission.

Figure B-4

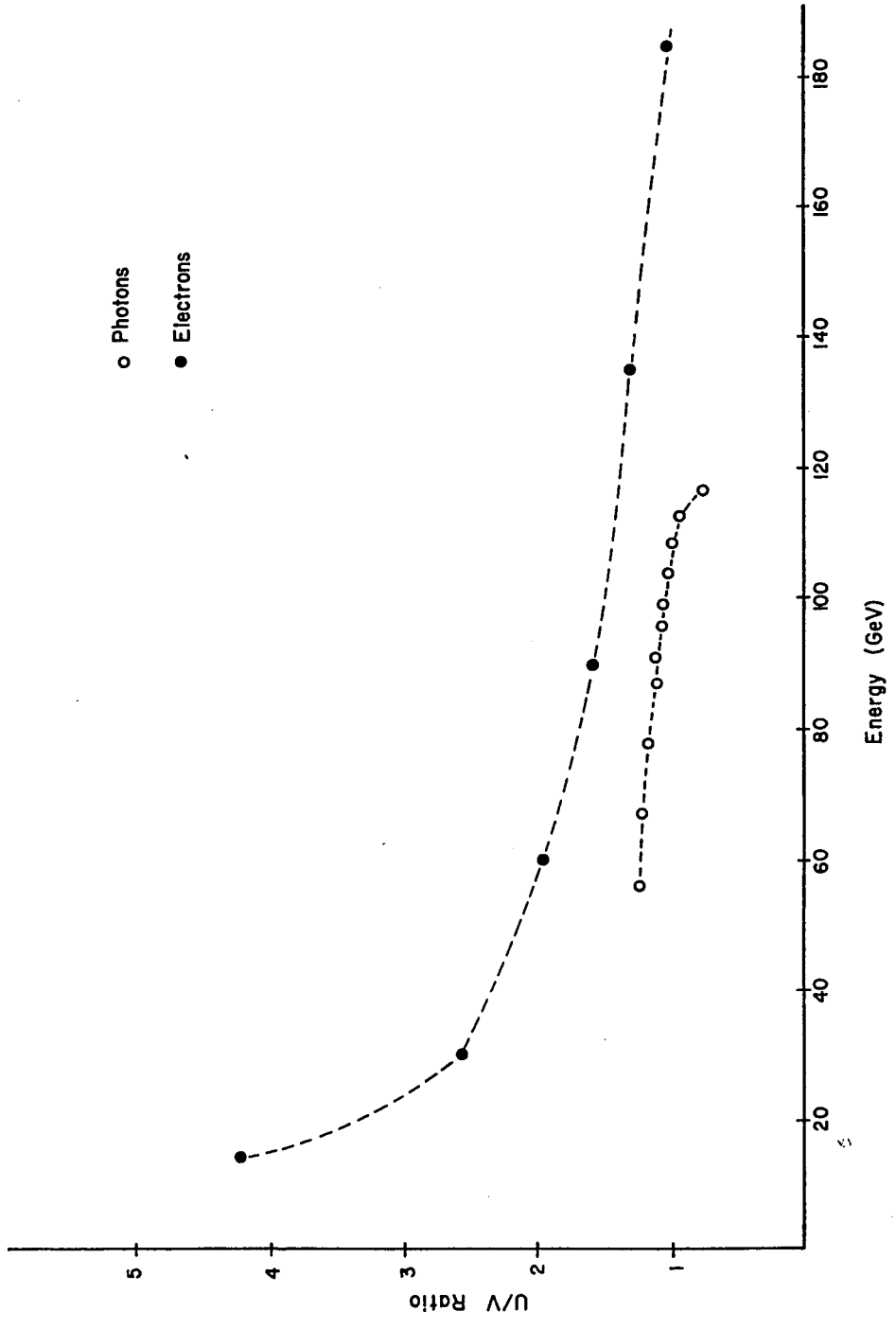

Reproduced with permission of the copyright owner. Further reproduction prohibited without permission.

Figure B-5

Total Absorption Counter Pulse Height Distributions

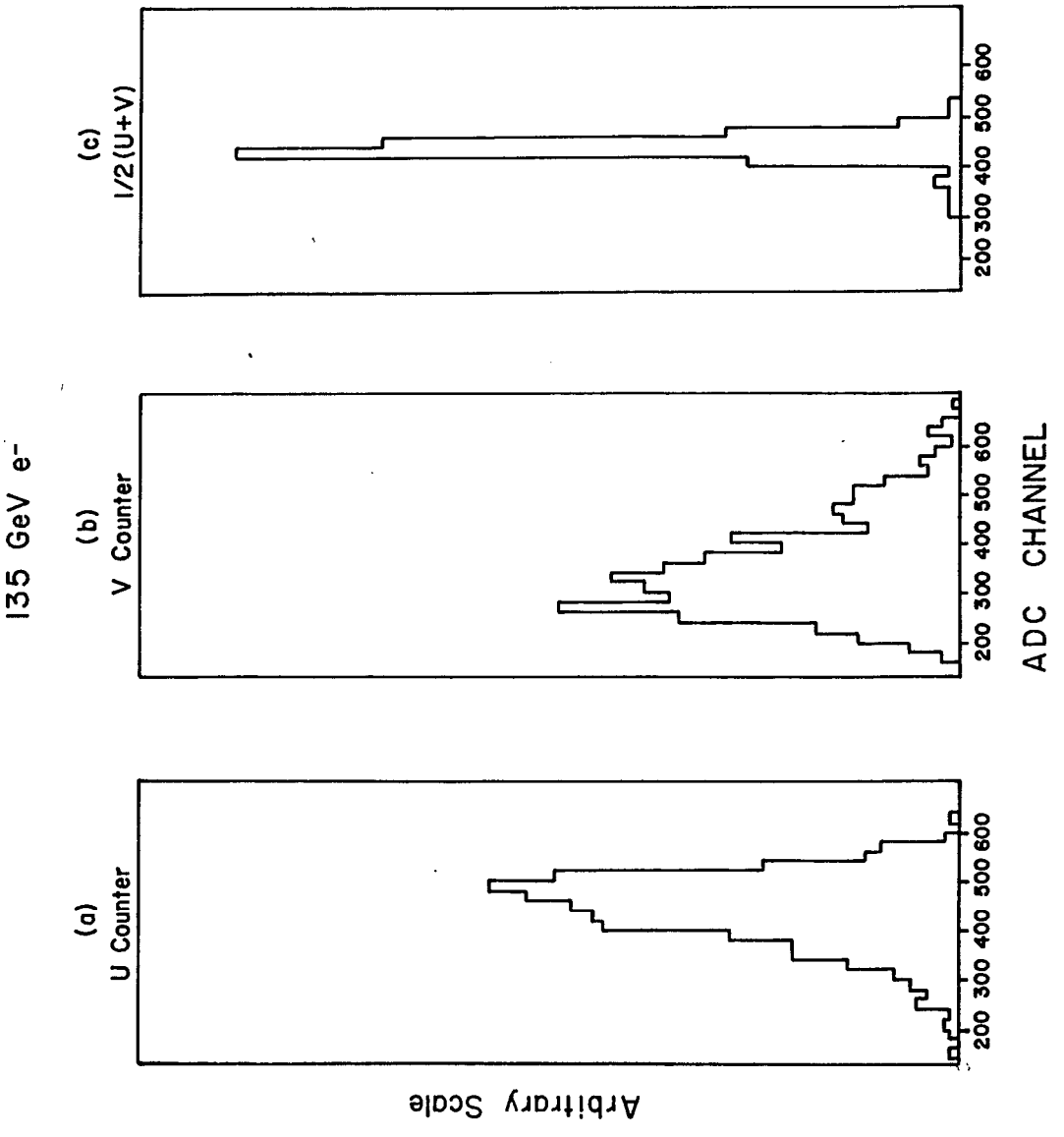

Reproduced with permission of the copyright owner. Further reproduction prohibited without permission.

development, the resulting summed distribution is quite narrow. The large fluctuations in the development of the shower also yield very wide pulse height distributions in the hodoscope as discussed in Section B.3.5.

B.3.4. Energy Dependence and Resolution

Using the data from a set of runs where we varied the electron beam energy from 15 to 185 GeV and a long run with tagged photons using a 135 GeV electron beam, we compiled the data necessary to give the energy dependence and resolution for the total absorption counters and hodoscope. These results are displayed in Figures B-6 and B-7. The energy used for the tagged photon points is the mean energy of the tagging channel.

As can be easily seen, the pulse height from the total absorption counters (U + V) is a linear function of beam energy with the electron and photon points lying on the same curve. The line through the points is the fit

$$PH(E) = 6.01\ (E - 3.0)$$

where E is measured in GeV.

The Gaussian width (σ) of the pulse height distribution which represents the energy resolution of the counters is also shown. Here the curve is just meant to guide the eye and does not represent a fit to any particular function. In this set of measurements no attempt is made to separate out

Reproduced with permission of the copyright owner. Further reproduction prohibited without permission.

Figure B-6

Total Absorption Counter Energy Response and Resolution

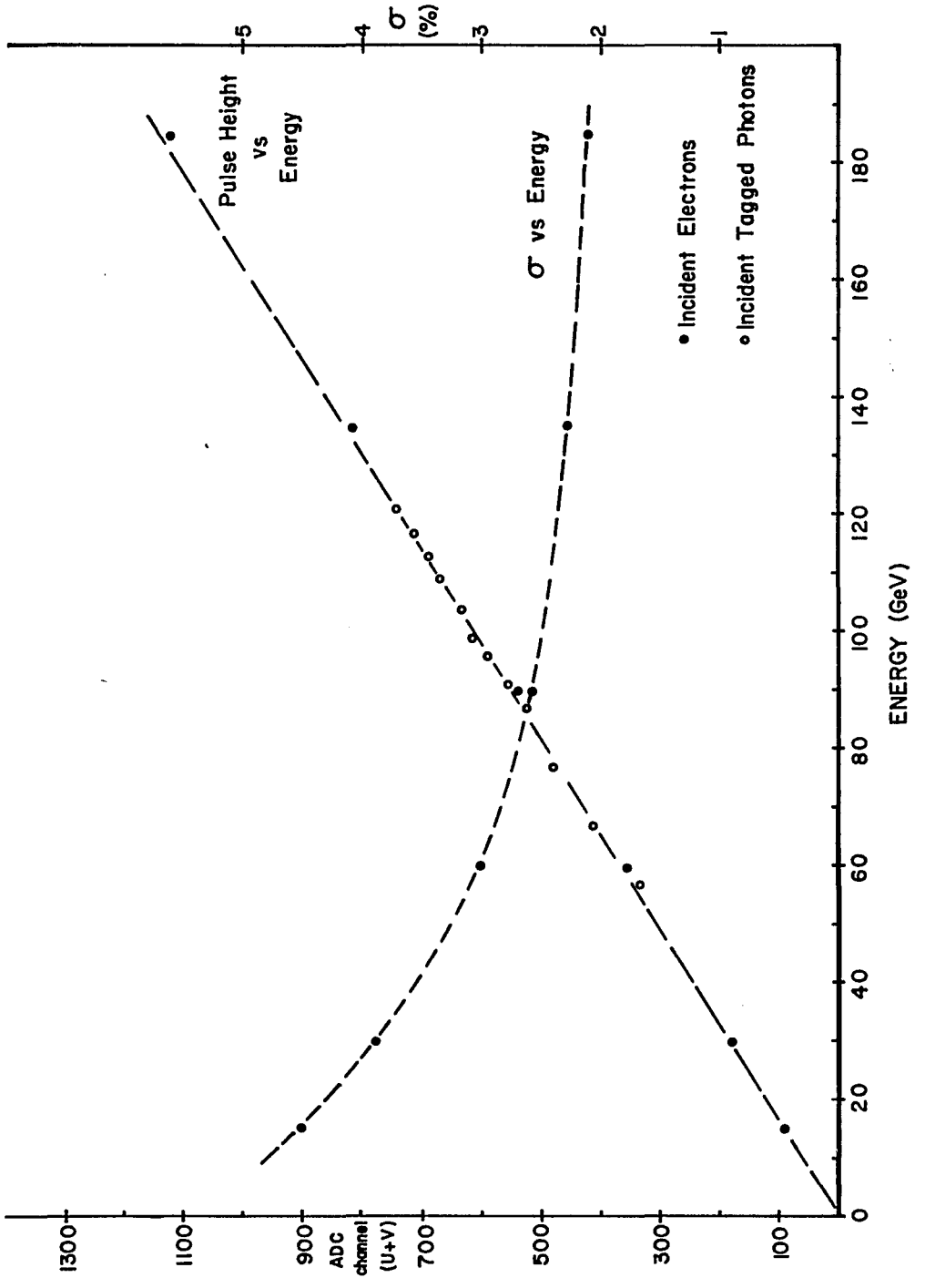

Reproduced with permission of the copyright owner. Further reproduction prohibited without permission.

Figure B-7

Hodoscope Energy Response and Resolution

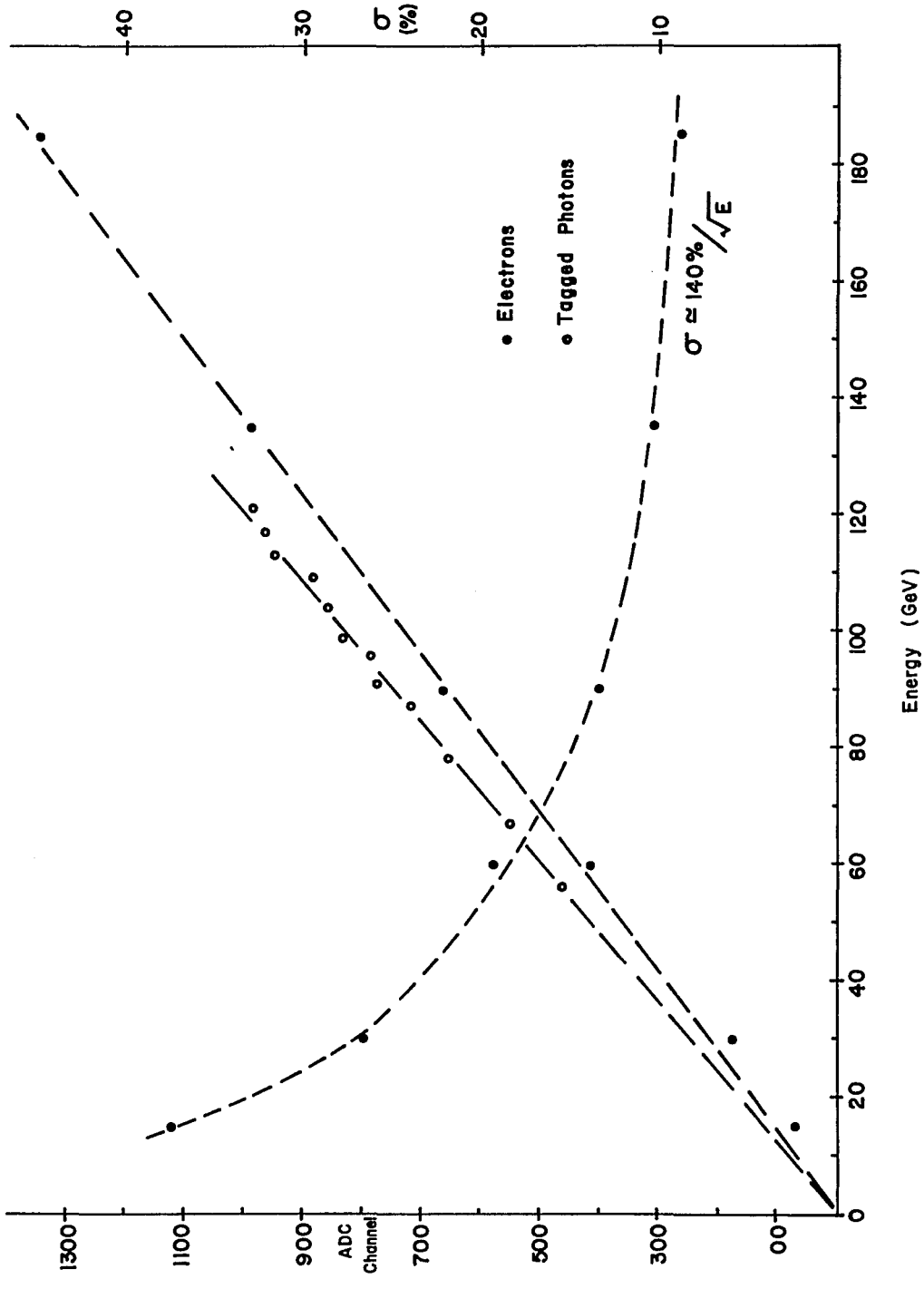

Reproduced with permission of the copyright owner. Further reproduction prohibited without permission.

beam momentum width effects. This is expected to be substantial since the momentum bite is typically 1 to 2% and is dependent on the beam energy. We did one special run with a 135 GeV electron beam with the collimators stopped down such that the beam momentum spread was small with the resulting $\sigma = 1.6\%$. With this as a measure of beam width effects, we can parametrize the energy resolution of the total absorption counters as

$$\sigma(E) = 18\% / \sqrt{E}$$

where E is measured in GeV.

The same information is plotted for one of the hodoscope planes in Figure B-7. The pulse height plotted is the sum of the pulse heights of nine adjacent strips. Again the energy response is approximately linear, although at low energies there is a significant deviation from linearity. This is to be expected since the hodoscope is only sampling at a fixed depth of the shower. Note that the photon- and electron-initiated showers lie on different curves with the photon data higher by about 12%. This agrees well with the previously described results on the U/V ratio for electron- and photon-initiated showers.

The data for the energy resolution of one hodoscope plane is also shown with the curve $\sigma = 140\% / \sqrt{E}$ superimposed. The resolution is poor since the hodoscope samples the shower only once and we have already seen that the longitudinal fluctuations of the shower are large. Since the

Reproduced with permission of the copyright owner. Further reproduction prohibited without permission.

energy measured in one plane of the hodoscope is strongly correlated to that measured in the other plane, even this poor resolution allows us to solve certain multi-shower ambiguity problems. This is discussed more thoroughly in the main text of this thesis.

B.3.5. Shower Width and Position Resolution

As was mentioned previously, showers are quite wide in the hodoscope due to the lateral spreading of the soft component. This is illustrated in Figure B-8 where various distributions are shown for 30 and 135 GeV showers. Figure B-8a shows a typical pulse height distribution for one event. Note that the distribution is non-Gaussian with most of the pulse height in the central three strips, especially at the higher energy. Figure B-8b is a histogram of the sum of the pulse heights of nine strips. The resulting mean and width of these distributions give the results plotted in Figure B-7. As a quantitative measure of the location and width of the shower, we define the centroid, $\langle x \rangle$, and mean square width, $\langle \Delta x^2 \rangle$, to be

$$\langle x \rangle = \frac{\Sigma\, x_i\, PH_i}{\Sigma\, PH_i}$$

$$\langle \Delta x^2 \rangle = \frac{\Sigma\, (x_i - \langle x \rangle)^2\, PH_i}{\Sigma\, PH_i}$$

The shower width, W, is defined as $W = \sqrt{\langle \Delta x^2 \rangle}$

Reproduced with permission of the copyright owner. Further reproduction prohibited without permission.

Figure B-8

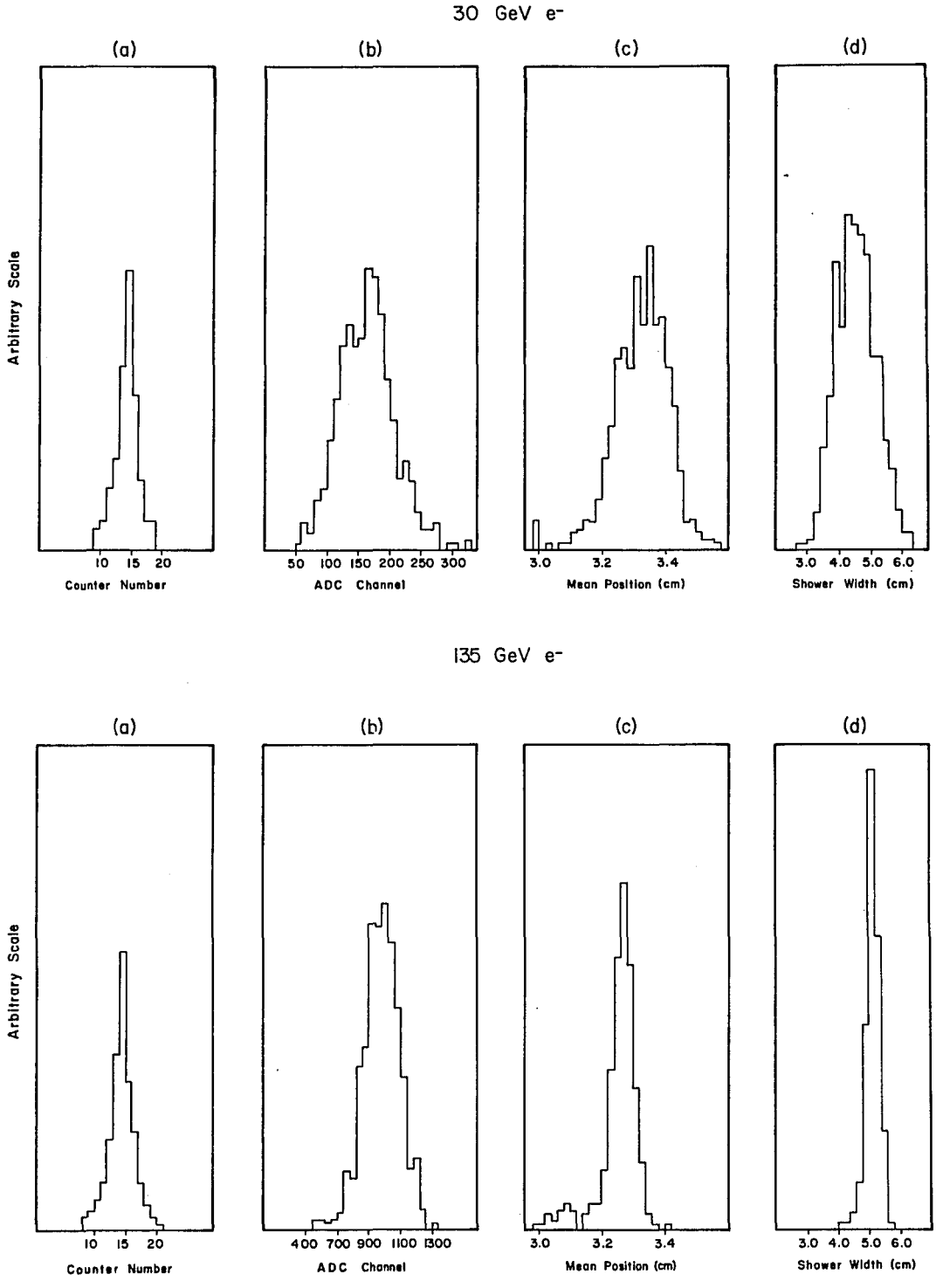

Reproduced with permission of the copyright owner. Further reproduction prohibited without permission.

Figures B-8c and B-8d are histograms of the quantities $\langle x \rangle$ and W. The Gaussian widths of these distributions define the position resolution, $\sigma_{\langle x \rangle}$, and variation in shower width, σ_W, respectively. Table B-3 lists these quantities as a function of energy for electron-initiated showers in the 15 to 185 GeV range. Note that the position resolution is in the 2 to 3 mm range at the highest energies.

Reproduced with permission of the copyright owner. Further reproduction prohibited without permission.

Table B-3

Shower Width and Position Resolution
In the Hodoscope

Energy (GeV)	Shower Width W (cm)	Variation in Width (cm)	Position Resolution (cm)
15	4.66	1.06	1.48
30	4.85	.55	.75
60	4.99	.35	.43
90	5.04	.27	.32
135	5.14	.23	.26
185	5.21	.20	.20

Reproduced with permission of the copyright owner. Further reproduction prohibited without permission.

Appendix C

ON-LINE MONITORING SYSTEMS

C.1. General Requirements

Since a knowledge of the integrity and stability of the experimental apparatus during the data taking is essential to this experiment, we designed a number of monitoring systems to check the status of the various counters as the data is being collected. The requirements of the various monitors are that they must be reliable, stable, and allow for redundancy. In addition the overall system should be completely automated, but still allow the flexibility to manually override the computer so that a particular monitor may be looked at in greater detail at any given time. For the forward detector, the crucial quantity to monitor is the variation of the pulse height with time. For the total absorption counters, we have an energy resolution of about 2% (Gaussian standard deviation) for 100 GeV showers. Thus we require a knowledge of the gain to better than 2% in order to keep systematic errors within this resolution. To provide for this accuracy as well as the necessary redundancy, we have three separate systems to monitor the pulse height of the counters using light emitting diodes (LED's), americium-241 sources embedded in sodium iodide crystals, and muons from the beam halo. For the hodoscope counters, the requirements are not as severe since the pulse height

Reproduced with permission of the copyright owner. Further reproduction prohibited without permission.

information need not be known to this precision (σ = 10% is sufficient), thus we have only a combined and somewhat less redundant LED and americium source system. In the recoil detector, the drift chambers do not lend themselves to these sorts of monitors; however, for the time-of-flight counters, checks on the stability of the pulse height and the time spectra are useful and can be performed with an LED system. In addition we have a system to monitor all the high voltages on the phototubes and drift chambers, the temperature at various places in the hydrogen target, and the currents on a couple of critical magnets (including the tagging magnets). This system, provided by Fermilab, consists of a high voltage distribution and monitoring box, multiplexer, digital voltmeter, and CAMAC readout system. We refer to this collection of units as the DVM system. It is interfaced to the computer so that we can not only read out the voltages on-line, but also write them onto magnetic tape for further study. The DVM system includes an alarm which is set off to notify the person on shift if any values vary from the nominal value by more than a predetermined tolerance. A further description of this system may be found in [Brenner 77].

The bulk of the remainder of this appendix consists of a description and summary of the performance of each of the on-line monitoring systems.

Reproduced with permission of the copyright owner. Further reproduction prohibited without permission.

C.2. LED System for the Total Absorption Counters

As mentioned previously there are three monitoring systems for the total absorption counters [Breakstone 75d]. The purpose of the LED system is to provide an accurate short-term monitor which can be used to cross-calibrate the counters and indicate gain variations that are due to rate effects. It has the advantages over the other systems since it can be turned on and off easily, thus can be run at high rates for short periods of time while still collecting good statistics; it can easily show in-spill and out-of-spill gain changes; it can easily be used to isolate a small set of counters; and its light output can be varied to investigate the linearity of the ADC's, possible phototube saturation, or other effects which may be intensity dependent. It has the limitations that its light output is temperature dependent and that its long term stability is suspect.

Since the light output of showers is quite large and we want to fan out one LED to several counters using fiber optics, we need a very bright LED. We found that the OPCOA LSL-38L-3 Ultra-High Intensity Illuminator is quite suitable. Since its peak light output is in the green part of the spectrum, its spectral response matches that of phototubes better than the more common red LED's. A number of tests of this LED were made to check its suitability for use as a monitor [Breakstone 74c]. In particular in a two-month test, we found its intensity to decrease systematically by

Reproduced with permission of the copyright owner. Further reproduction prohibited without permission.

about 4% per month [Breakstone 76b]. Day-to-day fluctuations are on the 1% level. The temperature dependence is quite large--the intensity decreases with increasing temperature by about 0.5% / ^{o}C [Breakstone 76c]. These variations limit the LED to a short term (on the order of a few days) monitor which will need periodic recalibration using the other monitors which are more stable with time and temperature variations.

The physical components of the LED system are illustrated in Figure C-1. The system is designed such that LED's and fiber optics groups can easily be replaced in the event of a malfunction. The LED is potted with a clear epoxy resin into a metal (aluminum or brass) housing complete with BNC connector soldered to the LED for ease of electrical connection. The metal housing containing the LED screws into a metal housing containing a group of eight fiber optics bundles (DuPont Crofon #1410). A piece of plexiglass in between the LED and the fiber optics is used to diffuse the highly collimated LED light. The fiber optics is coupled to the counter with a PVC housing which screws onto a plexiglass adapter glued to the light pipe of the counter. It is purposely placed such that the light has to go through all of the glue joints in the counter to reach the phototube so that we have a check that the glue joints are not deteriorating during the experiment. All optical couplings use optical grease (Dow Corning Q-2-3067). Neoprene tubing and black tape are used to achieve optical

Reproduced with permission of the copyright owner. Further reproduction prohibited without permission.

Figure C-1

U/V LED Hardware

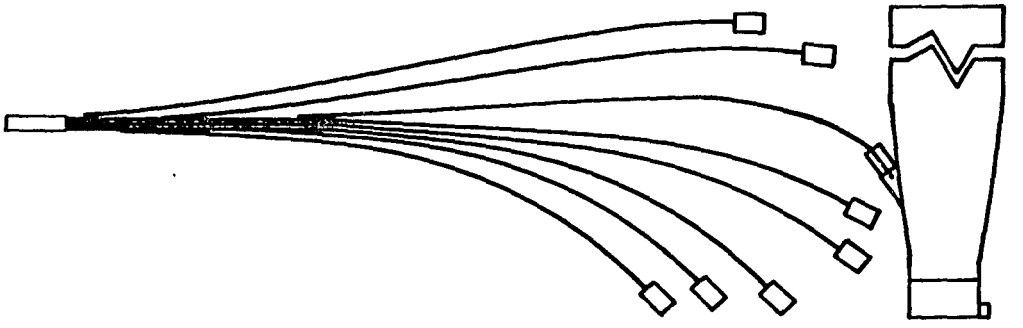

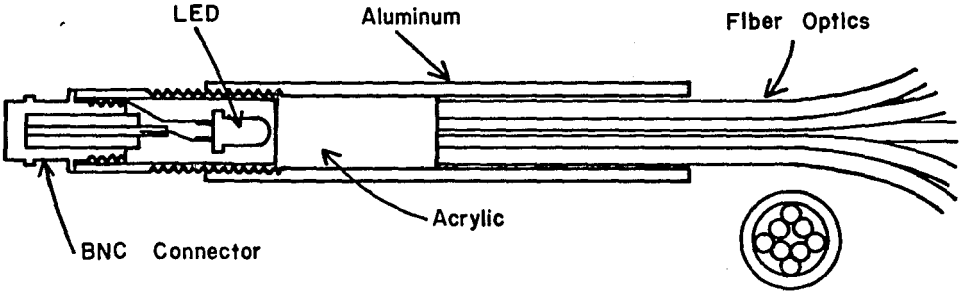

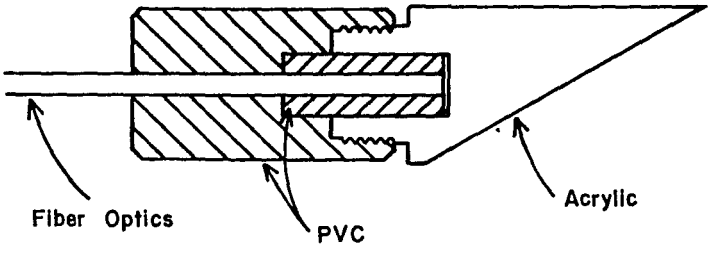

Reproduced with permission of the copyright owner. Further reproduction prohibited without permission.

isolation from the external environment.

To produce the high intensity needed, we use a high voltage pulser (Spencer-Kennedy Laboratories Model 503) modified to allow the use of an external high voltage power supply and a computer-enable gate. We use coaxial relays to switch the high voltage pulse to different LED's. The addressing of these units can be done either by computer via a CAMAC TTL output register or manually using a home-made unit which puts out TTL levels. The entire system was tested for reliability at Santa Cruz during the design stage [Breakstone 76a].

The electrical system used to control the LED's and to produce the trigger is conceptually simple, but somewhat complicated in practice, as illustrated in Figure C-2. The computer chooses the switching matrices which route the pulse to the various LED's via a CAMAC TTL output register. The pulser is enabled by a circuit which allows the computer to turn it on with a NIM pulse from a CAMAC NIM output register. It automatically shuts off with an adjustable delay, usually around two seconds. A small part of the pulse is split off using a resistive splitter to provide the total absorption counter LED trigger (denoted FLED in the drawing) which is used as an input to the priority interrupt to tell the data taking routine what kind of trigger it is.

The entire system worked very well during the course of the experiment. Over a six-month period fluctuations in the

Reproduced with permission of the copyright owner. Further reproduction prohibited without permission.

Figure C-2a

LED Control Electronics Block Diagram

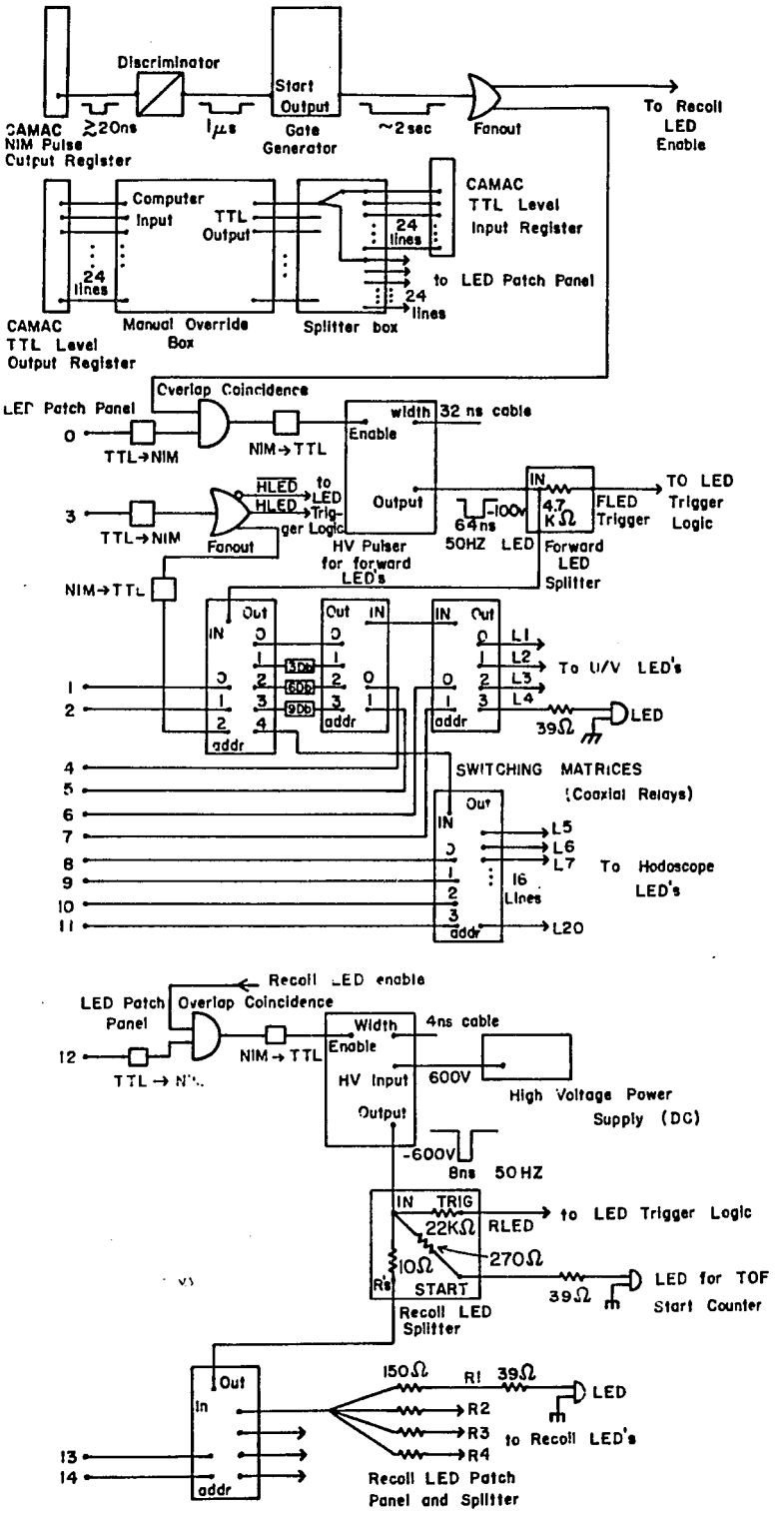

Reproduced with permission of the copyright owner. Further reproduction prohibited without permission.

Figure C-2b

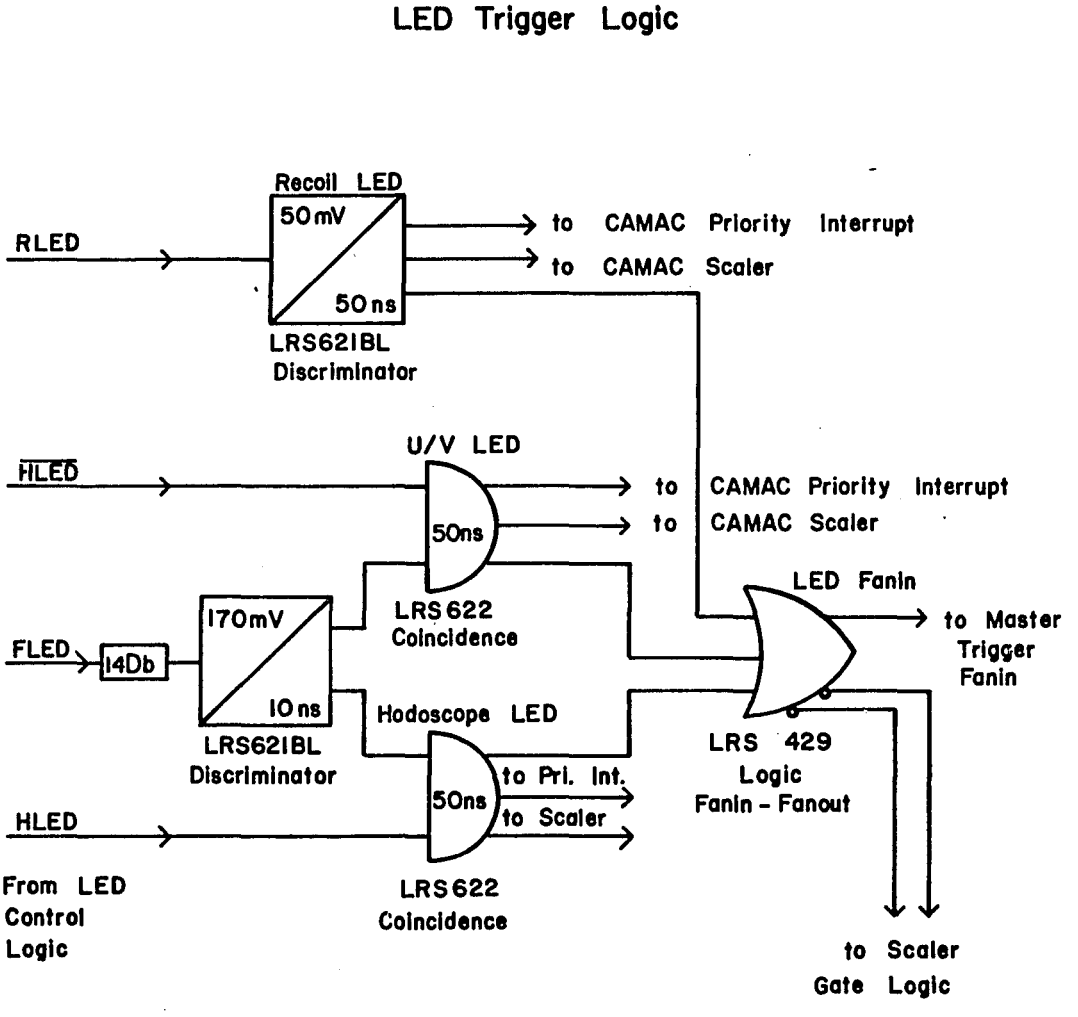

Reproduced with permission of the copyright owner. Further reproduction prohibited without permission.

pulse height are typically on the order of 10%. This is illustrated in Figure C-6, where we have plotted the average pulse height of each of the monitors for the total absorption counters versus time. The point at t = 1 day is the value from the calibration. The error bars include an estimate of the systematic errors in the algorithm which calculates the mean value of the distribution. For the americium, LED, and muon monitors the errors are 2, 1, and 10 ADC counts, respectively. This completely dominates the random errors ($\sigma / \sqrt{N}$) on the calculation of each point. Over a period of a few days the pulse heights for the LED's are constant to a few percent. None of the LED's failed during the experiment.

C.3. Americium Sources for the Total Absorption Counters

The second system used in monitoring the total absorption counters employs an americium-241 source embedded in a thallium-activated sodium iodide crystal. The Am^{241} emits an alpha particle of energy 5.64 MeV, which converts some of its energy into photons in the visible part of the spectrum. For sodium iodide approximately one photon is produced for each 25 eV energy loss. The large light output needed to be comparable to high energy showers requires the use of sodium iodide rather than plastic scintillator. Sodium iodide produces about four times as much light as plastic scintillator for the same amount of energy loss. The sources were manufactured by Isotope Products Laboratory in Burbank,

Reproduced with permission of the copyright owner. Further reproduction prohibited without permission.

California. Since they were a new product, each source was tested in Santa Cruz for its suitability. We found that the sources vary in pulse height by about a factor of two. The widths of the spectra vary by a factor of two and are typically about 2% (Gaussian standard deviation).

Since the primary purpose of the Am^{241} sources is to monitor the gain changes of the phototubes, we mount the sources directly on the face of the tube. In order to allow as much of the light from showers to get to the phototube as possible, we require the sources to be physically small (1/4 inch diameter by 1/4 inch long). For the V counters we mill a hole into the counter into which the source is potted, while for the U counters the sources are glued into a small plexiglass block which is in turn glued to the side of the counter so that the source faces the phototube. The location of the sources is illustrated in Figure A-3 in Appendix A. Optical grease is used for the optical coupling of the source to the phototube.

The logic for producing the americium source trigger for the total absorption counters is shown in Figure C-3. The complexity of the system is due to using many of the same units for a trigger on the total pulse height in the total absorption counters. The dynode signals from all the phototubes are fanned in and amplified downstairs to minimize the number of cables needed to go to the rest of the logic upstairs in the counting room. A factor-of-ten

Reproduced with permission of the copyright owner. Further reproduction prohibited without permission.

Reproduced with permission of the copyright owner. Further reproduction prohibited without permission.

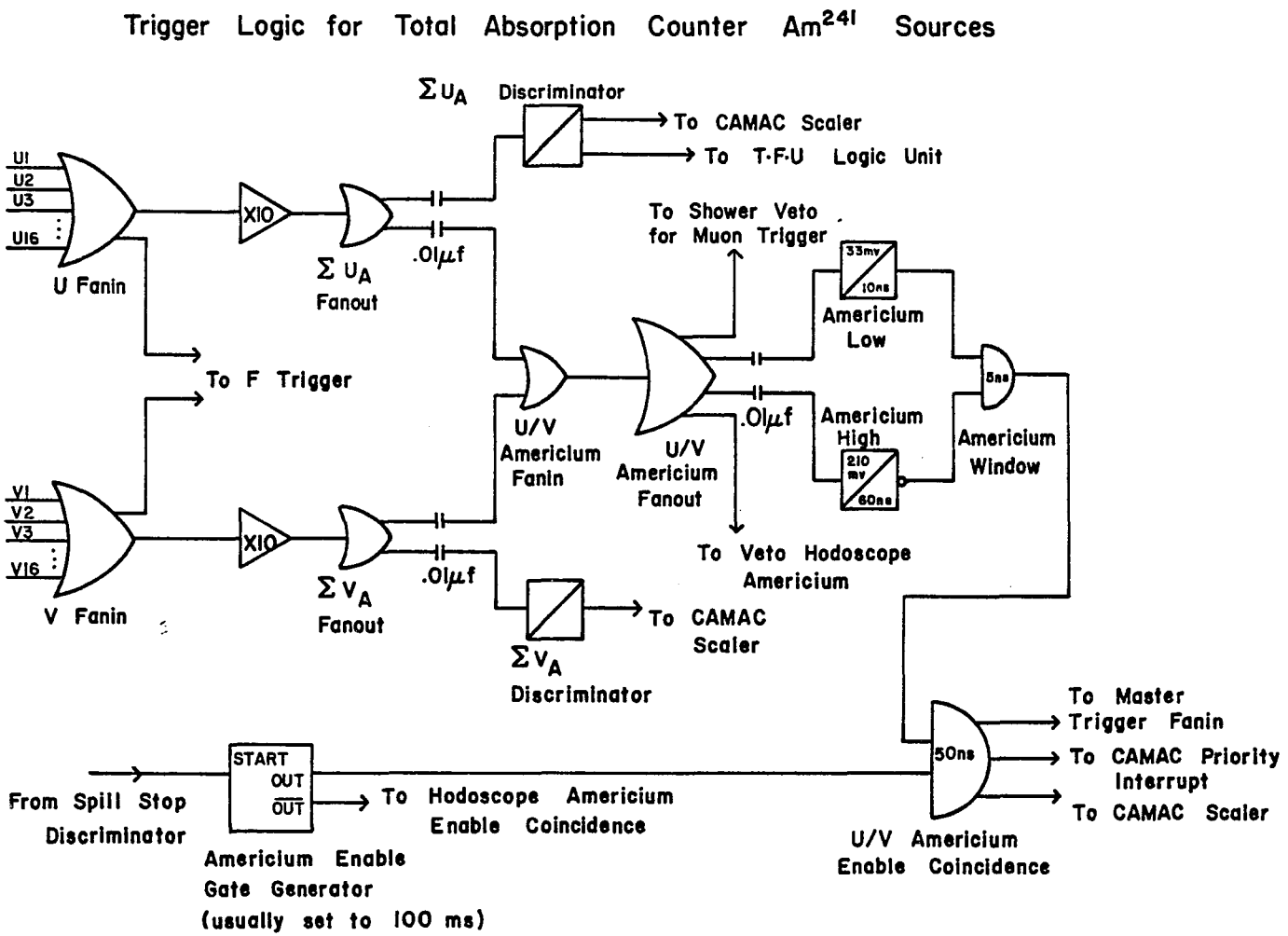

Figure C-3

amplification is used since the typical pulse height from the sources is only about 20 mV, below the discriminator's minimum threshold. Since we do not want showers from real events to contaminate the americium source spectra, we only take americium triggers cut of the beam spill. Figure C-6a shows the pulse height as a function of time for the americium monitor on a typical total absorption counter.

C.4. Muon Monitor

The final monitor of the pulse height stability of the total absorption counters uses muons from the beam halo. The advantage of using muons is that any pulse height variations which are seen must be due to the detection apparatus as opposed to possible variations in the light level of the LED's or americium sources. The major problem with the method is that the pulse height produced by a minimum-ionizing particle passing through the total absorption counters is on the order of 200 times less than that of a 100 GeV shower. This requires the anode signals to be split and one set to be amplified and run into a separate set of ADC's. The amplification is a factor of 100 obtained by putting in series two stages of commercial x10 amplifiers (LRS 612). Also because of the large fluctuations in the low number of photoelectrons produced at the photocathode of the phototubes, the pulse height distributions are quite wide, typically σ = 40%.

Reproduced with permission of the copyright owner. Further reproduction prohibited without permission.

The muon trigger is formed by a coincidence of the muon veto counters used in the tagging system and a set of hodoscope counters in each plane of the forward detector hodoscope as is illustrated in Figure C-4. This forms a set of sixteen 3 cm x 3 cm regions with one region overlapping each of the total absorption counters. The trigger logic consists of a simple set of fanins and coincidence units shown in Figure C-5.

Due to the large width of the pulse height distributions, the muon monitor is somewhat cumbersome to use. Thus the americium sources provide the primary monitor of phototube gain changes. In general when a change in average pulse height occurs, the LED and americium monitors track together, indicating that the gain of the phototube has changed. In those cases the muon monitor is checked in addition to see if it agrees with that hypothesis. This generally does agree and provides an accurate monitor of phototube gain changes in the total absorption counters. A plot of the gain variation as a function of time for a typical phototube as determined by these monitors is shown in Figure C-6d. The error on each point is estimated to be 2%, due primarily to systematic errors in the calculation of the average value for the americium monitor. For most of the counters the gain changes are less than 20% over the course of the experiment with the gain tracking of the monitors good to a few percent. This is discussed further in Section 4.2.3. in the main text.

Reproduced with permission of the copyright owner. Further reproduction prohibited without permission.

Figure C-4

Location of Muon Counters in Hodoscope

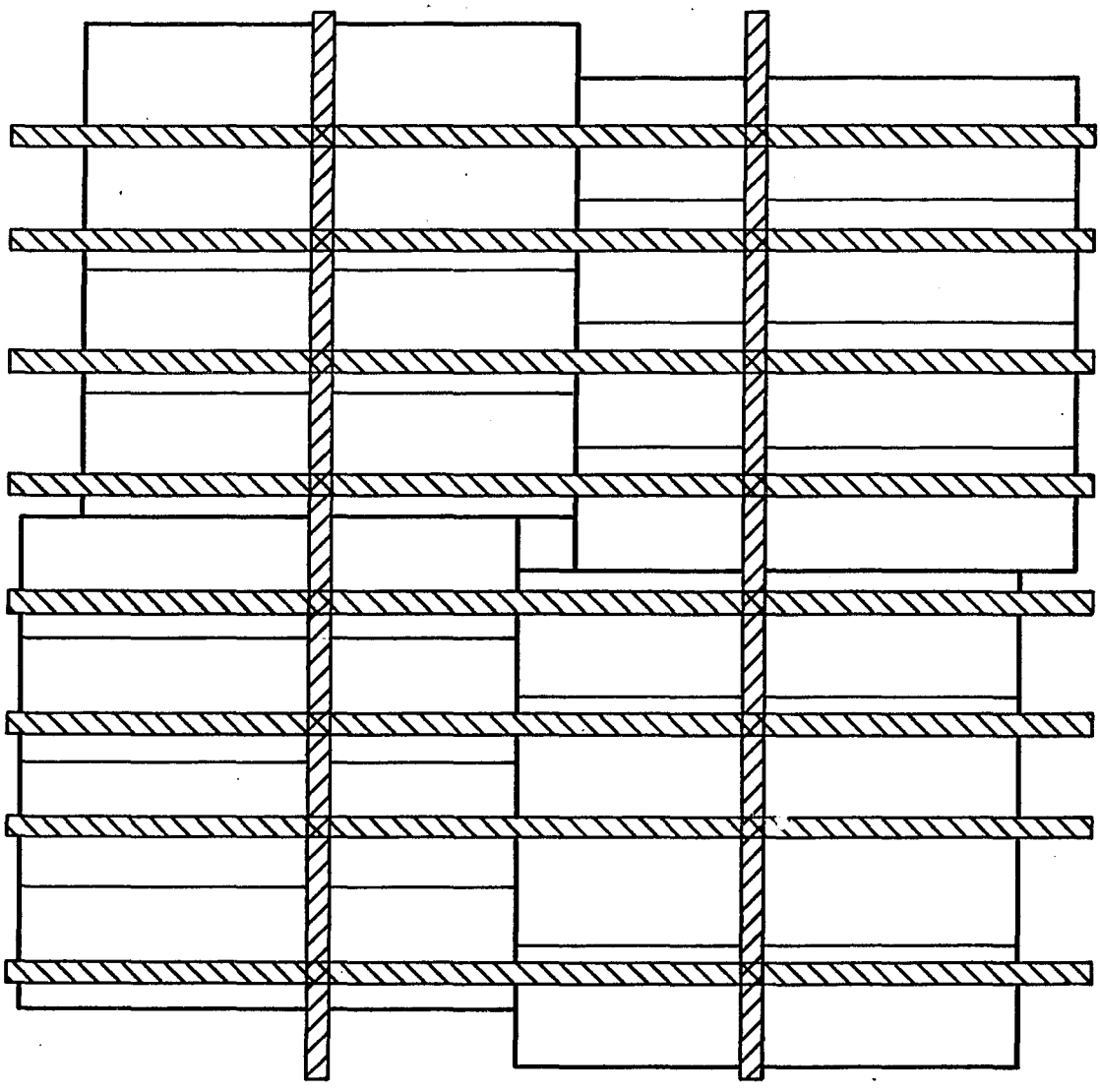

Reproduced with permission of the copyright owner. Further reproduction prohibited without permission.

Reproduced with permission of the copyright owner. Further reproduction prohibited without permission.

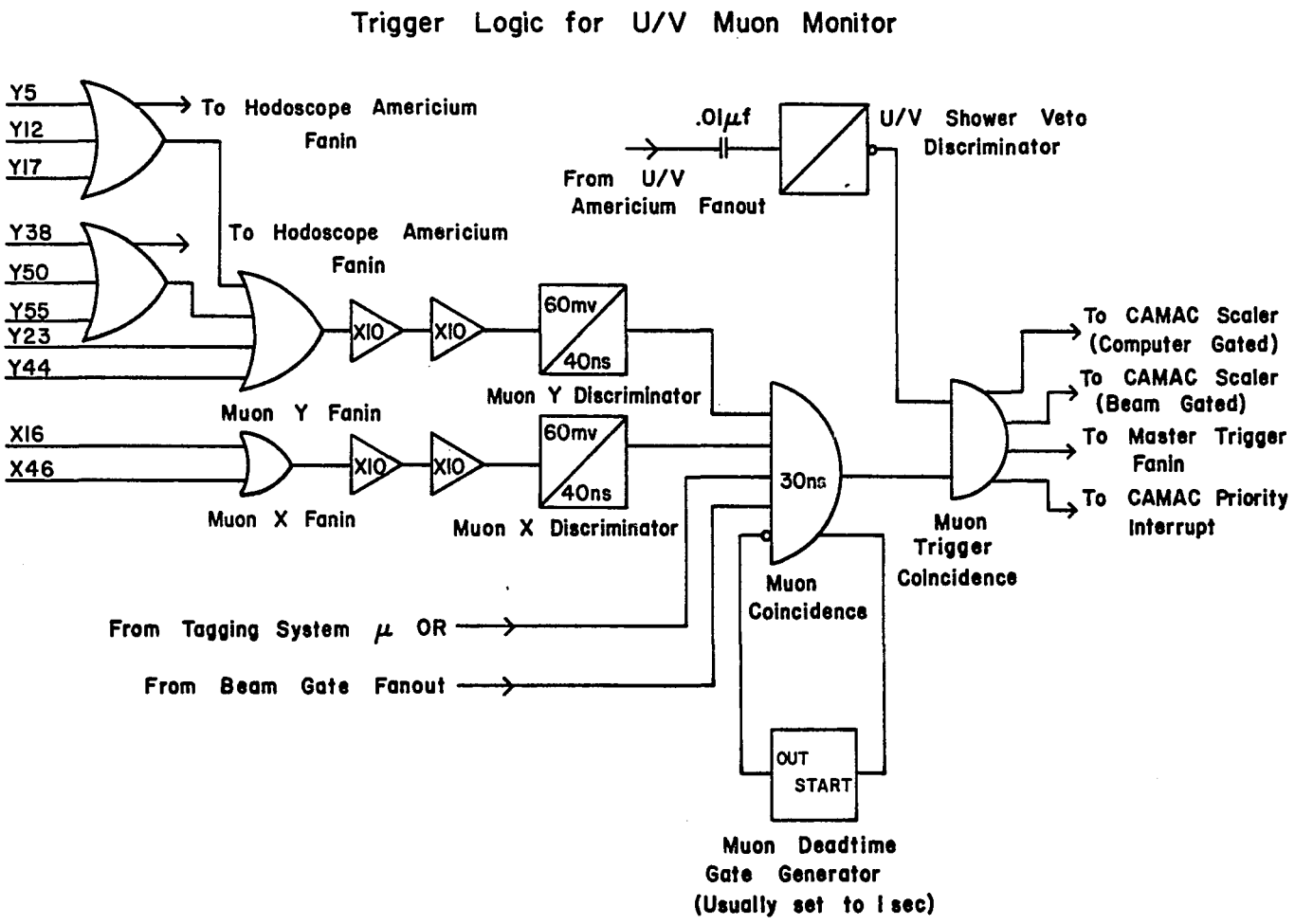

Figure C-5

Figure C-6

Monitors For Total Absorption Counter vs. Time

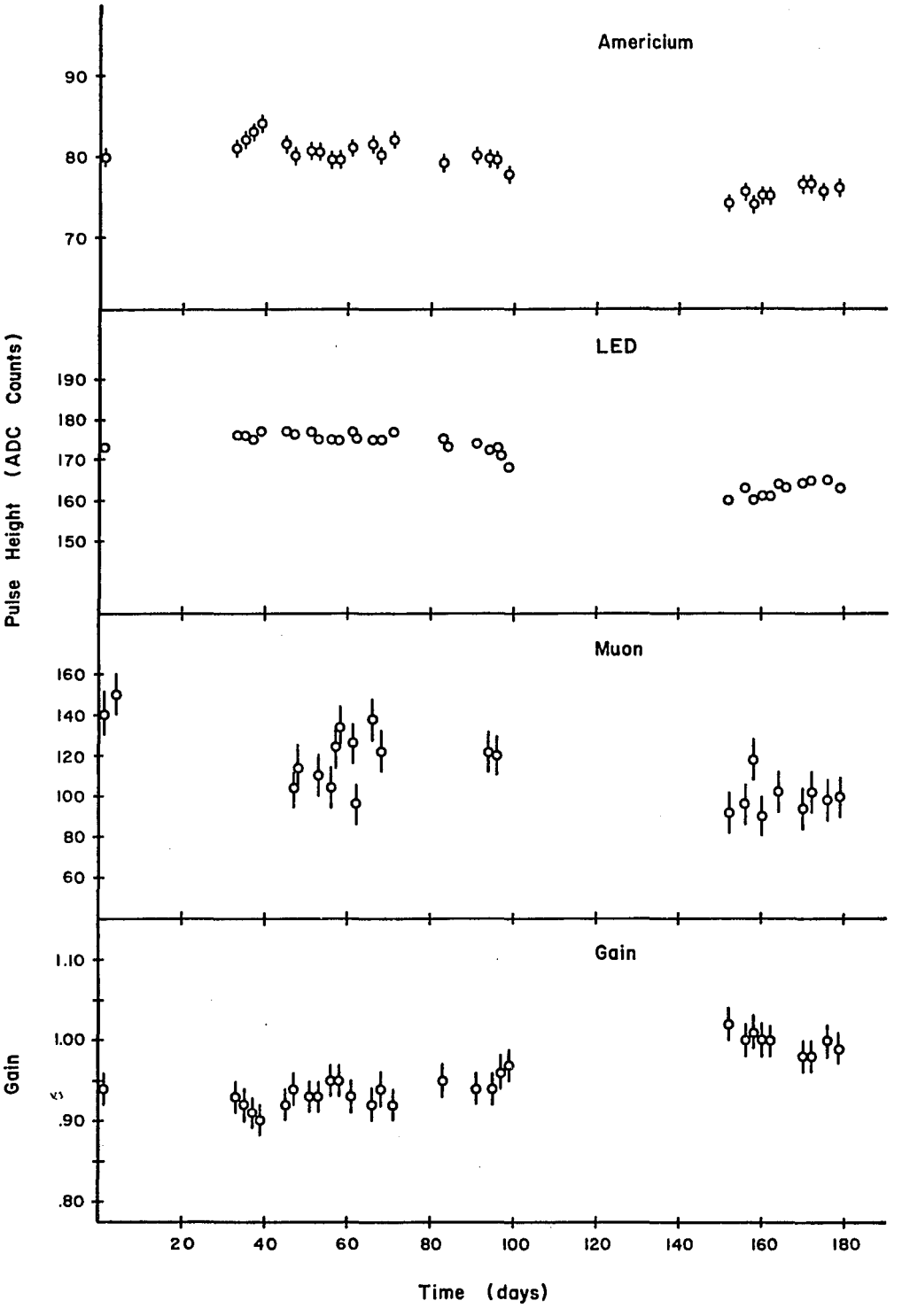

Reproduced with permission of the copyright owner. Further reproduction prohibited without permission.

C.5. LED and Americium Source System for the Hodoscope

For the hodoscope the number of counters involved (112) and the lower precision required allow the use of a combined LED and americium-241 source system. For the outer set of strips, there is one source for each eight counters with a single LED fanned out to that set of eight counters using fiber optics (see Figure C-7). The inner strips are done the same way but with sets of four counters rather than eight. This sums to a total of sixteen sources and sixteen LED's. The same LED and LED-to-fiber optics coupling is used here as on the total absorption counters. Since the light levels in the hodoscope are much less than those in the total absorption counters, the americium sources are embedded in a plastic scintillator rather than sodium iodide. The sources, also manufactured by Isotope Products Laboratories, are potted into a hole milled into the circular "cookie" which connects the counter to the phototube such that the source is directly on the face of the tube. Optical grease provides the optical coupling between the source and the phototube. Unfortunately, due to the timing of testing of prototypes and the ordering of the hodoscope and the sources, we found subsequently that the light levels of the sources are too low by a factor of ten to provide a good monitor, so we had to split and amplify the signals from those phototubes which have the sources on them using commercial amplifiers (LRS 612). This yields a somewhat broad distribution (σ = 40%) which results in many of the

Reproduced with permission of the copyright owner. Further reproduction prohibited without permission.

Figure C-7

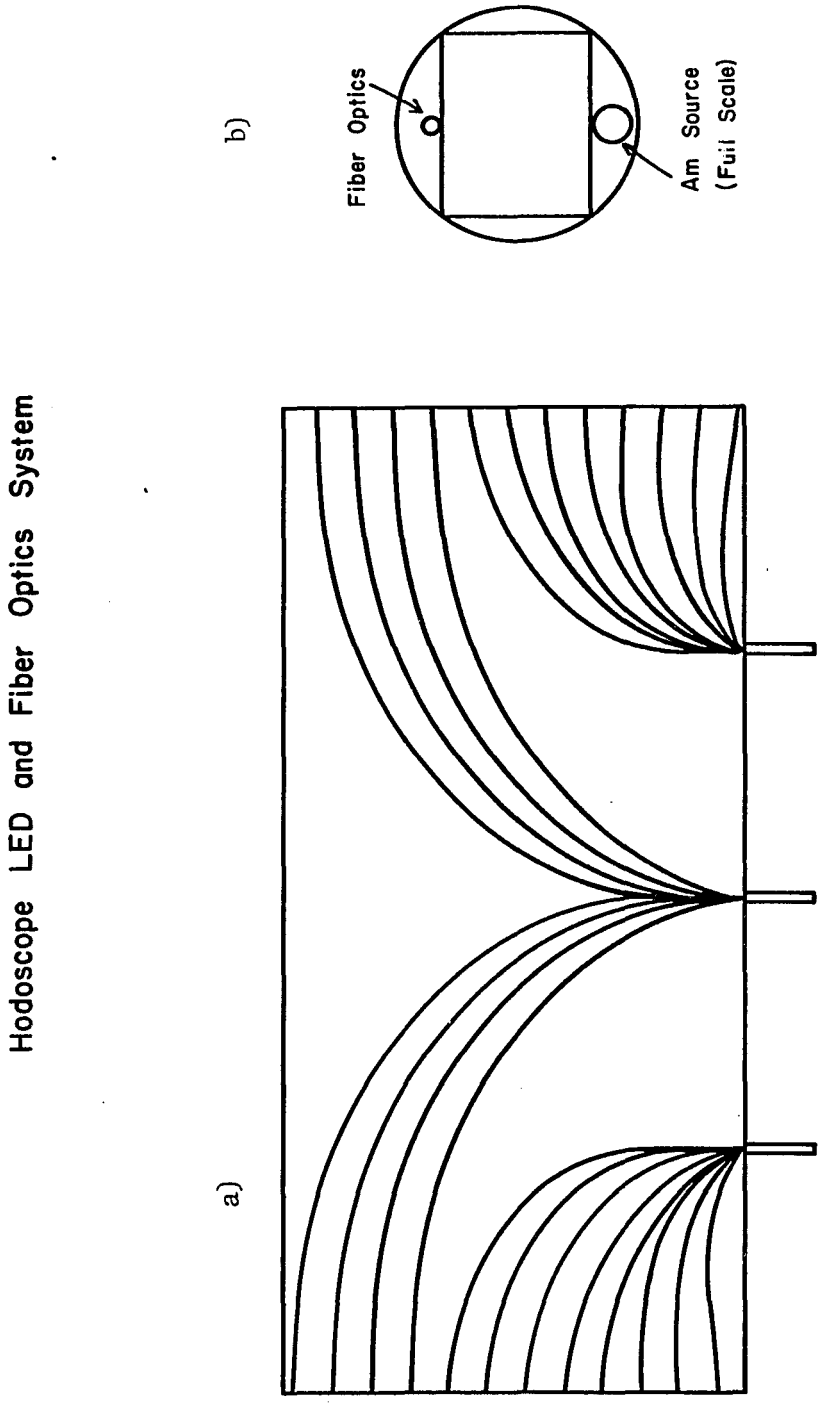

Reproduced with permission of the copyright owner. Further reproduction prohibited without permission.

same difficulties as the muon monitor for the total absorption counters. The trigger logic for each component of this monitoring system is similar to those used for the total absorption counters (see Figures C-8 and C-2).

In general this monitoring system did not do as well as that for the total absorption counters as can be seen in Figure C-9, where we plot versus time the americium and LED monitors for one of the hodoscope counters which had both. The scatter of points for the americium monitor limits its usefulness. The LED's also have larger systematic variations than for those on the total absorption counters. Tracking between the two monitors is not very good in addition. However, the monitors do indicate that the gains are constant to the 10% level for the duration of the experiment.

C.6. Time-of-Flight LED System

For the recoil detector, the only on-line monitoring system is an LED system designed to check the stability of the time spectra of the TDC's and the pulse height spectra of the ADC's for the time-of-flight counters. The major problem in designing the system is that typically inexpensive LED's have risetimes on the order of 50 ns, whereas we hope to achieve a width of the TDC spectrum comparable to the expected resolution of 300 ps. This requires the use of a very short (approximately 1 ns) pulse of quite high vol-

Reproduced with permission of the copyright owner. Further reproduction prohibited without permission.

Reproduced with permission of the copyright owner. Further reproduction prohibited without permission.

Trigger Logic for Hodoscope Am^{241} Source

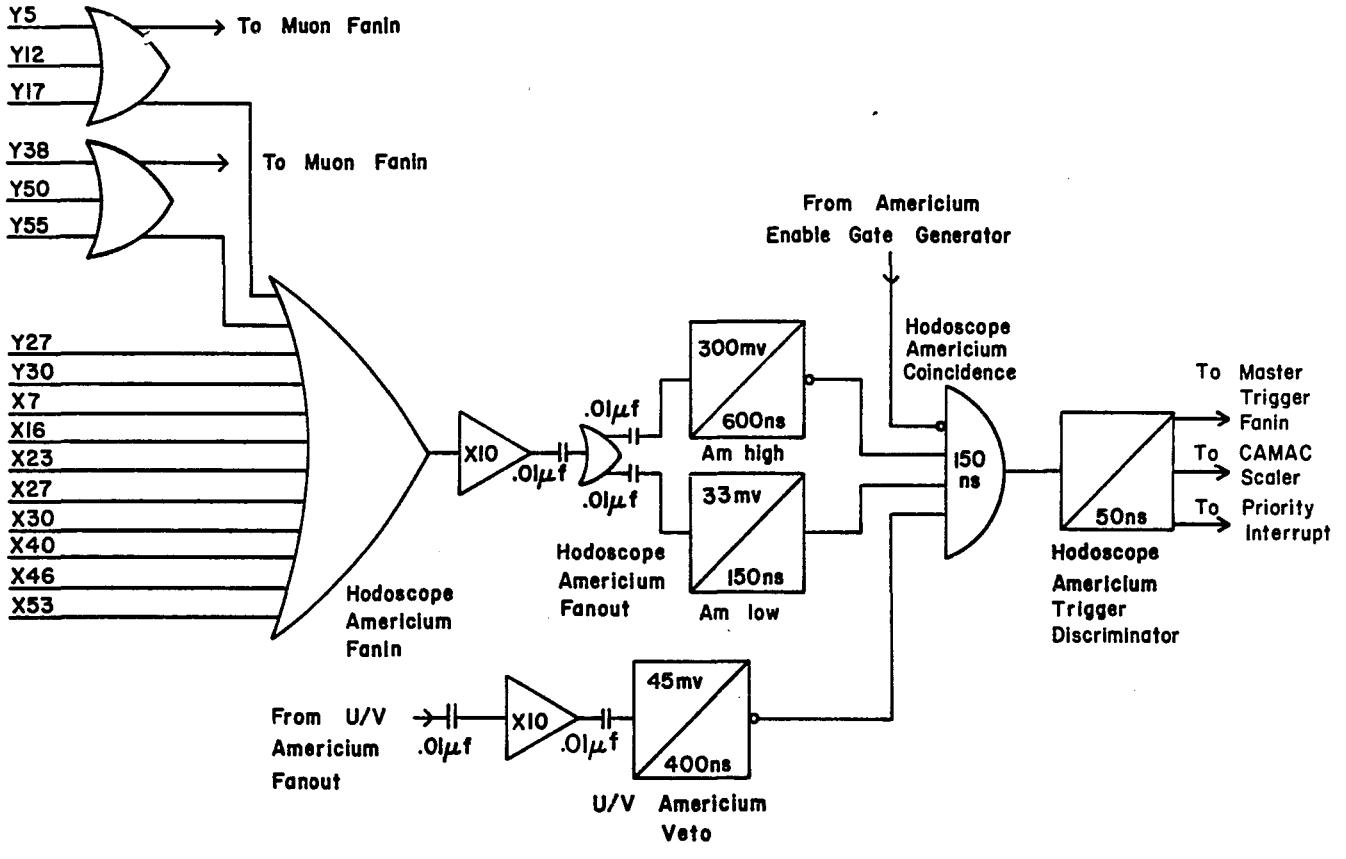

Figure C-8

Figure C-9

Monitors For Hodoscope vs. Time

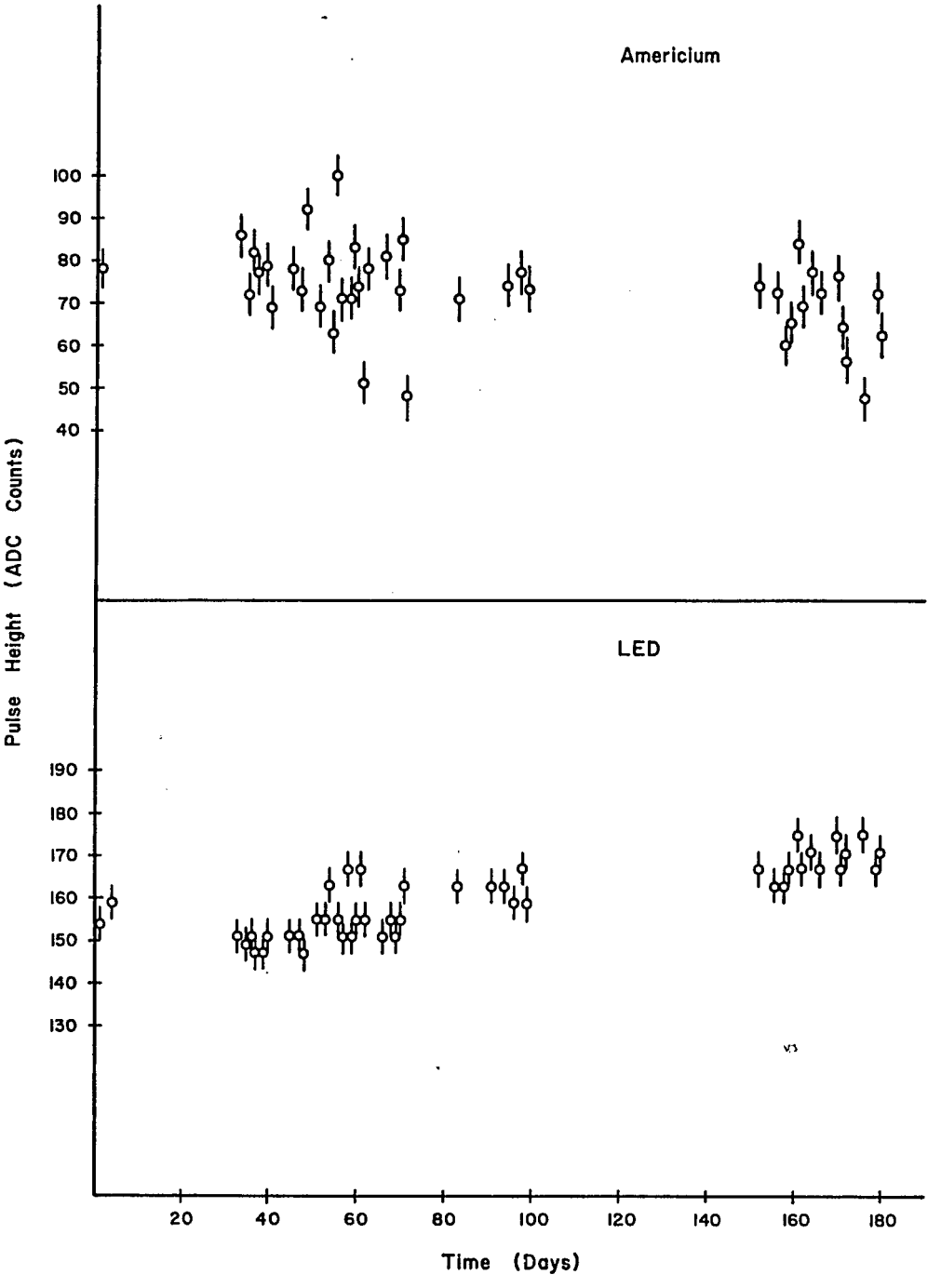

Reproduced with permission of the copyright owner. Further reproduction prohibited without permission.

tage (about 600 V) into a bright LED. For this reason we use the same LED as for the hodoscope and total absorption counters, the OPCOA LSL-38L-3. Tests at Santa Cruz showed the feasibility of this system and achieved a time resolution of = 500 ps, but indicated that the light level of the LED would be marginal, about equivalent to a minimum ionizing particle passing through the counter [Breakstone 76d].

Since we want to illuminate both tubes on either end of the counter with one LED, we designed a mounting which includes the fiber optics light guiding system shown in Figure C-10. The LED's are potted into the same kind of housing as used for the forward detector, however, a separate LED is used for each counter.

The electrical switching system and trigger logic are similar to that of the forward detector. The TOF start counter's LED and one of four sets of four TOF counter LED's are switched on at one time. The pattern of LED's on is such that all the TDC and ADC channels for the time-of-flight system are tested for each pattern. Details on the performance of this system during the experiment may be found in [Grillo 80].

Reproduced with permission of the copyright owner. Further reproduction prohibited without permission.

Figure C-10

TOF LED Hardware

Cutaway View
(Full Scale)

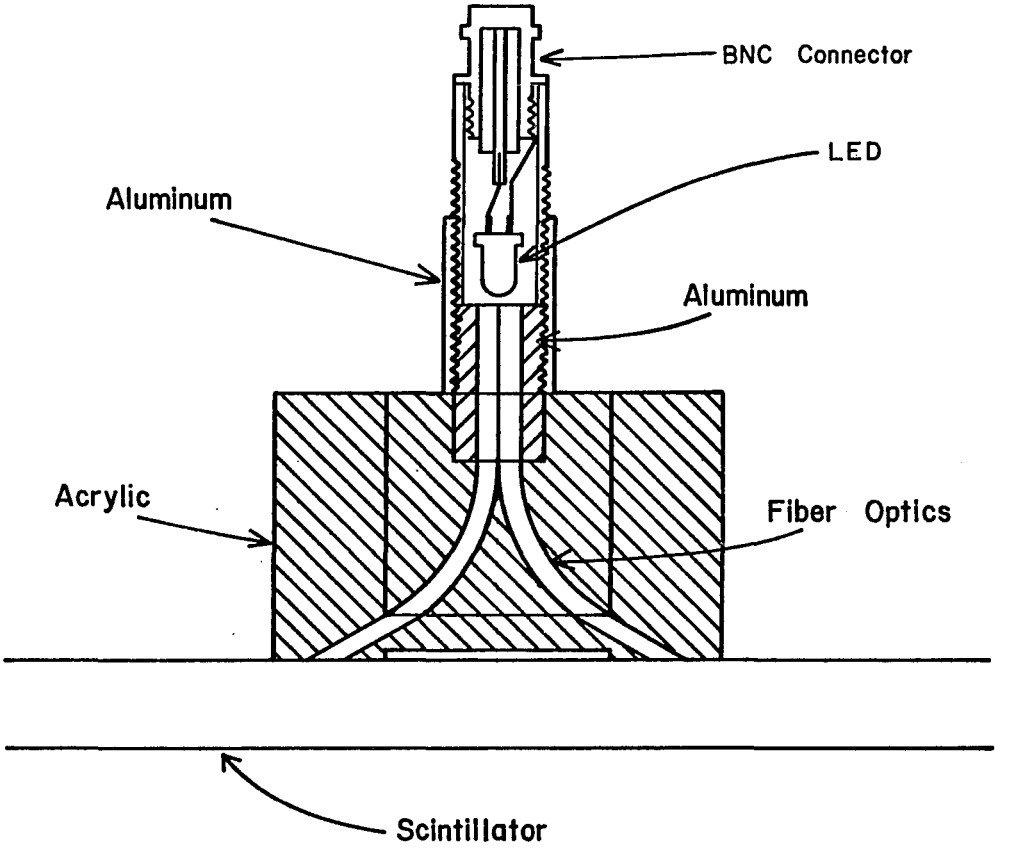

Reproduced with permission of the copyright owner. Further reproduction prohibited without permission.

Appendix D

DERIVATION OF FORMULAS

I have used a number of equations relating shower widths, particle separations, mass formulas, etc. in the analysis of the data. In this appendix I go through the derivations of these formulas in some detail. It is of particular importance to note where approximations are used in each case so that the validity of the formulas may be judged properly.

D.1. Overlapping Hodoscope Clusters

Given two hodoscope clusters that are well separated in one plane (e.g. the y plane), but overlap in the other plane (e.g. the x plane), we know (i.e. have measured) the individual energies, mean positions, and widths in the y plane, E_{1y}, E_{2y}, $\bar{y}_1$, $\bar{y}_2$, σ_{y1}, σ_{y2}, and the combined quantities in the x plane E_x, x, σ_x. We want to know these quantities for individual showers in the x plane, i.e. we want to know E_2, E_1, $\bar{x}_1$, $\bar{x}_2$, σ_{x1}, and σ_{x2}. To relate the unknown quantities to the known ones, we must assume that

$$E_{1x} = E_{1y} \equiv E_1 \qquad E_{2x} = E_{2y} \equiv E_2$$

and

$$\sigma_{x1} = \sigma_{y1} \equiv \sigma_1 \qquad \sigma_{x2} = \sigma_{y2} \equiv \sigma_2$$

and use the following equations:

Reproduced with permission of the copyright owner. Further reproduction prohibited without permission.

(1) $E_{1x} + E_{2x} = E_x$

(2) $E_{1x}\,\bar{x}_1 + E_{2x}\,\bar{x}_2 = E_x\,\bar{x}$

(3) $E_{1x}\,\overline{x_1^2} + E_{2x}\,\overline{x_2^2} = E_x\,\overline{x^2}$

(4) $\sigma_x^2 = \overline{x^2} - \bar{x}^2$

Equations (1) through (3) follow from the definitions of the total energy and first and second moments, e.g. for the first moment

$$\bar{x} \equiv \frac{\Sigma\, x_i E_{ix}}{\Sigma\, E_{ix}}$$

where the sum runs over the N hodoscope strips in which the shower deposits energy. Equation (4) follows from the definition of the shower width squared

$$\sigma_x^2 \equiv \frac{\Sigma\, (x_i-\bar{x})^2\, E_{ix}}{\Sigma\, E_{ix}}$$

Equations (1) through (4) can be used to derive a very useful formula relating the shower widths as follows:

$$\begin{aligned} E_x\sigma_x^2 &= E_x(\overline{x^2}-\bar{x}^2) \\ &= E_x\overline{x^2} - E_x\bar{x}^2 \\ &= E_{1x}\overline{x_1^2}+E_{2x}\overline{x_2^2} - \frac{1}{E_x}(E_{1x}^2\bar{x}_1^2+2E_{1x}E_{2x}\bar{x}_1\bar{x}_2+E_{2x}^2\bar{x}_2^2) \end{aligned}$$

$$\begin{aligned} E_x^2\sigma_x^2 &= E_xE_{1x}\overline{x_1^2}+E_xE_{2x}\overline{x_2^2}-E_{1x}^2\bar{x}_1^2-2E_{1x}E_{2x}\bar{x}_1\bar{x}_2-E_{2x}^2\bar{x}_2^2 \\ &= E_{1x}^2(\overline{x_1^2}-\bar{x}_1^2) + E_{2x}^2(\overline{x_2^2}-\bar{x}_2^2) + E_{1x}E_{2x}(\bar{x}_1^2-2\bar{x}_1\bar{x}_2+\bar{x}_2^2) \\ &= E_{1x}^2\sigma_{1x}^2 + E_{2x}^2\sigma_{2x}^2 + E_{1x}E_{2x}(\sigma_{1x}^2+\bar{x}_1^2-2\bar{x}_1\bar{x}_2+\sigma_{2x}^2+\bar{x}_2^2) \end{aligned}$$

Reproduced with permission of the copyright owner. Further reproduction prohibited without permission.

$$E_x{}^2\sigma_x{}^2 = E_{1x}(E_{1x}+E_{2x})\sigma_{1x}^2+E_{2x}(E_{1x}+E_{2x})\sigma_{2x}^2+E_{1x}E_{2x}(\bar{x}_1{}^2-2\bar{x}_1\bar{x}_2+\bar{x}_2{}^2)$$

$$= E_xE_{1x}\sigma_{1x}^2 + E_xE_{2x}\sigma_{2x}^2 + E_{1x}E_{2x}(\bar{x}_1-\bar{x}_2)^2$$

Thus we get

$$(5) \quad E_x\sigma_x{}^2 = E_{1x}\sigma_{1x}^2 + E_{2x}\sigma_{2x}^2 + \frac{E_{1x}E_{2x}}{E_x}(\bar{x}_1-\bar{x}_2)^2$$

which says that the overall width squared of a sum of two showers is simply the weighted sums of the individual widths plus a term proportional to the square of the separation between them. Note that in this derivation no assumptions have been made concerning the shape of the shower.

Equations (2) and (5) can now be used to eliminate x_2 so that x_1 may be expressed in terms of the average position and individual widths and energies of the constituent showers. The derivation follows: (2) may be rewritten as

$$\bar{x}_2 = \frac{E_x\bar{x} - E_{1x}\bar{x}_1}{E_{2x}}$$

Substituting into (5) gives

$$E_x\sigma_x{}^2 = E_{1x}\sigma_{1x}^2+E_{2x}\sigma_{2x}^2+\frac{E_{1x}E_{2x}}{E_x}\left(\bar{x}_1-\frac{E_x\bar{x}-E_{1x}\bar{x}_1}{E_{2x}}\right)^2$$

$$= \quad '' \quad + \frac{E_{1x}}{E_{2x}E_x}(\bar{x}_1(E_{1x}+E_{2x})-E_x\bar{x})^2$$

$$= \quad '' \quad + \frac{E_{1x}E_x}{E_{2x}}(\bar{x}_1-\bar{x})^2$$

$$(\bar{x}_1-\bar{x})^2 = \frac{E_{2x}}{E_{1x}E_x}(E_x\sigma_x^2 - E_{1x}\sigma_{1x}^2 - E_{2x}\sigma_{2x}^2)$$

Reproduced with permission of the copyright owner. Further reproduction prohibited without permission.

Thus we get

$$(6) \quad \bar{x}_1 = \bar{x} + \left(\frac{E_{2x}}{E_{1x}}\sigma_x^2 - \frac{E_{2x}}{E_x}\sigma_{1x}^2 - \frac{E_{2x}^2}{E_{1x}E_x}\sigma_{2x}^2\right)^{1/2}$$

Similarly for x_2 we get

$$(7) \quad \bar{x}_2 = \bar{x} - \left(\frac{E_{1x}}{E_{2x}}\sigma_x^2 - \frac{E_{1x}}{E_x}\sigma_{2x}^2 - \frac{E_{1x}^2}{E_{2x}E_x}\sigma_{1x}^2\right)^{1/2}$$

One gets a minus sign instead of a plus sign for the square root term because of the minus sign in the $(x_1 - x_2)^2$ term in equation (5). This obviously must be the case since the centers of the two showers must lie on opposite sides of the mean center position.

D.2. Di-photon Mass

Given two photons with 4-momentum vectors $\vec{p}_1 = (E_1, \underline{p}_1)$ and $\vec{p}_2 = (E_2, \underline{p}_2)$, the invariant mass of the pair is

$$\begin{aligned} m_{\gamma\gamma}^2 &= (\vec{p}_1 + \vec{p}_2)^2 \\ &= \vec{p}_1^{\,2} + 2\vec{p}_1\cdot\vec{p}_2 + \vec{p}_2^{\,2} \\ &= 2\vec{p}_1\cdot\vec{p}_2 \qquad \text{since } \vec{p}_1^{\,2} = \vec{p}_2^{\,2} = 0 \text{ for photons} \\ &= 2(E_1E_2 - \underline{p}_1\cdot\underline{p}_2) \end{aligned}$$

Thus we have

$$(8) \quad m_{\gamma\gamma}^2 = 2E_1E_2(1-\cos\theta_{\gamma\gamma})$$

since $\underline{p}_1\cdot\underline{p}_2 = p_1p_2\cos\theta_{\gamma\gamma}$

Reproduced with permission of the copyright owner. Further reproduction prohibited without permission.

and p = E for photons. Now the two photons have position vectors in the forward detector (with respect to the target) of

$$\underline{r}_1 = (x_1, y_1, z) \qquad \text{and} \qquad \underline{r}_2 = (x_2, y_2, z)$$

where z is the distance from the target to the hodoscope.

$$\cos\theta_{\gamma\gamma} = \frac{\underline{r}_1 \cdot \underline{r}_2}{r_1 r_2}$$

$$= \frac{x_1 x_2 + y_1 y_2 + z^2}{(x_1^2+y_1^2+z^2)^{1/2}\,(x_2^2+y_2^2+z^2)^{1/2}}$$

We can approximate this since the lateral dimensions of the detector are small compared to its distance to the target, i.e. x,y << z.

$$\cos\theta_{\gamma\gamma} \simeq \left(1+\frac{x_1x_2+y_1y_2}{z^2}\right)\left(1-\frac{x_1^2+y_1^2}{2z^2}\right)\left(1-\frac{x_2^2+y_2^2}{2z^2}\right)$$

$$\simeq \quad '' \quad \left(1-\frac{x_1^2+y_1^2+x_2^2+y_2^2}{2z^2}\right)$$

$$\simeq \left(1-\frac{1}{2z^2}[x_1^2-2x_1x_2+x_2^2 + y_1^2-2y_1y_2+y_2^2]\right)$$

Therefore to lowest order in $1/z^2$

$$\cos\theta_{\gamma\gamma} \simeq 1 - \frac{1}{2z^2}[(x_1-x_2)^2 + (y_1-y_2)^2]$$

Substituting this into (8) gives

$$(9) \qquad m_{\gamma\gamma}^2 = \frac{E_1E_2}{z^2}[(x_1-x_2)^2 + (y_1-y_2)^2]$$

Now we can use equation (5) derived previously to get

Reproduced with permission of the copyright owner. Further reproduction prohibited without permission.

$$m_{\gamma\gamma}^2 = \frac{E_1E_2}{z^2}[\frac{E^2}{E_1E_2}(\sigma_x^2 - \frac{E_1}{E}\sigma_{1x}^2 - \frac{E_2}{E}\sigma_{2x}^2 + \sigma_y^2 - \frac{E_1}{E}\sigma_{1y}^2 - \frac{E_2}{E}\sigma_{2y}^2)]$$

and arrive at

$$(10) \qquad m_{\gamma\gamma}^2 = \frac{E^2}{z^2}[\sigma_x^2+\sigma_y^2 - \frac{E_1}{E}(\sigma_{1x}^2+\sigma_{1y}^2) - \frac{E_2}{E}(\sigma_{2x}^2+\sigma_{2y}^2)]$$

At this point we have only had to assume that the energies are the same in each plane and in the total absorption counters. If we use the parametrizations for σ_{1x}, σ_{1y}, etc. we have

$$\sigma_{1x}^2 = \sigma_{xo}^2(E_1) = a + bE_1$$

$$\sigma_{1y}^2 = \sigma_{yo}^2(E_1) = c + dE_1 \text{ , etc.}$$

What we want to do is to eliminate E_1 and E_2 (since we don't know them), so we find the average value of the quantities

$$E_1(\sigma_{1x}^2+\sigma_{1y}^2) \qquad \text{and} \qquad E_2(\sigma_{2x}^2+\sigma_{2y}^2)$$

and use those. Since the energy spectrum of photons from a π^o decay is flat (i.e. dN/dE = const.)

$$\langle E_1(\sigma_{1x}^2+\sigma_{1y}^2)\rangle = \frac{1}{E}\int_0^E (a+c)E_1 + (b+d)E_1^2 \, dE_1$$

$$= \frac{1}{E}\left[\frac{E^2}{2}(a+c) + \frac{E^3}{3}(b+d)\right]$$

$$= \frac{E}{2}(a+c) + \frac{E^2}{3}(b+d)$$

Similarly,

$$\langle E_2(\sigma_{2x}^2+\sigma_{2y}^2)\rangle = \frac{E}{2}(a+c) + \frac{E^2}{3}(b+d)$$

Thus (10) becomes on the average

$$m_{\gamma\gamma}^2 = \frac{E^2}{z^2}(\sigma_x^2+\sigma_y^2 - [(a+c) + \frac{2E}{3}(b+d)])$$

Reproduced with permission of the copyright owner. Further reproduction prohibited without permission.

giving the final result:

$$(11) \quad m^2_{\gamma\gamma} = \frac{E^2}{z^2} [\sigma^2_x + \sigma^2_y - \sigma^2_{xo}(\tfrac{2}{3}E) - \sigma^2_{yo}(\tfrac{2}{3}E)]$$

What this says is that on the average, if we use two-thirds of the energy for the width parametrization, we will get the most accurate estimate of the invariant mass of the two photon system. Actually this is complicated a bit by the fact that the parametrizations aren't simple linear expressions, but have a slope which is itself energy dependent. However, this effect is small when compared to the other errors in the calculation such as the error coming from the energy resolution of the total absorption counters, so we ignore the effect and just use two-thirds of the total shower energy for the parametrization of the widths.

Reproduced with permission of the copyright owner. Further reproduction prohibited without permission.

References

[Angelis 78]
A. L. S. Angelis, B. J. Blumenfeld, L. Camilleri, T. J. Chapin, R. L. Cool, C. del Papa, L. DiLella, Z. Dimchovski, R. J. Hollebeek, L. M. Lederman, D. Levinthal, J. T. Linnemann, L. Lyons, N. Phinney, B. G. Pope, S. H. Pordes, A. F. Rothenberg, A. M. Segar, S. Singh-Sidhu, A. M. Smith, M. J. Tannenbaum, R. A. Vidal, J. Wallace-Hadrill, T. O. White, and J. M. Yelton. A Measurement of Inclusive π^0 Production at Large p_t from p-p Collisions at the CERN ISR. Physics Letters, 79B, 505 (1978).

[Bauer 78]
T. H. Bauer, R. D. Spital, D. R. Yennie, and F. M. Pipkin. The Hadronic Properties of the Photon in High-energy Interactions. Reviews of Modern Physics, 50, 261 (1978).

[Berger 73]
C. Berger, G. Dick, W. Erlewein, K. Lubelsmeyer, L. Paul, H. Meyer-Wachsmuth, and A. Schultz von Dratzig. Inclusive Photoproduction of π^0 Mesons at 6 GeV. Physics Letters, 47B, 377 (1973).

[Berger 77]
C. Berger, R. Buhring, G. Dick, R. Grigull, W. Wagner, H. Ackermann, T. Azemoon, W. Gabriel, H. D. Mertiens, H. D. Reich, F. Janata, and D. Schmidt. Electroproduction of Neutral Pions and Test of the Quark-Parton Model. Physics Letters, 70B, 471 (1977).

[Bjorken 69]
J. D. Bjorken and E. A. Paschos. Inelastic Electron-Proton and Photon-Proton Scattering and the Structure of the Nucleon. Physical Review, 185, 1975 (1969).

[Blankenbecler 74]
R. Blankenbecler and S. J. Brodsky. Unified Description of Inclusive and Exclusive Reactions at all Momentum Transfers. Physical Review, D10, 2973 (1974).

[Blankenbecler 78]
R. Blankenbecler, S. J. Brodsky, and J. F. Gunion. Magnitude of Large-Transverse-Momentum Cross Sections. Physical Review, D18, 900 (1978).

Reproduced with permission of the copyright owner. Further reproduction prohibited without permission.

[Boyarski 76]
A. M. Boyarski, D. H. Coward, S. D. Ecklund, B. Richter, D. J. Sherden, R. H. Siemann, C. K. Sinclair. Inclusive Photoproduction of Charged Particles in the Forward Hemisphere. Physical Review, D14, 1733 (1976).

[Breakstone 74a]
A. Breakstone, D. Cheng, D. Dorfan, A. Grillo, and C. Heusch. Detection Apparatus for NAL-Experiment 152. UCSC Internal Note 74/036 (8/74).

[Breakstone 74b]
A. Breakstone, D. Cheng, D. Dorfan, A. Grillo, and B. Smith. SLAC Tests of NAL Prototype Shower Detectors. UCSC Internal Note 74/037 (9/74).

[Breakstone 74c]
A. Breakstone. Phototube Tests. UCSC Internal Note (11/1/74).

[Breakstone 75a]
A. Breakstone. On-line Results for Total Absorption Counters. UCSC Internal Note (5/8/75).

[Breakstone 75b]
A. Breakstone. A Note on Comparisons of Pilot 425, UVT Plexiglas, and Scintillator. UCSC Internal Note (5/13/75).

[Breakstone 75c]
A. Breakstone. Design of Shower Counters for FNAL Experiment #152. UCSC Internal Note 75/043 (11/75).

[Breakstone 75d]
A. Breakstone. Proposed Monitoring of the Total Absorption Counters. UCSC Internal Note 75/045 (12/75).

[Breakstone 76a]
A. Breakstone. Forward LED System Test. UCSC Internal Note (2/76).

[Breakstone 76b]
A. Breakstone. LED Long-term Stability Test. UCSC Internal Note (2/76).

[Breakstone 76c]
A. Breakstone. LED Temperature Dependence Test. UCSC Internal Note (3/8/76).

[Breakstone 76d]
A. Breakstone. Time-of-Flight LED System. UCSC Internal Note (4/19/76).

Reproduced with permission of the copyright owner. Further reproduction prohibited without permission.

[Breakstone 76e]
A. Breakstone, A. Grillo, and D. Smith. Fermilab Test of Shower Counters. UCSC Internal Note (12/31/76).

[Breakstone 77a]
A. Breakstone. Forward Detector Monte Carlo Studies. UCSC Internal Note (4/11/77).

A. Breakstone. Addendum to Forward Detector Monte Carlo Studies. UCSC Internal Note (4/18/77).

A. Breakstone. Position Ambiguity Monte Carlo Studies. UCSC Internal Note (4/29/77).

[Breakstone 77b]
A. Breakstone. Summary of Results from Test Run of August, 1977. UCSC Internal Note (8/23/77).

A. Breakstone. Tape Contents from Test Run, August, 1977. UCSC Internal Note (8/26/77).

[Breakstone 77c]
A. Breakstone. How to Read the FNALTEST Tapes. UCSC Internal Note (8/31/77).

A. Breakstone. How to Use FNALTEST (Rev 2). UCSC Internal Note (11/9/77).

[Breakstone 78a]
A. Breakstone. Calibration Tape Contents, October, 1977. UCSC Internal Note (1/12/78).

A. Breakstone. Calibration Run Conditions, October, 1977. UCSC Internal Note (1/12/78).

A. Breakstone. Results of the Calibration Runs of October, 1977. UCSC Internal Note (3/20/78).

[Breakstone 78b]
A. Breakstone, D. Dorfan, A. Grillo, C. Heusch, V. Palladino, T. Schalk, A. Seiden, and D. Smith. E152 Status Quo. UCSC Internal Note (3/6/78).

[Breakstone 78c]
A. Breakstone. FNALTEST Rev 3. UCSC Internal Note (4/11/78).

A. Breakstone. Addendum to FNALTEST Rev 3. UCSC Internal Note (5/9/78).

[Breakstone 78d]
A. Breakstone. Calibration Tape Contents, May, 1978. UCSC Internal Note (6/2/78).

Reproduced with permission of the copyright owner. Further reproduction prohibited without permission.

A. Breakstone. Calibration Run Conditions, May, 1978. UCSC Internal Note (6/3/78).

[Breakstone 78e]
A. Breakstone. E152 Magnetic Tape Formats. UCSC Internal Note (5/25/78).

A. Breakstone. Tape Copying Procedures. UCSC Internal Note (6/1/78).

[Breakstone 78f]
A. Breakstone. Data Tape Contents Summary. UCSC Internal Note (12/29/78).

[Breakstone 80]
A. Breakstone. Preliminary PhD Thesis (Long Version). UCSC Internal Note (4/80).

[Brenner 77]
A. Brenner and R. Martin. CAMAC DVM Control for the HP3485. Fermilab Technical Note DVM CONTROL BISON HN-10.1 (1977).

[Caldwell 78]
D. O. Caldwell, J. P. Cumalat, A. M. Eisner, A. Lu, R. J. Morrison, F. V. Murphy, S. J. Yellin, P. J. Davis, R. M. Egloff, M. E. B. Franklin, G. J. Luste, J. F. Martin, J. D. Prentice, and T. Nash. Measurements of the Photon Total Cross Section on Protons from 18 to 185 GeV. Physical Review Letters, 40, 1222 (1978).

[Clark 78]
A. G. Clark, P. Darriulat, K. Eggert, V. Hungerbuhler, P. M. Patel, J. Strauss, A. Zalle, M. Banner, C. Lapuyade, T. Modis, P. Perez, J. Teiger, C. Tur, J. P. Vialle, H. Zaccone, A. Zylbersteijn, P. Jenni, P. Strolin, G. S. Tarnopolsky. Large Transverse Momentum Production in Proton-Proton, Deuterium-Proton, and Deuterium-Deuterium Collisions at the CERN ISR. Nuclear Physics, B142, 189 (1978).

[Cumalat 77]
J. P. Cumalat. Measurements of the Photon Total Cross Section on Protons from 45 GeV to 182 GeV. PhD Thesis, University of California, Santa Barbara (9/77).

[Davis 74]
P. Davis, R. Morrison, T. Nash, J. Prentice, J. Cumalat, R. Egloff, G. Luste, and F. Murphy. The Electron Beam Test of October-November, 1974. NAL Technical Memo TM-535 (1974).

Reproduced with permission of the copyright owner. Further reproduction prohibited without permission.

[Egloff 79]
R. M. Egloff. Measurements of Elastic Rho, Omega and Phi Meson Photoproduction Cross Sections on Protons from 30 to 180 GeV. PhD Thesis, University of Toronto (1979).

[Eisner 74]
A. M. Eisner, D. O. Caldwell, J. P. Cumalat, B. N. Kendall, T. P. McPharlin, R. J. Morrison, and F. V. Murphy. Inclusive π^0 and η Photoproduction at High Transverse Momenta. Physical Review Letters, 33, 865 (1974).

[Field 78a]
R. D. Field and R. P. Feynman. A Parametrization of the Properties of Quark Jets. Nuclear Physics, B136, 1 (1978).

[Field 78b]
R. D. Field. Can Existing High-Transverse-Momentum Hadron Experiments Be Interpreted by Contemporary Quantum Chromodynamics Ideas? Physical Review Letters, 40, 997 (1978).

[Field 79]
R. D. Field. Perturbative Quantum Chromodynamics and Applications to Large Momentum Transfer Processes. California Institute of Technology Report CALT-68-739 (10/10/79).

[Garbincius 76]
P. Garbincius. A Short Guide for Tuning the TPL Electron Beam. Fermilab Note (9/25/76).

[Garbincius 78]
P. Garbincius. An Increased Acceptance Electron Beam for the Tagged Photon Lab. Fermilab Note (3/16/78).

[Grillo 76]
A. Grillo. Study of Multiple Peaks in Showers Observed by the Multi-wire Proportional Chamber. UCSC Internal Note (6/76).

[Grillo 79]
A. Grillo. The Design of CAMAC Diagnostic Module. Nuclear Instruments and Methods, 165, 379 (1979).

[Grillo 80]
A. Grillo. Elastic Photon-Proton Scattering in the 100 GeV Energy Region. PhD Thesis, University of California, Santa Cruz (1980).

Reproduced with permission of the copyright owner. Further reproduction prohibited without permission.

[Gunion 72]
J. F. Gunion, S. J. Brodsky, and R. Blankenbecler. Composite Theory of Scattering at Large Transverse Momenta. Physical Review, D6, 2652 (1972).

[Halliwell 72]
C. Halliwell, P. J. Biggs, W. Busza, M. Chen, T. Nash, F. Murphy, G. Luxton, and J. D. Prentice. Design of a Tagged Photon-Electron Beam Facility for NAL. Nuclear Instruments and Methods, 102, 51 (1972).

[Jacob 78]
M. Jacob and P. V. Landshoff. Large Transverse Momentum and Jet Studies. Physics Reports, 48, 285 (1978).

[Jones 79]
D. Jones and J. F. Gunion. Transition from Constituent-Interchange to Quantum-Chromodynamic p_t Dominance at High Transverse Momentum. Physical Review, D19, 867 (1979).

[Kourkoumelis 79]
C. Kourkoumelis, L. K. Resvanis, T. A. Filippas, E. Fokitis, A. M. Cnops, S. Iwata, R. E. Palmer, D. C. Rahm, P. Rehak, I. Stumer, C. W. Fabjan, T. Fields, D. Lissauer, I. Manneli, P. Mouzourakis, A. Nappi, W. J. Willis, and M. Goldberg. Inclusive η Production at High p_t at the ISR. Physics Letters, 84B, 277 (1979).

[Loomis 79]
W. A. Loomis, B. A. Gordon, F. M. Pipkin, S. H. Pordes, W. D. Shambroom, L. J. Verhey, R. Wilson, H. L. Anderson, R. M. Fine, R. H. Heisterberg, H. S. Matis, L. Mo, L. C. Myrianthopoulos, S. C. Wright, W. R. Francis, R. G. Hicks, T. B. W. Kirk, V. K. Bharadwaj, N. E. Booth, G. I. Kirkbride, T. W. Quirk, A. Skuja, M. A. Staton, W. S. C. Williams. Hadron Production in Muon-proton and Muon-deuteron Collisions. Physical Review, D19, 2543 (1979).

[Messel 70]
H. Messel and D. F. Crawford. Electron-Photon Shower Distribution Function. Pergamon Press (1970).

[Palladino 80]
V. Palladino. Exclusive Photoproduction of Omega Mesons at Fermilab Energies. PhD Thesis, University of California, Santa Cruz (1980).

[Seiden 76]
A. Seiden. A Simple Model for the Quark Fragmentation Functions Seen in Deep Inelastic Processes. Physics Letters, B68, 157 (1976).

Reproduced with permission of the copyright owner. Further reproduction prohibited without permission.

[Seiden 77]
A. Seiden. Hadron Distributions in a Quark-Parton Model. SLAC-PUB-1962 (also UCSC 77-061) (6/77).

[Seiden 78]
A. Seiden, T. L. Schalk, and J. F. Martin. Particle Production in a Quark-Cascade Model. Physical Review, D18, 3990 (1978).

Reproduced with permission of the copyright owner. Further reproduction prohibited without permission.